Catalytic Transformation of Biomass-Derived Oxygenates Using Transition Metal Carbide, Nitride, and Oxide Surfaces

Zhexi Lin

Submitted in partial fulfillment of the
requirements for the degree of
Doctor of Philosophy
under the Executive Committee
of the Graduate School of Arts and Sciences

COLUMBIA UNIVERSITY

2021

Abstract

Catalytic Transformation of Biomass-Derived Oxygenates Using Transition Metal Carbide, Nitride, and Oxide Surfaces

Zhexi Lin

The catalytic conversion of biomass-derived oxygenates into valuable fuels and chemicals is a promising route to address the current energy and environmental issues. The low-temperature catalytic conversion is particularly promising in that it does not require intense energy input and can yield a variety of value-added products. In this approach, the hydrodeoxygenation reaction removes excess oxygen in biomass-derived oxygenates to convert them into value-added fuels and chemicals. There are two promising conversion pathways under this category: the conversion of lignocellulosic biomass and the biodiesel production from waste cooking oils. In the first approach, furfural is an important platform chemical that can be further upgraded into value-added products. Transition metal carbide catalysts have been demonstrated to be highly active and selective in cleaving the aliphatic C-O bond to form 2-methylfuran from furfural. However, the stability of these catalysts needs further improvement. In the second approach of biodiesel production, glycerol is a major by-product. The upgrading of glycerol via the selective hydrodeoxygenation reaction is especially economically promising. Different numbers of C-O bonds of glycerol can be cleaved to form value-added compounds, such as allyl alcohol, propanal, and acetol. Mo_2C has previously been shown as a selective catalyst for C-O bond scission, but its interaction with oxygen is so strong that all the C-O bonds in glycerol are cleaved. In order to selectively break certain numbers of C-O bonds while preserving others, the Mo_2C catalyst needs to be modified.

In this dissertation, the strategies for modifying the Mo_2C surface to achieve enhanced stability for furfural conversion and tunable selectivity for glycerol upgrading are demonstrated. With the addition of cobalt, the interaction between the surface and the oxygen atom in furfural is lowered to a proper extent and therefore the stability of Mo_2C is enhanced. By using different coverages of copper to modify Mo_2C, the number of C-O bonds cleaved in glycerol can be controlled. The subsequent chapters then compare the reactions of glycerol over the corresponding transition metal nitride, Mo_2N, as well as the C-O bond scission over a modified transition metal oxide, WO_x/Pt(111), surface. It is shown that while Mo_2C and Mo_2N both break all C-O bonds of glycerol to produce propylene, Mo_2N also selectively cleaves two C-O bonds of glycerol to form allyl alcohol and propanal, a phenomenon only observed on the Cu/Mo_2C interface. DFT calculations reveal that the surface nitrogen atoms in Mo_2N block some Mo sites, and therefore promote the selective C-O bond scission. In the case of C-O bond scission of isopropanol over WO_x/Pt(111), it is shown that surface hydroxyl groups on WO_x sites catalyze the reaction. DFT results also demonstrate the synergistic effect between WO_x and Pt and predict the energetics of *in situ* acid sites formation, which are very useful for the optimization of relevant metal oxide/metal catalysts. Overall, this dissertation compares the similarities and differences regarding the active sites and reaction mechanisms of C-O/C=O bond scission of biomass-derived oxygenates over transition metal carbide, nitride, and oxide surfaces, which should in turn provide useful guidelines for the rational catalyst design for biomass upgrading reactions.

Table of Contents

List of Figures

List of Tables

List of Schemes

Acknowledgements

I am truly grateful for everyone who helped me during my doctoral study at Columbia. First and foremost, I would like to thank Prof. Jingguang G. Chen for all his guidance and support throughout my PhD study. He has inspired me not only in research, but also in teaching, and beyond. He showed me examples of how to think correctly and carefully. I could not have been where I am without his guidance and inspiration. I would also like to thank my thesis committee members, Prof. Alan C. West, Prof. Daniel V. Esposito, Prof. Ah-Hyung Alissa Park, Prof. Robert J. Farrauto for the help and guidance on my thesis.

I also want to thank my collaborators at the University of Delaware, Dr. Shizhong Liu for performing the DFT calculations and drafting the manuscript used in Chapter 6, and Dr. Stavros Caratzoulas and Prof. Dionisios G. Vlachos for their advice and paper writing. In addition, I would like to thank Jiayu Fu, Dr. Weiqing Zheng, and Dr. Sibao Liu for the valuable discussion. I am also grateful to my collaborators at the University of South Carolina, Dr. Salai C. Ammal for the DFT calculations and manuscript presented in Chapter 5, Kyung-Eun You for the helpful discussion, and Prof. Andreas Heyden for his guidance and writing of the paper. I am especially thankful to Prof. Sergey A. Rykov who helped repair all the electronics and instruments in the lab, as well as Dr. Zhenhua Xie for the valuable discussion on different research projects. In addition, I would like to acknowledge help with our instruments from our vendors, especially Randy Dellwo from RBD Instruments, Larry Kesmodel from LK Technologies, and Richard Opsal from Adron Systems.

I am also very grateful to all the Chen Group members at Columbia who have helped me throughout the years. As my research mentor, Dr. Weiming Wan helped me get started and taught me all the details about my projects. Prof. Ke Xiong has provided me guidance and inspired me

with his research. Dr. Brian Tackett and Dr. Lea Winter also helped me with various aspects about my research and thesis. Dr. Nongnuch Arthrith taught me DFT calculations. Steven Denny and Will Porter have been my lab mates over the past two years, when we learned from each other and kept the research projects going smoothly. I am also very grateful to all the visiting scholars to our lab, including but not limited to Dr. Hui Wang, Dr. Xiaoran Niu, Dr. Qun He, Dr. Kuan Chang, Dr. Xiaodan Li, Dr. Xin Chen, and Dr. Zhifeng Jiang. I have learned different skills and knowledge from them and enjoyed the friendship with them as well. Furthermore, I would also like to acknowledge the Chen Group members and friends at Brookhaven National Laboratory who have assisted me in different aspects, especially Prof. Binhang Yan, Prof. Siyu Yao, Dr. Baohuai Zhao, for their fruitful discussion, help with setting up the flow reactor, and the synthesis and characterization of the catalysts used in Chapter 3. I also want to acknowledge Dr. Yumeng Liu, Dr. Dong Tian, Prof. Zhao Jiang, Prof. Wenchao Sheng, and Dr. Qiyuan Wu for their assistance and valuable discussion.

Additionally, I would like to thank my friends and classmates at Columbia for their help and friendship, especially Jianzhou Qu and Dr. Christiana Lininger for their help with DFT calculations, Dr. Nicholas Brady, Dr. Emily Hsu, Dr. William Tsui, Dr. Yong Dou, Dr. Wenjie Fei, Zeyu Hui, and Xueqi Pang for their friendship and help with research and coursework. I would also like to thank Kathy Marte-Garcia, Emely Aquino, Ariel Sanchez, Aurna Malakar, Rezarta Binaj for their essential support to my doctoral research and study at Columbia. I also acknowledge the Environmental Health and Safety (EH&S) and Facilities Department that ensure we have a safety and productive environment for research. I am also grateful to the staff at Airgas who supply essentials gasses to our lab, especially Jane Ferguson and Noah for order processing and gas delivery.

I am also very grateful to my friends and family who have supported me over the years. I would like to thank my parents and brother for all their generous support. I also thank my friend and mentor, Richard A. Roth CC '72. Last but not least, I owe everything to Alma Mater, our nurturing mother, Columbia University in the City of New York.

Chapter 1: Introduction

1.1 Catalytic Biomass Transformation and C-O/C=O Bond Scission

The catalytic upgrading of non-edible lignocellulosic biomass to fuels and chemicals is a promising way to mitigate current environmental issues and to address energy challenges. Various methods and processes have been developed to convert lignocellulosic biomass into cellulose, hemicellulose and then to C5 and C6 sugars, xylose, fructose and glucose.[1-2] These C5 and C6 sugars can then be converted into platform biomass-derived chemicals, including furfural and 5-hydroxylmethylfufural, which can be further upgraded to fuel additives such as 2-methylfuran (2-MF) or industrial-relevant chemicals such as p-xylene.[3]

The main motivation for converting lignocellulosic biomass is that the biomass-derived molecules contain excess oxygen. The high O/C ratio limits the energy density of the biomass derivatives, as well as the selectivity to desired products during the upgrading processes.[4] In order to solve this problem, the excess oxygen needs to be removed via deoxygenation, which can be divided into two types of reactions: deocarbonylation/decarboxylation (DCO) and hydrodeoxygenation (HDO). The DCO reactions cleave the C-C bond associated with the carbonyl group or carboxyl group, resulting in loss of carbon and decreasing the energy content of the molecule. On the other hand, the HDO reaction selectively cleaves the C-O/C=O bond while preserving the carbon chain length. Moreover, under sufficient H_2 partial pressure, the HDO reaction removes oxygen in the form of H_2O instead of CO_2 and is therefore more environmentally friendly than DCO regarding CO_2 emission.

1.2 Unique Catalytic Properties of Transition Metal Carbide, Nitride, and Oxide Surfaces

The selective C-O bond scission of biomass derivatives has been studied using various types of catalysts, including bimetallics[3,10–14], and transition metal carbide-based and oxide-based catalysts[15–22]. Transition metal carbides and nitrides (TMCs and TMNs) have drawn much attention due to their unique catalytic properties. Professor Boudart was among the pioneers in the investigation of TMCs and TMNs. In 1973, Levy and Boudart found that tungsten carbides possessed Pt-like properties during the reactions of H_2 oxidation to produce H_2O and 2,2-dimethylpropane isomerization to form 2-methylbutane.[5] Subsequently, there have been many reviews of the electronic, structural, and catalytic properties of TMCs and TMNs.[6–9] TMCs and TMNs, in the form of either thin films or powder catalysts, are synthesized by the incorporation of carbon and nitrogen into the crystal lattices of the respective parent metals. TMCs and TMNs demonstrate unique physical and chemical properties, such as extreme hardness and brittleness similar to that of covalent solids, high melting temperatures and simple crystal structures that are representative of ionic crystals, as well as electronic and magnetic properties resembling those of transition metals.[8] TMCs and TMNs are also refractory and resistant to sintering at high temperatures. Typical crystal structures of TMCs and TMNs include face-centered cubic (fcc), hexagonal close-pack (hcp) or simple hexagonal (hex) structures.[8] Due to the incorporation of carbon and nitrogen into the metal lattice, the electronic and structural properties of TMCs and TMNs are altered from their parental metals, as reported in many experimental and theoretical studies. For example, Kitchin *et al.* studied the change of electronic properties of TMCs using DFT calculations and found that the d-band structures of TMCs were significantly different from the parent metals, and the incorporation of carbon species also induced strain in the surface structure

of the parent metals. These changes of electronic and surface structures translated to different binding energies observed on TMCs.[10] Frühberger *et al.* also demonstrated experimentally that, by carburizing a single crystal Mo(110) surface, the reactivity of the surface was substantially changed to resemble those of Pt-group metals.[11] Therefore, it is possible to design TMC and TMN catalysts using earth-abundant metals, either as catalysts or as catalyst supports, to replace or reduce the loading of precious metals. More recently, however, TMCs and TMNs have been found to demonstrate significantly different catalytic properties than Pt-group metals in reactions involving oxygen-containing molecules.[12] TMCs and TMNs have been shown to be very selective in breaking the C-O/C=O bonds in the hydrodeoxygenation (HDO) reaction[13] primarily due to the strong interaction between TMCs/TMNs with the oxygen atom.

Transition metal oxides (TMOs) are another type of promising catalysts for the C-O/C=O bond scission of biomass-derived oxygenates.[14,15] Their structures are substantially different from those of TMCs and TMNs. The active sites on oxide surfaces also differ from those on carbides and nitrides. The active sites on TMCs and TMNs are still metal-like, modified electronically or structurally by carbon or nitrogen atoms. The actives sites present on TMOs could be the hydroxyl groups when surface oxygen atoms are protonated, or oxygen vacancies resulted from partial oxidation or removal of surface oxygen atoms. Consequently, the reaction mechanisms on oxides are significantly different from those of carbides and nitrides. For example, both Pt/WO_x and its inverse oxide, WO_x/Pt, are particularly interesting because they have multiple distinct active sites and are active and selective for the C-O bond scission of glycerol, tetrahydrofurfuryl alcohol, and m-cresol.[23–29] For the glycerol hydrogenolysis reaction that produces 1,3-propanediol, it has been proposed that the Pt site is responsible for dissociating hydrogen, which then spills over to the WO_x site to form *in situ* Brønsted acid sites that catalyze the selective C-O bond scission.[26,27] On

the other hand, it has also been proposed that WO_x covers the Pt particles due to the strong metal-support interaction (SMSI) during the ring opening reaction of tetrahydrofurfuryl alcohol to produce 1,5-pentanediol.[28] The oxygen vacancy sites on WO_x serve as the active sites for the HDO reaction of m-cresol.[29]

Since TMCs have emerged as promising HDO catalysts and have been extensively studied, the remainder of this chapter will mainly discuss the C-O/C=O bond scission of biomass-derived oxygenates over TMCs. Molybdenum carbide (Mo_2C) and tungsten carbide (WC) have been shown to be highly selective toward C-O/C=O bond scissions. For example, Yu *et al.* have shown that Mo_2C selectively cleaves the C-O bonds in ethylene glycol to produce ethylene, with the C-C bond remaining intact.[16] Ren *et al.* have demonstrated that WC and Mo_2C selectively cleave the C-O/C=O bond of C3 oxygenates, such as propanol and propanal, to produce propylene.[17,18] Ruddy *et al.* investigated the mechanism of the acetic acid HDO reaction and identified different types of active sites with different functionality.[19] Bhan *et al.* used the acetone HDO reaction to demonstrate the bifunctionality of Mo_2C and the effect of oxygen modification on the active sites.[20] Additionally, there are a number of studies on the HDO of longer chain molecules, such as methyl stearate,[21-22] oleic acid,[23,24] stearic acid[21,25,26] and vegetable oils.[22,27-28] Model compounds for lignin derivatives, such as anisole[29-30] and guaiacol,[31-32] have also been extensively studied. Xiong *et al.* have reported that Mo_2C is selective to the HDO of furfural to 2-methylfuran.[33] Several HDO reactions with Mo_2C have been investigated using both experimental and computational approaches and detailed reaction mechanisms have been proposed.[17,18,34]

In additional to their high HDO selectivity, TMCs can be used as substrates to support metal catalysts for HDO reactions. Wan *et al.* have shown that the bimetallic Fe/Pt(111) surface is active toward the HDO reaction of furfural.[35] However, at elevated temperatures, Fe tends to

diffuse into the Pt bulk, causing the HDO activity of Fe/Pt(111) to decrease. In contrast, by changing the substrate from Pt(111) to Mo_2C, the stability of Fe/Mo_2C/Mo(110) is enhanced while maintaining similar HDO activity as that of Fe/Pt(111).[36] This is because the Mo_2C substrate possesses Pt-like properties and can also serve as a barrier to prevent the Fe from diffusing into the bulk, therefore retaining the HDO activity with enhanced stability.[37-38] Similarly enhanced stability is also observed on Co/Mo_2C/Mo(110) for the furfural HDO reaction, compared to Co/Pt(111).[39,35]

Research progress on the conversion of lignocellulosic biomass over TMC catalysts has been summarized by several reviews. Xiong *et al.* summarized and compared different bimetallic and TMC catalysts that can be used to achieve desired bond-cleavage sequence for reforming and HDO reactions of biomass-derived molecules.[4] Bhan *et al.* summarized the synthesis of TMCs and *in situ* chemical titration techniques to identify different sites on the bifunctional TMC catalysts.[40] Medlin *et al.* reviewed the bifunctional catalysts for the HDO reaction of pyrolysis oil and model compounds from biomass derivatives, with a focus on the influence of catalyst structures on reactivity.[41] This chapter aims to summarize the recent findings of HDO reactions of biomass-derived molecules with different structures (linear-chain vs. ring-containing) over TMC model surfaces. DFT calculations, surface science studies on single crystals. General trends in the HDO of linear-chain and ring-containing biomass-derived molecules over TMC surfaces are drawn.

1.3 HDO of Linear-Chain Oxygenates

Linear-chain oxygenates represent an important class of biomass-derived molecules. Simple linear-chain molecules are often used as model compounds for the study of more complex biomass derivatives. Their relatively simple molecular structures significantly reduce the computational expense, and their relatively high vapor pressures allow the dosing into ultrahigh vacuum (UHV)

chamber for single crystal studies. C2 linear molecule such as ethylene glycol, glycolaldehyde and acetic acid are good model compounds because they have the same C/O ratio as C5 and C6 sugars and contain various functional groups. For the study of unsaturated fatty acids with relatively long chains, acrylic acid can serve as a model compound because it has a shorter chain that contains one C=C bond and one carboxylic acid functional group. In order to highlight the HDO reactions of linear oxygenates over TMC catalysts, this section uses the reactions of C2 (acetaldehyde, glycolaldehyde and acetic acid) and C3 oxygenates (propanal, propanol, 2-propanol and acrylic acid) on TMC surfaces as examples to demonstrate the selective C-O/C=O bond cleavage capability of TMCs.

1.3.1 C=O/C-O Bond Scission of C2 Oxygenates

As a major product of the *ex-situ* catalytic fast pyrolysis (CFP) of biomass, acetic acid can be converted via various pathways, including DCO, HDO and ketonization (KET).[19] Acetic acid contains a C-O bond and a C=O bond. Therefore, it can be used to probe whether the carbide surface can promote the cleavage of one bond or both carbon-oxygen bonds. Using a combination of DFT and UHV techniques, Yu *et al.* demonstrated that acetic acid undergoes complete C-O/C=O bond scission to produce ethylene on the WC surface.[42] In comparison, when modified by Ni, the Ni/WC surface tends to break the C-C and C-H bonds to yield the reforming products (CO + H_2).

TPD results reveal that ethylene is only produced on the WC surface, while H_2, CO and CO_2 are produced on the 0.5ML and 1ML Ni-modified WC surfaces. HREELS measurements demonstrate that acetic acid undergoes O-H scission to generate an acetate, CH_3COO, intermediate that binds to the WC and 1 ML Ni/WC surfaces. The disappearance of the ν(C=O) mode (1711 cm^{-1}) at 200K indicates that the -COO group binds to the surfaces in a bidentate bonding

configuration. The main difference between the WC and 1ML Ni/WC surfaces is that the C-C bond of acetate, indicative of the ν(CC) mode at 1028 cm^{-1}, is preserved on WC up to 600 K but cleaved on 1ML Ni/WC at above 500 K. This is consistent with the ethylene peak temperature of 640 K on WC, as well as the production of H_2, CO and CO_2 between 500 K and 600 K on 1 ML Ni/WC from the TPD results.

In order to compare the different interactions of the –COOH and –C=O functional groups on WC, TPD and HREELS measurements of acetaldehyde have also been performed on WC and Ni/WC surfaces.[42] the TPD results reveal that the primary product over WC is ethylene, which is formed by cleaving the C=O bond of acetaldehyde between 300 K and 500 K. On Ni/WC, the main products are H_2, CO and CH_4, indicating that acetaldehyde undergoes C-C and C-H scissions. HREELS experiments show that the ν(C=O) mode at 1650 cm^{-1} of acetaldehyde is weakened upon increasing the temperature to 200 K and disappears at 300 K, indicating that acetaldehyde changes to a di-σ bonding configuration at 300 K. On Ni/WC, the attenuation of the δ(CCO) mode at 528 cm^{-1} and the ν(CC) mode at 1109 cm^{-1} at 300 K suggests the start of C-C scission, which is consistent with the TPD results.

Vohs *et al.* performed surface studies on the reaction of glycolaldehyde over a Mo_2C surface using TPD and HREELS.[43] It is demonstrated that below 550 K, the primary product is ethylene, with ethanol and acetaldehyde as minor products. These three products are all produced from the deoxygenation reactions, indicating that Mo_2C is highly selective toward the C-O/C=O scission. HREELS results reveal that at temperatures below 200 K, glycolaldehyde bonds to Mo_2C via an η_1(O) bonding configuration, which then transit to a di-σ η_2(C=O) bonding configuration between 200 K and 300 K. The di-σ η_2(C=O) configuration weakens the C=O bond, facilitating the subsequent C=O scission.[43]

1.3.2 C=O/C-O Bond Scission of C3 Oxygenates

TMCs have been studied extensively for the HDO of biomass-derived oxygenate molecules. The production of fuels and chemicals from renewable biomass is an effective method to reduce the dependence on fossil fuels and to alleviate environmental pollution.[44] The high oxygen content in biomass derivatives often leads to undesirable side reactions or reduce the heat value of the derivatives.[4] Therefore, efforts have been made to identify catalysts that selectively cleave the C-O/C=O bond while preserving the C-C bond in biomass-derived molecules. TMCs have shown promise in the selective bond scission in biomass-derived molecules. Due to the complexity of biomass derivatives, model compounds have been used for the study of C-O/C=O bond scission. TMC single crystals and powders have been studied extensively for the HDO reaction of C3 oxygenates containing one hydroxyl group. For example, temperature programmed desorption (TPD) experiments revealed the formation of the HDO product, propylene, from the reactions of both propanal and 1-propanol over Mo_2C/Mo(110), with desorption peaks at 390 K and 403 K, respectively.[18,45] The similar propylene desorption peak shapes and temperatures suggested that both propanal and 1-propanol went through similar intermediates (propoxide or η_2(C,O)-propanal), as confirmed by the high-resolution electron energy loss spectroscopy (HREELS) measurements. It is worth noting that the selective C-O/C=O bond scission over Mo_2C/Mo(110) was not observed over transition metal surfaces,[46–48] therefore highlighting the unique HDO selectivity of TMC surfaces.

Ren *et al.* extended the promising results from single crystal surfaces to Mo_2C powder catalysts for the HDO reaction of a variety of C3 oxygenates (propanal, propanol, 2-propanol, and acetone).[18] It was found that propylene was the major product for all reactants, with propane being a minor product. The yields of C2 products were less than 2%, suggesting that Mo_2C was highly

selective in breaking the C-O/C=O bonds while preserving the C-C bond. They also studied the effect of H_2 on the stability of Mo_2C, and found that by co-feeding H_2 the steady-state conversion was around 50% at 573 K, whereas the catalyst deactivated rapidly without co-fed H_2. It was also shown that with co-fed H_2, H_2O was produced from the removal of surface oxygen by H_2. The authors also showed that even with excess H_2, the HDO product from propanal was mainly propylene instead of propane, which was the main HDO product over precious metal catalysts.[49,50]

DFT calculations were performed to explain the high selectivity of Mo_2C toward the C-O/C=O bond scission.[18] Upon adsorption, propanal underwent C-O bond scission with an activation barrier of 0.61 eV. In contrast, the activation energy for C-C bond scission was 1.21 eV, consistent with the experimental observation of low activity toward C-C bond scission. The authors also used DFT calculations to investigate the effect of hydrogen on surface oxygen removal. The dissociative adsorption of H_2 onto the O-bound Mo_2C surface site was favorable, with a barrier of 0.46 eV. The resulting OH* underwent reaction with another OH* to produce water and O* with a barrier of 1.18 eV, thereby removing surface oxygen to enhance the stability of Mo_2C, which was consistent with the experimental results. In another study, Ren *et al.* also used DFT calculations to investigate the reaction pathways and energetics of propanal and propanol deoxygenation over WC(0001). Propanol chemisorbed on WC(0001), releasing 1.05 eV energy, and underwent O-H bond scission to form the propoxy ($CH_3CH_2CH_2O$) intermediate with an Ea of 0.66 eV. The C-H bond scission of chemisorbed propanol was unfavorable, as the barrier was 1.50 eV. The propoxy intermediate preferably went through further dehydrogenation to form the CH_3CH_2CHO intermediate, which was the same intermediate produced from propanal adsorption. Such an intermediate readily underwent C-O/C=O bond scission selectively to form propylene, with an activation energy of 0.33 eV and a reaction energy of -2.42 eV, indicating that the reaction

was both kinetically and thermodynamically favorable. Overall, DFT calculations predicted that both Mo_2C(0001) and WC(0001) were highly selective toward C-O/C=O bond scission. Ren *et al.* compared the HDO of propanal over Mo_2C and WC powder catalysts. It was found that Mo_2C showed a significantly higher propanal steady-state conversion (~40%) than WC (<20%). They attributed this to the smaller particle size of Mo_2C (3~5 nm), as compared to the large WC particles (~100nm) resulting from the higher synthesis temperature (1273 K) necessary to achieve the WC phase. Nonetheless, both Mo_2C and WC showed high selectivity to propylene (~60%), consistent with the DFT predictions that both catalysts should be highly selective towards C-O/C=O bond scission.

In addition to HDO reactions involving C3 mono-oxygenates, TMCs and TMNs have also been extensively studied for reactions involving C3 oxygenates with more than one hydroxyl groups, including 1,2-propanediol (1,2-PDO), 1,3-propanediol (1,3-PDO), and glycerol. Lin *et al.* compared the reaction pathways of 1,2-PDO, 1,3-PDO, and glycerol over a Mo_2C/Mo(110) surface and found that all three molecules underwent total C-O bond scission to produce propylene.[51] In addition, the propylene desorption peaks from glycerol and 1,2-PDO had similar shapes and peak temperatures (378 K), indicating that the HDO of both molecules occurred with similar intermediates, as verified by the HREELS measurements. In contrast, 1,3-PDO had a broader peak at higher peak temperature (533 K) from TPD and a different intermediate from HREELS, suggesting that the reaction intermediate for 1,3-PDO was different than the other two molecules. These results indicated that 1,2-PDO might be used as a surrogate molecule for glycerol in gas-phase HDO studies due to the higher vapor pressure of 1,2-PDO compared to glycerol.

Furthermore, Wan *et al.* studied the glycerol HDO reaction over Mo_2C/Mo(110) and Cu/Mo_2C/Mo(110) surfaces and discovered different reaction pathways depending on the Cu

coverage.[52] On Mo_2C/Mo(110), all C-O bonds of glycerol were cleaved to form propylene (39 amu). As the Cu coverage was increased, less propylene was formed but allyl alcohol (57 amu) and propanal (58 amu) were produced resulting from the scission of two C-O bonds of glycerol. As Cu coverage was further increased, the amount of allyl alcohol and propanal formation decreased, indicating that these two pathways were only favorable at the Cu/Mo_2C interface. In the meantime, the amount of acetol (74 amu) production increased continuously as the Cu coverage was increased. Acetol became the dominant product when Cu coverage reached greater than one monolayer (ML), suggesting that acetol production was preferred on the Cu site of the surface. The authors attributed the tunable reaction pathway to the extent of interaction between the surface and the oxygen atoms in glycerol. Mo_2C interacted with O strongly and therefore broke all the C-O bonds in glycerol. When Mo_2C was modified by sub-ML Cu, the interaction with O was weakened at the Cu-Mo_2C interface and only two C-O bonds of glycerol were cleaved as a result. When Mo_2C was fully covered by Cu, the interaction between O and the surface was further weakened and only one C-O bond of glycerol was broken to produce acetol. This work demonstrated that the oxygen binding energy on a TMC surface could be tuned with an admetal, and in turn provided a useful strategy for controlling reaction pathways to produce different HDO products.

The reaction mechanism of propylene formation from glycerol over Mo_2C has been investigated using DFT calculations.[52] Glycerol adsorbed strongly via its three oxygen atoms on three Mo atoms of a Mo-terminated Mo_2C(0001) surface with a binding energy of -2.12 eV. The higher binding energy of glycerol when compared to that of ethylene glycol over Mo_2C (0001) (-1.07 eV)[53] was ascribed to the interaction between the additional oxygen atom in glycerol and the surface, as well as the Van der Waals interactions considered during the calculations. Upon

adsorption, O-H bond scissions (E_a = 0.03 - 0.28 eV) were found to be more preferable than C-O bond scissions (E_a = 0.98 - 1.11 eV). In the subsequent step, O-H bond cleavage of the alkoxide intermediate (barriers between 0.09 and 0.20 eV) was again more favorable than C-O or C-H scissions (E_a = 0.89 – 1.30 eV), even though C-O bond scission was equally favorable by thermodynamics considerations. In the third step, the CH_2OH-CHO-CH_2O* again preferred to undergo O-H bond breaking with a substantially lower barrier (0.21 eV) than those of C-O bond cleavages (0.68 – 0.73 eV). The CH_2O-CHO-CH_2O* intermediate underwent stepwise C-O bond scissions with activation barriers of 0.48 eV (secondary C-O bond), 0.31 eV (primary C-O bond), and 0.15 eV (primary C-O bond). Compared with C-H bond scissions or O-H bond formation, the sequential C-O cleavages were more kinetically favored. The DFT-calculated optimal reaction pathway agreed well with experimental results, in which glycerol underwent three sequential C-O bond scissions to produce propylene.

The reaction pathways of glycerol on Mo_2C and Mo_2N have also been compared by Lin *et al.*.[54] On the one hand, glycerol underwent three C-O bond scissions on both Mo_2C and Mo_2N to produce propylene. This similarity was likely due to the strong interaction between the oxygen in glycerol with both surfaces. On the other hand, propylene desorbed from Mo_2C with a peak temperature of 389 K, whereas a peak temperature of 480 K was observed over Mo_2N. Aside from the production of propylene from both surfaces, glycerol also underwent scission of two C-O bonds on Mo_2N to form propanal and allyl alcohol with peak temperatures of 476 K and 418 K. The different reaction pathway over Mo_2N was attributed to the geometry of the surface where some Mo sites were blocked by N to facilitate the selective cleavage of two C-O bonds instead of all three. Overall, the combined experimental and theoretical investigations demonstrated that Mo_2C selectively broke all the C-O bonds in glycerol, 1,2-PDO, and 1,3-PDO to produce propylene. The

modification by Cu could control the cleavage of specific numbers of C-O bonds to produce value-added products such as allyl alcohol and propanal. In comparison, Mo_2N was able to not only break all the C-O bonds of glycerol to form propylene but also cleave two C-O bonds to produce allyl alcohol and propanal. In addition to C3 oxygenates, Mo_2C catalysts also showed high HDO selectivity for furfural[33] and anisole[55].

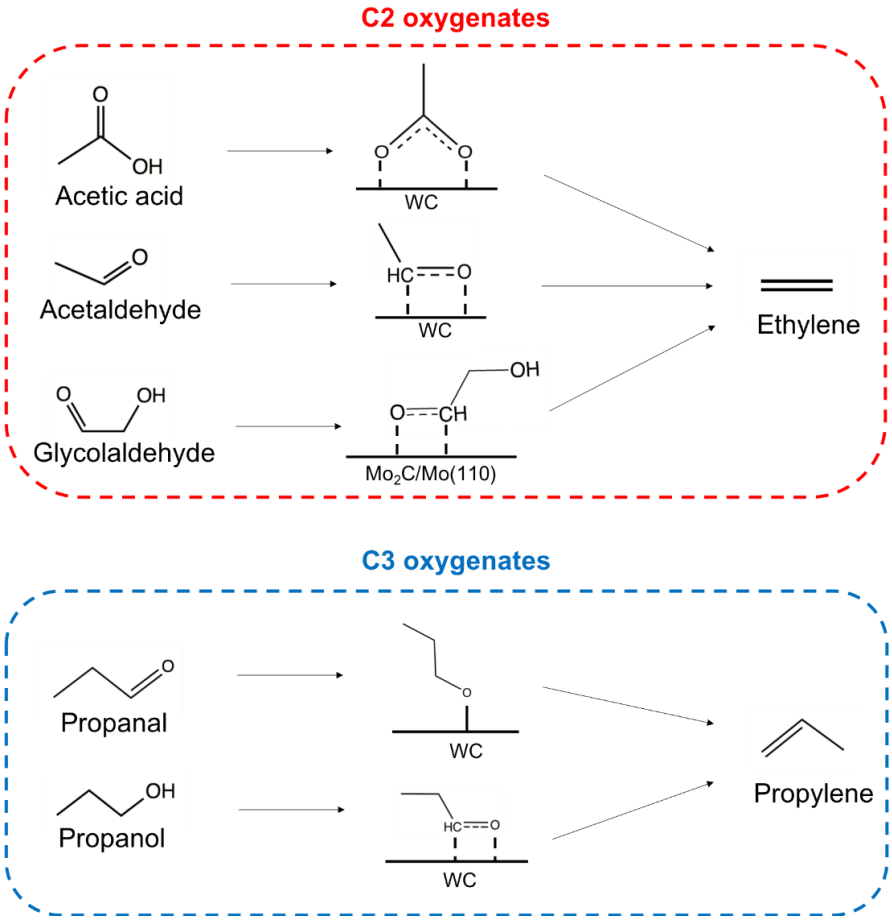

Scheme 1.1 Summary of reaction pathways of C2 and C3 oxygenates on TMC surfaces. Reproduced from Lin *et al.*,[13] with permission from The Royal Society of Chemistry. Copyright © 2018 the Royal Society of Chemistry.

Scheme 1 summarizes the pathways of the C2 and C3 oxygenates discussed. Overall, from the studies of linear C2 and C3 oxygenates, Mo_2C and WC have similar catalytic property at lower temperature (<550 K). Both carbides tend to cleave all the C-O/C=O bonds to form ethylene or propylene as the major product. HREELS observations on the reactions of the C2 and C3 oxygenates suggest that in general WC and Mo_2C interact strongly with the C-O/C=O bonds, which facilitates the cleavage of the bonds. It is also noticed that when WC is modified with Ni, the reaction pathway shifts from C-O/C=O scission toward the C-C bond scission.

1.4 HDO of Ring-Containing Oxygenates

The investigation of TMCs for HDO at low temperature and pressure has been extended to furanic oxygenates and lignin derivatives. Furanics are oxygenates containing furan rings. For example, furfural and 5-hydroxymethylfurfural are two platform furanic molecules that can be further upgraded via HDO to valuable fuels and chemicals, such as 2-methylfuran, furfuryl alcohol, dimethylfuran and levulinic acid.[3,56] The lignin fractions of lignocellulosic biomass are amorphous polymers consisting of phenolic compounds, making lignin derivatives as viable biomass sources to produce aromatic compounds via HDO. The C-C bond hydrogenation or the undesired C-C bond cleavage by hydrogenolysis can occur concurrently with HDO reactions. Due to the strong C-O bond strength (422–468 kJ mol^{-1}), it is often difficult to selectively break the C-O bond while preserving the aromatic ring. High temperature (500–700 K) and pressure (1–30 MPa) are usually used to cleave the C-O bond in an aromatic molecule and mitigate coking.[29] Due to their preference toward C-O/C=O bond scission over C-C bond cleavage, TMC catalysts have been explored for the HDO of both furanics and lignin derivatives HDO reactions. This section uses furfural and guaiacol as examples of ring-containing molecules to demonstrate the high HDO

selectivity of Mo_2C. The HDO reactions of other ring-containing molecules over TMC catalysts are also summarized.

1.4.1 C=O/C-O Bond Scission of Furfural over Mo_2C Surfaces

The hemicellulosic fragment of lignocellulosic biomass can be converted into a platform chemical known as furfural, which can be further upgraded via hydrogenation or HDO reactions to valuable chemicals, such as furfuryl alcohol, tetrahydrofurfuryl alcohol and 2-methylfuran (2-MF).[3] The conversion of furfural to 2MF, which requires selective removal of the oxygen from the C=O bond outside the furan ring, is of particular interest for fuel production.

Shi *et al.* performed DFT and microkinetic calculations to provide fundamental understanding of the HDO reaction mechanism.[34] The DFT results provide insights into the adsorption configuration, activation barrier and the effect of hydrogen partial pressure on the product selectivity. Five adsorption configurations of furfural on a $Mo_2C(101)$ surfaces are compared, including the cis- and trans-furfural. The most stable configuration is the cis-furfural absorbed via the η_2(C=O) bonding configuration with the C=O bond elongated and furan ring tilted away from the surface. Based on the optimized adsorption configuration, the subsequent activation barrier calculation on $Mo_2C(101)$ reveals that there is a critical initial step, in which the activation barriers of all possible pathways differ significantly. Two competing pathways are then identified: C-H scission to produce a F-CO intermediate that leads to furan formation and hydrogenation to produce a F-CH_2O intermediate that results in 2-MF production.

The effect of hydrogen coverage on the reaction pathways has also been calculated on hydrogen pre-covered surface. Compared to furfural on the clean Mo_2C surface, the activation barrier for each pathway changes with the increase of hydrogen coverage. The furan production pathway is no longer favored. The two competing pathways become 2-MF production and furfuryl

alcohol production, with F-CH_2O being a common intermediate for both pathways. In order to bridge the pressure gap between first-principles calculations and reactor studies, microkinetic modeling is performed to evaluate the activation barrier, reaction energy and reaction rate constant for the furfural HDO and DCO reactions over the Mo_2C surface at reaction conditions (ambient pressure or H_2-pressurized condition). It is shown that DCO (furan production) is preferred on the clean Mo_2C surface, while the HDO reaction (2-MF production) is preferred on 4H pre-covered surface, which is consistent with reactor study results that 2-MF production dominates at relatively high hydrogen partial pressure.[34]

The HDO of furfural over the Mo_2C surface has been investigated using TPD and HREELS.[33,43,45] TPD results indicate that 2-MF is the major furan ring-containing product from furfural.[33] To determine if furfuryl alcohol is an intermediate for the conversion of furfural to 2-MF, Xiong *et al.* also performed parallel TPD and HREELS measurements following the reaction of furfuryl alcohol.[33] It is found that furfuryl alcohol also produces 2-MF with a similar peak temperature as that of desorption of 2-MF produced from furfural. HREELS observations on furfural over Mo_2C suggest that furfural primarily bonds to Mo_2C via the carbonyl group.[33,43] The binding configuration changes from η_1(O) to di-σ η_2(C,O) configuration upon increasing the temperature from below 200 K to 300 K.[43] A 2-MF-like intermediate is observed when temperature is increased to 300K after dosing furfural or furfuryl alcohol onto hydrogen pre-covered Mo_2C (110).[33] This also suggests that furfural may first undergo hydrogenation on the carbonyl group to form furfuryl alcohol and then proceeds to form 2-MF, consistent with the DFT calculation.[34] The selective carbonyl C=O scission suggests that the C=O bond outside the furan ring is more reactive than that in the furan ring. The general similarity among DFT calculations, UHV experiments and

reactor studies suggests the feasibility of using model surface calculations and experiments to guide the rational design of powder catalysts.

1.4.2 DFT Calculations of Guaiacol over the TiC Surface

Guaiacol contains both phenolic and methoxyl functional groups and is reported as one of the main products from lignin depolymerization.[31] The HDO of guaiacol can be used to evaluate the catalytic activity and selectivity for the conversion of depolymerized lignin streams. DFT calculations have been performed to investigate the HDO reaction of guaiacol over a range of transition metal ceramics, including carbides.[58] The guaiacol HDO reaction energy was compared among TiO_2, TiC, TiN, TiS_2 and TiP. The TiC surface first dissociate H_2 into atomic H, which is then added to guaiacol to assist the cleavage of the C-O bond between the benzene ring and the methoxy group (Ph-OCH_3 bond). The C-O bond in the –OCH_3 group is also broken, and hydrogen is added to form CH_4 and H_2O. This deoxygenation/hydrogenation step of the -O-CH_3 group is thermodynamically favored as the reaction energy difference is over 1 eV. The resulting phenol-like intermediate subsequently undergoes C-O scission to form a benzene-like intermediate and atomic oxygen, which is then hydrogenated and desorbs as water. The benzene-like intermediate is further hydrogenated and desorb as benzene. It should be noted that in this HDO pathway, the Ph-OCH_3 bond scission is preferred over the Ph-OH bond cleavage.

In summary, the HDO reaction pathways of linear and ring-containing biomass derivatives over TMC model surfaces are compared. Due to their strong interaction with oxygen, TMC catalysts exhibit excellent C-O/C=O bond cleavage selectivity, which makes them promising catalysts for upgrading biomass-derived oxygenates. Several model compounds are used to illustrate the HDO activity over TMCs. In the case of C2 and C3 linear-chain oxygenates, Mo_2C and WC tend to cleave all the C-O/C=O bonds to produce ethylene and propylene, respectively.

As for ring-containing molecules, the location of the oxygen significantly impacts the C-O/C=O bond reactivity. For example, the C=O bond in the carbonyl group in furfural is much more reactive than the C-O bond in the furan ring. Therefore, Mo_2C selectively cleaves the carbonyl C=O bond to produce 2-MF. Despite their excellent C-O/C=O scission capability, TMCs are subject to deactivation due to the poisoning by oxygen and carbonaceous species, which interact strongly with the catalyst surface. In some cases, hydrogen is found to be capable of alleviating the deactivation by removing surface oxygen as water.

The feasibility of combining DFT calculations and microkinetic modeling with parallel experimental studies on model surfaces and powder catalysts to identify promising TMC catalysts for the HDO reaction of biomass derivatives is also demonstrated. For instance, two competing reaction pathways of furfural over Mo_2C (C-C scission and C=O scission) are identified by DFT calculation and microkinetics modeling.[34] With the increase of hydrogen partial pressure, the dominant pathway shifts from furan production (C-C scission) to 2-MF production (C=O scission), which is consistent with flow reactor results that higher hydrogen partial pressure promotes the C=O scission pathway to form 2-MF.

1.5 Dissertation Outline and Approach

TMCs, TMNs, and TMOs have all shown promising activity, selectivity, and stability for the C-O/C=O bond scission of biomass-derived oxygenates. The active sites and reaction mechanisms over these catalytic materials are distinct and are often not well understood. Therefore, it is important to study and compare these materials to gain insights that will help the rational catalyst design for desired biomass conversion reactions. In addition, theoretical calculations and surface science techniques often provide critical information regarding the intrinsic catalytic properties of materials. Therefore, this dissertation focuses on the mechanistic

studies of linear and ring-containing biomass-derived oxygenates over TMC/TMN/TMO surfaces based on first-principles Density Functional Theory (DFT) calculations and model surface experimentations. There are seven chapters in this dissertation following the Introduction Chapter.

Chapter 2 introduces the experimental and theoretical techniques for studying the HDO reactions of various biomass-derived oxygenates in this dissertation. In this chapter, techniques used for the catalytic surface preparation will be discussed in detail, which include ion sputtering, physical vapor deposition (PVD), and chemical vapor deposition (CVD) methods. Surface characterization techniques will also be discussed, which include Auger electron spectroscopy (AES) to identify surface composition, temperature programmed desorption (TPD) to collect information about gas-phase products, and high-resolution electron energy loss spectroscopy (HREELS) to determine surface intermediates. Density function theory (DFT) calculations will also be reviewed to show how it can provide useful information regarding active sites and reaction mechanisms.

Following the review of experimental and theoretical methods, Chapter 3 demonstrates an example of using Co-modifier to enhance the stability of Mo_2C for the furfural HDO reaction. Furfural is an important biomass platform chemical that can be further upgraded into various value-added chemicals and fuel additives. It is also a ring-containing molecule that has a substantially different structure than linear-chain molecules. This chapter explains how one can enhance the stability of the highly active and selective Mo_2C to achieve the production of a valuable fuel additive 2-metylfuran from furfural.

Chapter 4 then shows the design principles for tuning the reaction pathway of a linear-chain molecule, glycerol, with Cu modifications. Since the three oxygen atoms in glycerol are in a similar chemical environment as compared to those in furfural, modifications need to be made

to achieve the selective scission of specific numbers of C-O bonds to form different valuable products. Cu modifications demonstrate tunable reaction pathways based on the admetal coverage. Despite the promising results, the low vapor pressure of glycerol hinders the experimentation at ambient pressure and therefore the correlation between model surface experiments under ultrahigh vacuum (UHV) conditions and the studies of industrial-relevant powder catalysts. In order to address this issue, this chapter also demonstrates the feasibility of using 1,2-propanediol as a surrogate for glycerol for vapor-phase mechanistic study using powder catalysts.

Chapters 3 and 4 illustrate the promising and tunable catalytic properties of Mo_2C for the HDO reaction of both ring-containing and linear-chain molecules, and that one can use a surrogate molecule to facilitate the vapor-phase mechanistic studies of glycerol at ambient pressure. Chapter 5 compares the selective HDO reaction of glycerol over Mo_2N and Mo_2C. It is shown that Mo_2N not only cleaves three C-O bonds of glycerol to form propylene as Mo_2C does, but also breaks two C-O bonds to produce allyl alcohol and propanal, which is only observed on the Cu/Mo_2C interface but not on Mo_2C.

Following the comparison between TMC and TMN surfaces, Chapter 6 discusses the reaction pathways of glycerol over an inverse oxide model surface, $WO_x/Pt(111)$, and reveals active sites and reaction mechanisms that are completely different from those of TMCs and TMNs. It is shown that Pt sites catalyze the hydrogenation reaction, whereas WO_x sites promote the dehydrogenation reaction due to the presence of hydroxyl groups on the surface. Strategies for tuning the active sites on the surface are also discussed based on the DFT predictions on *in situ* generated Bronsted acid sites.

Chapter 7 then summarizes the studies on transition metal carbide, nitride and oxide surfaces discussed in this dissertation. By comparing the three types of catalytic surfaces, insights

into application-dependent rational catalyst design are gained. This chapter also points out future research directions. For example, the inverse oxide design used in Chapter 6 can be extended to the studies of relevant metal oxide/metal systems to reveal the intrinsic catalytic properties at the interface. It is also pointed out that the combination of first-principles DFT calculations, model surface experiments, and *in situ* characterization using ambient-pressure X-ray photoelectron spectroscopy (XPS) and X-ray adsorption (XAS) techniques provides in-depth understanding regarding the active sites and reaction mechanisms and should be used whenever possible. Furthermore, with the recent advances of machine learning in catalysis, it is possible to combine machine learning with multiscale modeling (DFT, microkinetics modeling, kinetic Monte Carlo simulations, and molecular dynamic simulations) to accelerate the identification of optimal compositions of TMC/TMN/TMO catalytic materials.

1.6 Acknowledgements

Reproduced from *Lin, Z., Chen, R., Qu, Z. & Chen, J. G. Hydrodeoxygenation of biomass-derived oxygenates over metal carbides: from model surfaces to powder catalysts. Green Chem. 20, 2679–2696 (2018)* by permission of The Royal Society of Chemistry, Copyright © 2018 Royal Society of Chemistry. I acknowledge Dr. Rui Chen, Dr. Zhenping Qu for their assistance in paper writing. Chapter 1 also contains part of the manuscript *Lin, Z., Denny, S. R. & Chen, J. G. Transition Metal Carbides and Nitrides as Catalysts for Thermochemical Reactions. (Manuscript under Review).* I acknowledge Steven Denny for his assistance in paper writing.

1.7 References

(1) Chheda, J. N.; Huber, G. W.; Dumesic, J. A. Liquid-Phase Catalytic Processing of Biomass-Derived Oxygenated Hydrocarbons to Fuels and Chemicals. *Angew. Chemie - Int. Ed.* **2007**, *46* (38), 7164–7183. https://doi.org/10.1002/anie.200604274.

(2) Wettstein, S. G.; Martin Alonso, D.; Gürbüz, E. I.; Dumesic, J. A. A Roadmap for Conversion of Lignocellulosic Biomass to Chemicals and Fuels. *Curr. Opin. Chem. Eng.* **2012**, *1* (3), 218–224. https://doi.org/10.1016/j.coche.2012.04.002.

(3) Lange, J. P.; Van Der Heide, E.; Van Buijtenen, J.; Price, R. Furfural-A Promising Platform for Lignocellulosic Biofuels. *ChemSusChem* **2012**, *5* (1), 150–166. https://doi.org/10.1002/cssc.201100648.

(4) Xiong, K.; Yu, W.; Vlachos, D. G.; Chen, J. G. Reaction Pathways of Biomass-Derived Oxygenates over Metals and Carbides: From Model Surfaces to Supported Catalysts. *ChemCatChem* **2015**, *7* (9), 1402–1421. https://doi.org/10.1002/cctc.201403067.

(5) Levy, R. B.; Boudart, M. Platinum-Like Behavior of Tungsten Carbide in Surface Catalysis. *Science (80-.).* **1973**, *181* (4099), 547–549. https://doi.org/10.1126/science.181.4099.547.

(6) Oyama, S. T. Preparation and Catalytic Properties of Transition Metal Carbides and Nitrides. *Catal. Today* **1992**, *15* (2), 179–200. https://doi.org/10.1016/0920-5861(92)80175-M.

(7) Johansson, L. I. Electronic and Structural Properties of Transition-Metal Carbide and Nitride Surfaces. *Surf. Sci. Rep.* **1995**, *21* (5–6), 177–250. https://doi.org/10.1016/0167-5729(94)00005-0.

(8) Chen, J. G. Carbide and Nitride Overlayers on Early Transition Metal Surfaces: Preparation, Characterization, and Reactivities. *Chem. Rev.* **1996**, *96*, 1477–1498. https://doi.org/10.1021/cr950232u.

(9) Hwu, H. H.; Chen, J. G. Surface Chemistry of Transition Metal Carbides. *Chem. Rev.* **2005**, *105*, 185–212. https://doi.org/10.1021/cr0204606.

(10) Kitchin, J. R.; Nørskov, J. K.; Barteau, M. A.; Chen, J. G. Trends in the Chemical Properties of Early Transition Metal Carbide Surfaces: A Density Functional Study. *Catal. Today* **2005**, *105* (1 SPEC. ISS.), 66–73. https://doi.org/10.1016/j.cattod.2005.04.008.

(11) Frühberger, B.; Chen, J. G. Reaction of Ethylene with Clean and Carbide-Modified Mo(110): Converting Surface Reactivities of Molybdenum to Pt-Group Metals. *J. Am. Chem. Soc.* **1996**, *118* (46), 11599–11609. https://doi.org/10.1021/ja960656l.

(12) Stottlemyer, A. L.; Kelly, T. G.; Meng, Q.; Chen, J. G. Reactions of Oxygen-Containing Molecules on Transition Metal Carbides: Surface Science Insight into Potential Applications in Catalysis and Electrocatalysis. *Surf. Sci. Rep.* **2012**, *67* (9–10), 201–232. https://doi.org/10.1016/j.surfrep.2012.07.001.

(13) Lin, Z.; Chen, R.; Qu, Z.; Chen, J. G. Hydrodeoxygenation of Biomass-Derived Oxygenates over Metal Carbides: From Model Surfaces to Powder Catalysts. *Green Chem.* **2018**, *20* (12), 2679–2696. https://doi.org/10.1039/C8GC00239H.

(14) Goulas, K. A.; Mironenko, A. V.; Jenness, G. R.; Mazal, T.; Vlachos, D. G. Fundamentals of C–O Bond Activation on Metal Oxide Catalysts. *Nat. Catal.* **2019**, *2* (3), 269–276. https://doi.org/10.1038/s41929-019-0234-6.

(15) He, Z.; Wang, X. Renewable Energy and Fuel Production over Transition Metal Oxides: The Role of Oxygen Defects and Acidity. *Catal. Today* **2015**, *240* (PB), 220–228. https://doi.org/10.1016/j.cattod.2014.04.023.

(16) Yu, W.; Salciccioli, M.; Xiong, K.; Barteau, M. A.; Vlachos, D. G.; Chen, J. G. SI-Theoretical and Experimental Studies of C-C versus C-O Bond Scission of Ethylene Glycol Reaction Pathways via Metal-Modified Molybdenum Carbides. *ACS Catal.* **2014**, *4* (5), 1409–1418. https://doi.org/10.1021/cs500124n.

(17) Ren, H.; Chen, Y.; Huang, Y.; Deng, W.; Vlachos, D. G.; Chen, J. G. Tungsten Carbides as Selective Deoxygenation Catalysts: Experimental and Computational Studies of Converting C3 Oxygenates to Propene. *Green Chem.* **2014**, *16* (2), 761–769. https://doi.org/10.1039/C3GC41256C.

(18) Ren, H.; Yu, W.; Salciccioli, M.; Chen, Y.; Huang, Y.; Xiong, K.; Vlachos, D. G.; Chen, J. G. Selective Hydrodeoxygenation of Biomass-Derived Oxygenates to Unsaturated Hydrocarbons Using Molybdenum Carbide Catalysts. *ChemSusChem* **2013**, *6* (5), 798–801. https://doi.org/10.1002/cssc.201200991.

(19) Schaidle, J. A.; Blackburn, J.; Farberow, C. A.; Nash, C.; Steirer, K. X.; Clark, J.; Robichaud, D. J.; Ruddy, D. A. Experimental and Computational Investigation of Acetic Acid Deoxygenation over Oxophilic Molybdenum Carbide: Surface Chemistry and Active Site Identity. *ACS Catal.* **2016**, *6* (2), 1181–1197. https://doi.org/10.1021/acscatal.5b01930.

(20) Sullivan, M. M.; Bhan, A. Acetone Hydrodeoxygenation over Bifunctional Metallic-Acidic Molybdenum Carbide Catalysts. *ACS Catal.* **2016**, *6* (2), 1145–1152. https://doi.org/10.1021/acscatal.5b02656.

(21) Gosselink, R. W.; Stellwagen, D. R.; Bitter, J. H. Tungsten-Based Catalysts for Selective Deoxygenation. *Angew. Chemie - Int. Ed.* **2013**, *52* (19), 5089–5092. https://doi.org/10.1002/anie.201209809.

(22) Han, J.; Duan, J.; Chen, P.; Lou, H.; Zheng, X. Molybdenum Carbide-Catalyzed Conversion of Renewable Oils into Diesel-like Hydrocarbons. *Adv. Synth. Catal.* **2011**, *353* (14–15), 2577–2583. https://doi.org/10.1002/adsc.201100217.

(23) Hollak, S. A. W.; Gosselink, R. W.; Van Es, D. S.; Bitter, J. H. Comparison of Tungsten and Molybdenum Carbide Catalysts for the Hydrodeoxygenation of Oleic Acid. *ACS Catal.* **2013**, *3* (12), 2837–2844. https://doi.org/10.1021/cs400744y.

(24) Kim, S. K.; Yoon, D.; Lee, S. C.; Kim, J. Mo<inf>2</Inf>C/Graphene Nanocomposite as a Hydrodeoxygenation Catalyst for the Production of Diesel Range Hydrocarbons. *ACS Catal.* **2015**, *5* (6), 3292–3303. https://doi.org/10.1021/acscatal.5b00335.

(25) Stellwagen, D. R.; Bitter, J. H. Structure–Performance Relations of Molybdenum- and Tungsten Carbide Catalysts for Deoxygenation. *Green Chem.* **2015**, *17* (1), 582–593. https://doi.org/10.1039/C4GC01831A.

(26) Liang, J.; Ding, R.; Wu, Y.; Chen, Y.; Wu, K.; Meng, Y.; Yang, M.; Wang, Y. Effective Conversion of Heteroatomic Model Compounds in Microalgae-Based Bio-Oils to Hydrocarbons over β-Mo2C/CNTs Catalyst. *J. Mol. Catal. A Chem.* **2016**, *411*, 95–102. https://doi.org/10.1016/j.molcata.2015.10.018.

(27) Qin, Y.; Chen, P.; Duan, J.; Han, J.; Lou, H.; Zheng, X.; Hong, H. Carbon Nanofibers Supported Molybdenum Carbide Catalysts for Hydrodeoxygenation of Vegetable Oils. *RSC Adv.* **2013**, *3* (38), 17485. https://doi.org/10.1039/c3ra42434k.

(28) Han, J.; Duan, J.; Chen, P.; Lou, H.; Zheng, X.; Hong, H. Nanostructured Molybdenum Carbides Supported on Carbon Nanotubes as Efficient Catalysts for One-Step Hydrodeoxygenation and Isomerization of Vegetable Oils. *Green Chem.* **2011**, *13* (9), 2561. https://doi.org/10.1039/c1gc15421d.

(29) Lee, W. S.; Wang, Z.; Wu, R. J.; Bhan, A. Selective Vapor-Phase Hydrodeoxygenation of Anisole to Benzene on Molybdenum Carbide Catalysts. *J. Catal.* **2014**, *319*, 44–53. https://doi.org/10.1016/j.jcat.2014.07.025.

(30) Iida, T.; Shetty, M.; Murugappan, K.; Wang, Z.; Ohara, K.; Wakihara, T.; Román-Leshkov, Y. Encapsulation of Molybdenum Carbide Nanoclusters inside Zeolite Micropores Enables Synergistic Bifunctional Catalysis for Anisole Hydrodeoxygenation. *ACS Catal.* **2017**, *7*, 8147–8151. https://doi.org/10.1021/acscatal.7b03175.

(31) Jongerius, A. L.; Gosselink, R. W.; Dijkstra, J.; Bitter, J. H.; Bruijnincx, P. C. A.; Weckhuysen, B. M. Carbon Nanofiber Supported Transition-Metal Carbide Catalysts for the Hydrodeoxygenation of Guaiacol. *ChemCatChem* **2013**, *5* (10), 2964–2972. https://doi.org/10.1002/cctc.201300280.

(32) Moreira, R.; Ochoa, E.; Luis Pinilla, J.; Portugal, A.; Suelves, I. Liquid-Phase Hydrodeoxygenation of Guaiacol over Mo 2 C Supported on Commercial CNF. Effects of Operating Conditions on Conversion and Product Selectivity. *Catalysts* **2018**, *8*, 127.

https://doi.org/10.3390/catal8040127.

(33) Xiong, K.; Lee, W. S.; Bhan, A.; Chen, J. G. Molybdenum Carbide as a Highly Selective Deoxygenation Catalyst for Converting Furfural to 2-Methylfuran. *ChemSusChem* **2014**, *7* (8), 2146–2149. https://doi.org/10.1002/cssc.201402033.

(34) Shi, Y.; Yang, Y.; Li, Y.-W.; Jiao, H. Mechanisms of Mo 2 C(101)-Catalyzed Furfural Selective Hydrodeoxygenation to 2-Methylfuran from Computation. *ACS Catal.* **2016**, *6*, 6790–6803. https://doi.org/10.1021/acscatal.6b02000.

(35) Jiang, Z.; Wan, W.; Lin, Z.; Xie, J.; Chen, J. G. Understanding the Role of M/Pt(111) (M=Fe, Co, Ni, Cu) Bimetallic Surfaces for Selective Hydrodeoxygenation of Furfural. *ACS Catal.* **2017**, *7* (9), 5758–5765. https://doi.org/10.1021/acscatal.7b01682.

(36) Wan, W.; Jiang, Z.; Chen, J. G. A Comparative Study of Hydrodeoxygenation of Furfural Over Fe/Pt(111) and Fe/Mo2C Surfaces. *Top. Catal.* **2018**. https://doi.org/10.1007/s11244-018-0901-x.

(37) R. B. Levy; M. Boudart. Platinum-Like Behavior of Tungsten Carbide in Surface Catalysis. *Science (80-.).* **1973**, *181* (4099), 547–549.

(38) Tripathi, C. C.; Kumar, M.; Kumar, D. Atom Beam Sputtered Mo2C Films as a Diffusion Barrier for Copper Metallization. *Appl. Surf. Sci.* **2009**, *255* (6), 3518–3522. https://doi.org/10.1016/j.apsusc.2008.09.076.

(39) Lin, Z.; Wan, W.; Yao, S.; Chen, J. G. Cobalt-Modified Molybdenum Carbide as a Selective Catalyst for Hydrodeoxygenation of Furfural. *Appl. Catal. B Environ.* **2018**, *233*, 160–166. https://doi.org/10.1016/j.apcatb.2018.03.113.

(40) Sullivan, M. M.; Chen, C.-J.; Bhan, A. Catalytic Deoxygenation on Transition Metal Carbide Catalysts. *Catal. Sci. Technol.* **2016**, *6*, 602–616. https://doi.org/10.1039/C5CY01665G.

(41) Robinson, A. M.; Hensley, J. E.; Will Medlin, J. Bifunctional Catalysts for Upgrading of Biomass-Derived Oxygenates: A Review. *ACS Catal.* **2016**, *6* (8), 5026–5043. https://doi.org/10.1021/acscatal.6b00923.

(42) Yu, W.; Mellinger, Z. J.; Barteau, M. A.; Chen, J. G. Comparison of Reaction Pathways of Ethylene Glycol, Acetaldehyde, and Acetic Acid on Tungsten Carbide and Ni-Modified Tungsten Carbide Surfaces. *J. Phys. Chem. C* **2012**, *116* (9), 5720–5729. https://doi.org/10.1021/jp210756f.

(43) McManus, J. R.; Vohs, J. M. Deoxygenation of Glycolaldehyde and Furfural on Mo_2C/Mo(100). *Surf. Sci.* **2014**, *630*, 16–21. https://doi.org/10.1016/j.susc.2014.06.019.

(44) Serrano-Ruiz, J. C.; Dumesic, J. A. Catalytic Routes for the Conversion of Biomass into Liquid Hydrocarbon Transportation Fuels. *Energy Environ. Sci.* **2011**, *4*, 83. https://doi.org/10.1039/c0ee00436g.

(45) Xiong, K.; Yu, W.; Chen, J. G. Selective Deoxygenation of Aldehydes and Alcohols on Molybdenum Carbide (Mo_2C) Surfaces. *Appl. Surf. Sci.* **2014**, *323*, 88–95. https://doi.org/10.1016/j.apsusc.2014.06.100.

(46) Davis, J. L.; Barteau, A. Polymerization and Decarbonylation Reactions of Aldehydes on the Pd(111) Surface. *J. Am. Chem. Soc* **1989**, *111*, 1782–1792. https://doi.org/10.1021/ja00187a035.

(47) Murillo, L. E.; Chen, J. G. Adsorption and Reaction of Propanal, 2-Propenol and 1-Propanol on Ni/Pt(111) Bimetallic Surfaces. *Surf. Sci.* **2008**, *602* (14), 2412–2420. https://doi.org/10.1016/j.susc.2008.05.026.

(48) Brown, N. F.; Barteau, M. A. Reactions of 1-Propanol and Propionaldehyde on Rh(111). *Langmuir* **1992**, *8* (3), 862–869. https://doi.org/10.1021/la00039a021.

(49) Gutierrez, A.; Kaila, R. K.; Honkela, M. L.; Slioor, R.; Krause, A. O. I. Hydrodeoxygenation of Guaiacol on Noble Metal Catalysts. *Catal. Today* **2009**, *147*, 239. https://doi.org/10.1016/j.cattod.2008.10.037.

(50) Peng, B.; Zhao, C.; Mejía-Centeno, I.; Fuentes, G. A.; Jentys, A.; Lercher, J. A. Comparison of Kinetics and Reaction Pathways for Hydrodeoxygenation of C3 Alcohols on Pt/Al_2O_3. *Catal. Today* **2012**, *183*, 3–9. https://doi.org/10.1016/j.cattod.2011.10.022.

(51) Lin, Z.; Wan, W.; Chen, J. G. 1,2-Propanediol as a Surrogate Molecule of Glycerol for Mechanistic Studies of Selective Hydrodeoxygenation Reactions over Mo_2C and Cu/Mo_2C Surfaces. *ACS Sustain. Chem. Eng.* **2019**, *7*, 8077–8082. https://doi.org/10.1021/acssuschemeng.9b01051.

(52) Wan, W.; Ammal, S. C.; Lin, Z.; You, K.-E.; Heyden, A.; Chen, J. G. Controlling Reaction Pathways of Selective C–O Bond Cleavage of Glycerol. *Nat. Commun.* **2018**, *9* (1), 4612. https://doi.org/10.1038/s41467-018-07047-7.

(53) Yu, W.; Salciccioli, M.; Xiong, K.; Barteau, M. A.; Vlachos, D. G.; Chen, J. G. Theoretical and Experimental Studies of C-C versus C-O Bond Scission of Ethylene Glycol Reaction Pathways via Metal-Modified Molybdenum Carbides. *ACS Catal.* **2014**, *4* (5), 1409–1418. https://doi.org/10.1021/cs500124n.

(54) Lin, Z.; Ammal, S. C.; Denny, S. R.; Rykov, S.; You, K.-E.; Heyden, A.; Chen, J. G. Controlling Extent of C-O Bond Scission of Glycerol over Molybdenum Nitride Surfaces. (Manuscript in Preparation).

(55) Lu, Q.; Chen, C. J.; Luc, W.; Chen, J. G.; Bhan, A.; Jiao, F. Ordered Mesoporous Metal Carbides with Enhanced Anisole Hydrodeoxygenation Selectivity. *ACS Catal.* **2016**, *6* (6), 3506–3514. https://doi.org/10.1021/acscatal.6b00303.

(56) Rosatella, A. A.; Simeonov, S. P.; Frade, R. F. M.; Afonso, C. A. M. 5-Hydroxymethylfurfural (HMF) as a Building Block Platform: Biological Properties, Synthesis and Synthetic Applications. *Green Chem.* **2011**, *13* (4), 754. https://doi.org/10.1039/c0gc00401d.

(57) Lee, W.-S.; Wang, Z.; Zheng, W.; Vlachos, D. G.; Bhan, A. Vapor Phase Hydrodeoxygenation of Furfural to 2-Methylfuran on Molybdenum Carbide Catalysts. *Catal. Sci. Technol.* **2014**, *4* (8), 2340. https://doi.org/10.1039/c4cy00286e.

(58) He, Y.; Laursen, S. Trends in the Surface and Catalytic Chemistry of Transition-Metal Ceramics in the Deoxygenation of a Woody Biomass Pyrolysis Model Compound. *ACS Catal.* **2017**, *7* (5), 3169–3180. https://doi.org/10.1021/acscatal.6b02806.

Chapter 2: Experimental and Theoretical Methods

2.1 Overview

In this dissertation, model surface experiments and theoretical calculations are used to investigate the intrinsic catalytic properties of materials. Due to the complexity of industrial powder catalysts that involves heat and mass transport processes and reaction on multiple facets, fundamental understandings regarding the intrinsic kinetics are difficult to obtain. Surface science experimentations and first-principles calculations on well-define model surfaces under ideal conditions (*e.g.*, ultrahigh vacuum) are therefore necessary to overcome this difficulty. This chapter will introduce surface preparation methods, surface science techniques, and first-principles density functional theory (DFT) calculations that are commonly used for the studies presented in Chapters 3 – 6.

2.2 Surface Preparation

Single crystals and thin films studied in this dissertation are cleaned by Ne^+ sputtering and annealing. The surface purity is verified by the elemental composition detected using Auger electron spectroscopy (AES). The synthesis of catalytic systems of interest are usually conducted using physical vapor deposition (PVD) or chemical vapor deposition (CVD) methods. The sections below describe the two deposition processes.

2.2.1 Physical Vapor Deposition

Physical vapor deposition (PVD) is used for depositing metal overlayers on carbide and nitride surfaces. The setup for PVD is shown in Figure 2.1. A wire of the metal to be deposited is reeled around a tungsten coil that is attached to a DC power supply. The metal source is covered with a shield to direct the metal vapor to the surface. During the PVD process, the substrate is

maintained at a designated temperature depending on the application, and placed in front of the metal source, which is heated with a current high enough to facilitate the deposition at a reasonable rate.

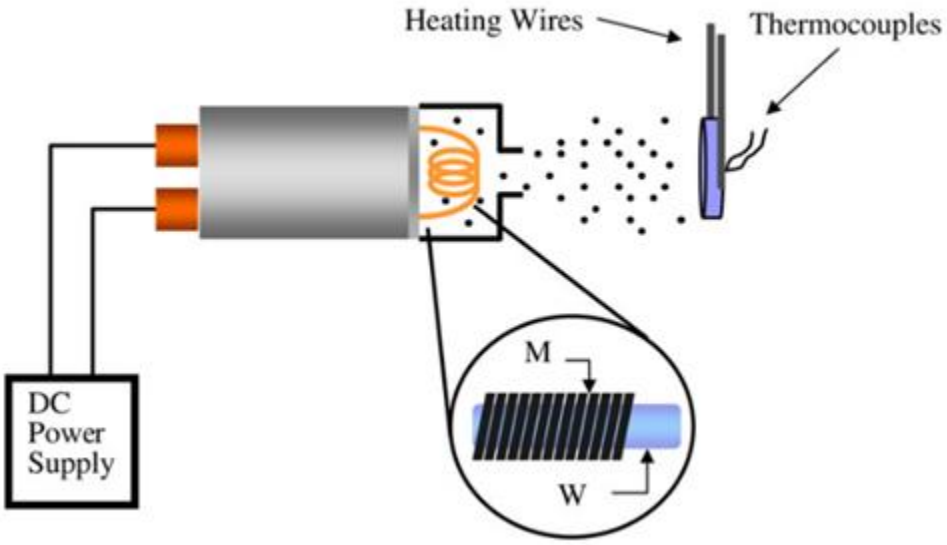

Figure 2.1 Setup for physical vapor deposition. Reprinted from Chen *et al.*,[1] Copyright © 2008 Elsevier.

The growth mechanism of the metal overlayer can differ depending on the type of substrate and admetal. As illustrated in Figure 2.1, the admetal can grow in a layer-by-layer fashion by the Frank van der Merwe growth mechanism, or in a 3-dimensional (3-D) island fashion following the Volmer–Weber (VW) mechanism.[1] The determining factor is the cohesive energy between overlayer metal atoms in relation to the binding energy between the overlayer atoms and the substrate. If the former is larger, then 3-D island formation will be more favorable than the layer-by-layer growth mechanism, and vice versa.

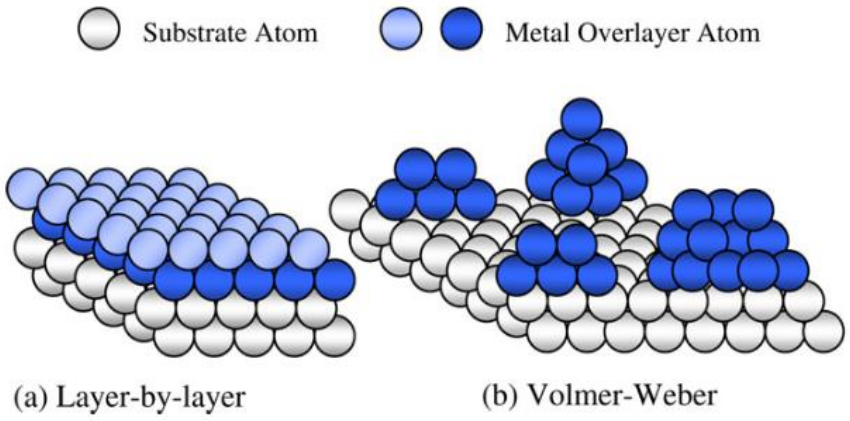

Figure 2.2 Growth mechanism of metal overlayer. Reprinted from Chen *et al.*,[1] Copyright © 2008 Elsevier.

The growth mechanism can be characterized using Auger Electron Spectroscopy (AES), as will be mentioned in Section 2.3.1. The AES peak-to-peak intensity of the admetal and the substrate can be plotted as a function of the deposition time. Distinct breakpoints will be observed in the case of layer-by-layer growth (Figure 2.3 a) but not with 3-D island formation (Figure 2.3 b). The first breakpoint also indicates the completion of the first monolayer, and can be used to determine the time needed for the deposition of a monolayer of admetal.[1]

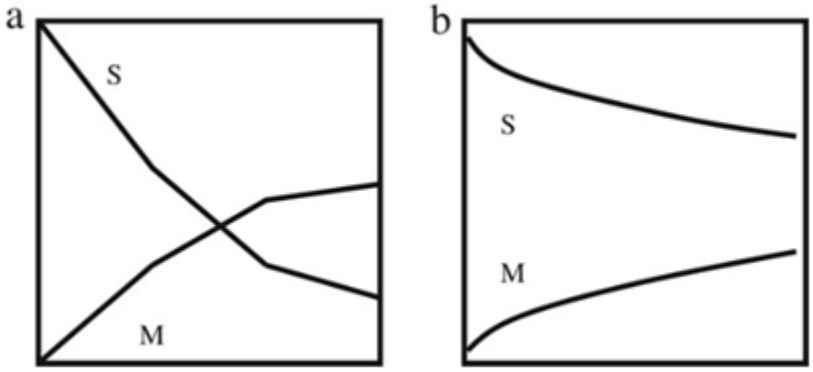

Figure 2.3 AES characterization of growth mechanism: peak-to-peak intensity of admetal and substrate as a function of deposition time. Reprinted from Chen *et al.*,[1] Copyright © 2008 Elsevier.

2.2.2 Chemical Vapor Deposition

Chemical vapor deposition is used to prepare WO_x/Pt(111) surfaces. The deposition of WO_x utilizes the $W(CO)_6$ precursor, which is adsorbed onto Pt(111) at liquid nitrogen temperature. In order to facilitate the vaporization of the solid $W(CO)_6$ precursor, the entire gas line from the sample cylinder to the gate valve is heated to and maintained at above 413 K during the deposition process. Mass spectrometry is used to monitor the dosing of $W(CO)_6$. AES measurements are taken to confirm the presence of W on the surface. Then, the surface is exposed to $5*10^{-7}$ Torr of O_2 and heated to 573 K at 0.5 K/s and held there for 30 minutes to oxidize the decomposed tungsten on the surface. Once WO_x forms on the surface after the 30-minute oxidation process, the surface is heated to 950 K in the same oxygen environment to remove excess carbon, followed by an AES measurement to confirm the presence of W, O and, Pt on the surface. Before the surface is exposed to reactants, it is reduced at 473 K in $5*10^{-8}$ H_2 for 10 min.

2.3 Experimental Techniques

2.3.1 Auger Electron Spectroscopy

Auger Electron Spectroscopy (AES) is used to identify the surface elemental composition and their characteristics.[1] In this thesis, a cylindrical mirror analyzer (CMA) was used for AES measurements. During a measurement, the sample of interest is placed in front of the AES, with the distance depending on the particular CMA device. An electron beam (typically with an energy of 3 keV) is directed towards the sample to initiate the Auger process (Figure 2.4). During the Auger process, a core electron of the surface element is knocked out by the incoming electron beam. At the same time, an electron from a higher energy level fills in the core hole, releasing energy that promoted the emission of an electron in an even higher energy level. This ejected electron carries energy that is elemental-specific, which can be used to determine the identity and

concentration of the surface elements. The ejected electron goes through a parabolic trajectory and is collected by the electron detector, on which a spectrum is recorded. Typically, the spectrum is differentiated for analysis. The peak location informs the identity of the element (*e.g.*, Pt, Fe, Mo, *etc.*), and the peak-to-peak height informs the concentration of the element when normalized by a sensitivity factor and divided by the sum of the normalized peak-to-peak height of all elements.

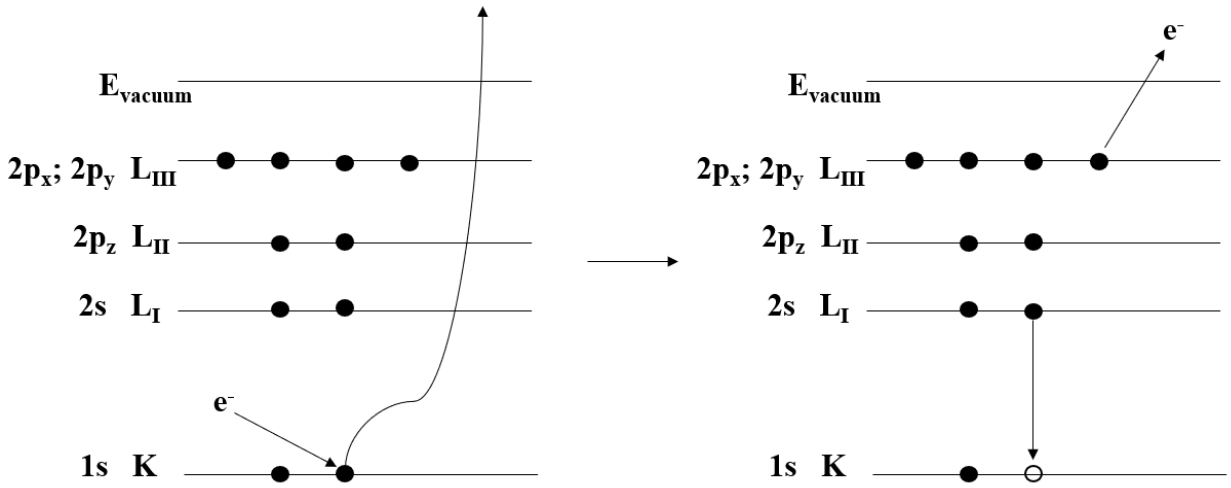

Figure 2.4 Schematic of the Auger process that involves three electron transfer.

The kinetic energy of the ejected Auger electron can be calculated with Equation 2.1, where E_k, E_{L_I}, $E_{L_{III}}$, and E_v are the energies of the core electrons, electrons on the L_I orbital, electrons on the L_{III} orbital, and electrons in vacuum. This kinetic energy is elemental specific and is independent of the energy of the incident beam.

$$Kinetic\ Energy = \left(E_k - E_{L_I}\right) - \left(E_{L_{III}} - E_{vac}\right) \tag{2.1}$$

Equation 2.2 shows the method for estimating the coverage of an overlayer.[2] I_A, S_A and I_B, S_B are the peak-to-peak intensities and sensitivity factors of the overlayer and the substrate, respectively. The atomic diameter of the overlayer atom is represented by d. $\lambda_{imfp}^{A}(E_A)$ and $\lambda_{imfp}^{B}(E_B)$ are the mean-free-paths of electrons at the peak energies of element A and B,

respectively. Cos(θ) is the emission angle from surface normal, which is specific to the CMA. This method is used in this dissertation for estimating the metal overlayer coverages, the trend of which is verified by experiments.

$$\frac{\frac{I_A}{s_A}}{\frac{I_B}{s_B}} = \frac{1-\exp\left[\frac{-d}{\lambda^A_{\mathrm{imfp}}(E_A)\cos\theta}\right]}{\exp\left[\frac{-d}{\lambda^A_{\mathrm{imfp}}(E_B)\cos\theta}\right]} \tag{2.2}$$

2.3.2 Temperature-Programmed Desorption

Temperature-Programmed Desorption (TPD) is a technique that measures the desorption of gas-phase molecules when a surface pre-dosed with reactant is heated up. Typically, the catalytic material is exposed to reactants at a low enough temperature to facilitate adsorption, followed by subsequent heating at a linear rate in front of a mass spectrometer that records the TPD spectra. The information that TPD experiments provides include the identity of the gas phase products based on the m/e ratio, the concentration of the products based on the peak area, the adsorption strength or activation barrier of product formation based on the peak temperature, and the desorption order based on the peak shape.[3] The desorption process can be modeled using Equation 2.3, where r_d is the desorption rate, which is indicated by the mass spec intensity experimentally; k_d is the desorption rate constant; θ is the coverage. Clearly, r_d is proportional to the product of k_d and θ, both of which are functions of temperature. This equation in fact explains the origin of TPD peaks as shown in Figure 2.5.[3] While θ decreases with temperature, k_d increases with temperature. Therefore, the product of the two appears as a peak, indicating that r_d starts from zero and increases with temperature initially. After reaching a maximum value, r_d starts to decrease and eventually goes back to zero as θ reaches zero.

In fact, further analysis with the desorption kinetics using the Redhead equation provides quantitative information regarding the activation energy for desorption for unactivated adsorption

processes. In the Redhead analysis,[4] after establishing the relationship between temperature (T) and time (t) using Equation 2.4, the derivative of θ with respect to T is set to zero at the peak temperature (Equation 2.5). This allows the derivation of Equation 2.6 that can be used to estimate the activation barrier for desorption given the peak temperature. In the special case for first-order desorption with a heating rate of 3 K/s and a pre-exponential factor of $1*10^{13}$ s^{-1}, the equation can be further simplified to the following: $E_a = 0.06*T_p$, where E_a is the activation energy for desorption in kcal/mol and T_p is peak temperature in Kelvin (K). Such simplification allows one to quickly estimate E_a, which is very helpful for data analysis and experiment design.

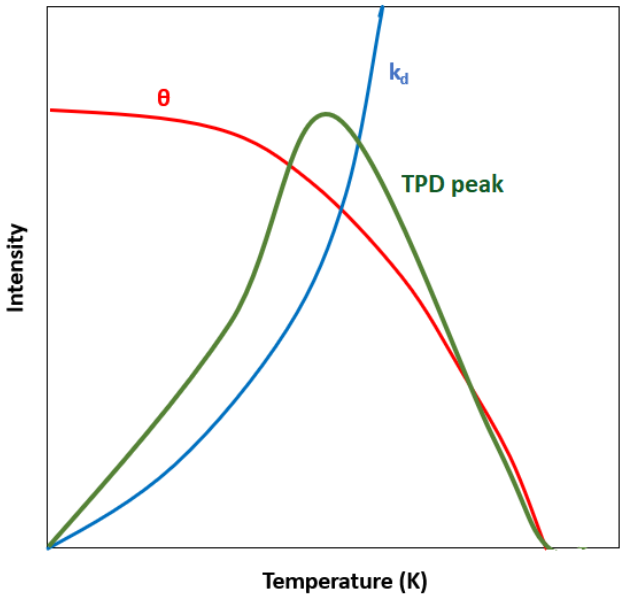

Figure 2.5 Origin of a TPD peak with contributions from θ and k_d.

$$r_d = -N_s \frac{d\theta}{dt} = k_d (N_s \theta)^n = k_0 (N_s \theta)^n \exp\left(-\frac{E_A}{RT}\right) \quad (2.3)$$

$$T = T_0 + \beta_H t \quad (2.4)$$

$$\left.\frac{dr_d}{dT}\right|_{T=T_P} = 0 \quad (2.5)$$

$$k_0 n\theta_P^{n-1} \exp\left(-\frac{E_A}{\mathrm{R}T_p}\right) = \frac{\beta_H E_A}{RT_P^2} \quad (2.6)$$

2.3.3 High-Resolution Electron Energy Loss Spectroscopy

High-resolution electron energy loss spectroscopy (HREELS) is a technique that uses electrons to excite chemical bonds within molecules to detect the associated vibrational modes by means of dipole scattering and impact scattering. The detectability of dipole moments on catalyst surfaces follows the surface dipole selection rules,[5] as shown in Figure 2.6. A dipole moment that is parallel to the surface will induce an opposite dipole moment on the surface, and thereby the net dipole moment will be zero. Nonetheless, when a dipole moment is aligned in a perpendicular configuration to the surface, the induced dipole moment will be of the same direction and strength as the original dipole moment, and therefore the net dipole moment is twice that of the original dipole moment. In the case where the dipole moment is at some angle (neither parallel or perpendicular) to the surface, the net dipole moment equals to the perpendicular component to the surface, the magnitude of which is $2\mu\cos(\theta)$, where μ is magnitude of the original dipole moment, and θ is the angle between the original dipole moment and surface normal.

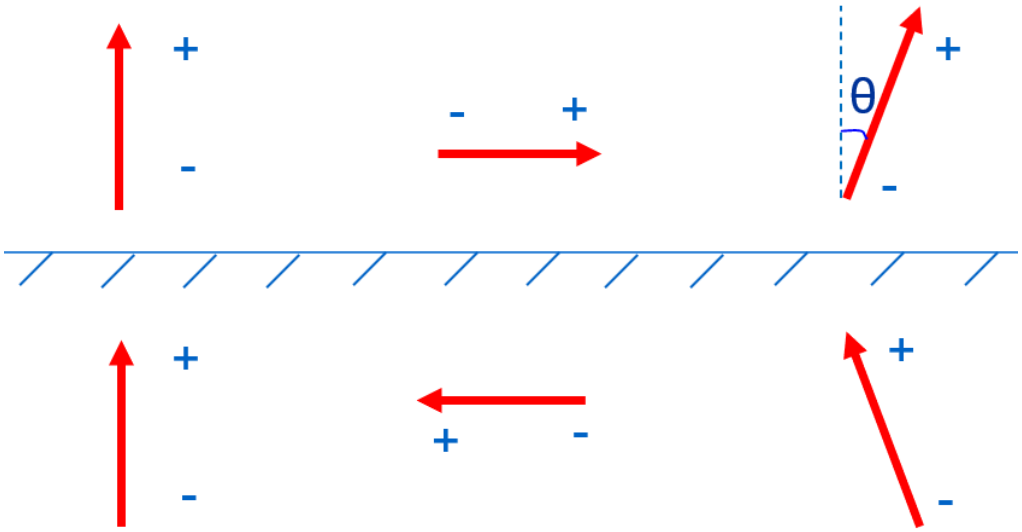

Figure 2.6 Surface Dipole Selection Rule.

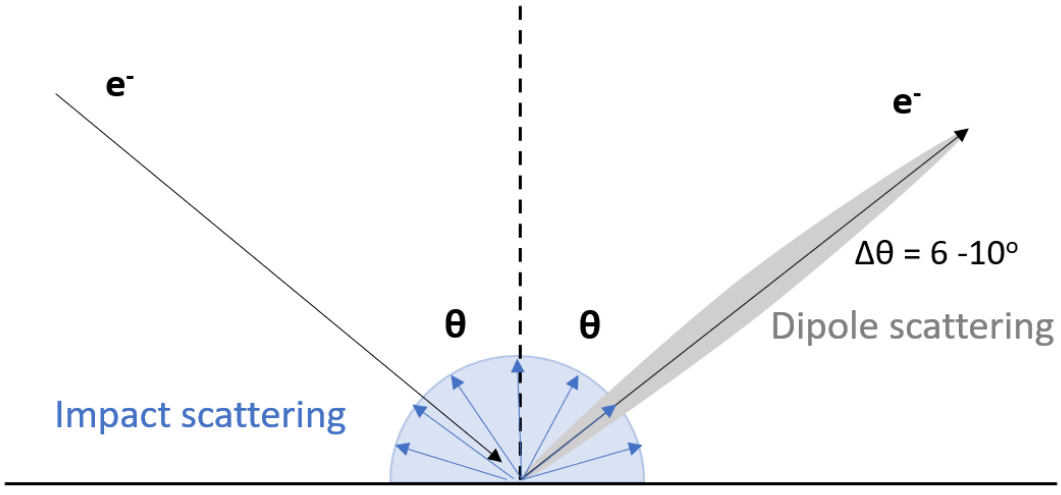

Figure 2.7 Illustration of dipole and impact scatterings of incident electrons during HREELS measurements.

Figure 2.7 shows the different types of electron scatterings that happen during an HREELS measurement. In a typical process, low energy electrons are guided through two monochromators before they reach the sample surface. After hitting the surface, electrons are scattered and collected

by the detector. The energy loss of the electrons corresponds to the energy required to excite the vibrational modes of chemical bonds in the adsorbate and therefore can be used to identify the vibrational modes of the functional groups of the adsorbate. When electrons collide with the surface, there are two types of scattering mechanisms: dipole scattering and impact scattering. Dipole scattering produces electron beams that are relatively focused, with a $\Delta\theta$ between 6^o and 10^o, where θ is the angle between the incident electron beam and surface normal. But such scattering mechanism only allows the detection of dipole moments that have a perpendicular component to the surface. In contrast, electrons resulting from impact scattering are much more diffused and scatter in all directions. Although lower in signal-noise ratio, impact-scattered electrons can be used to detect vibrational modes either parallel or perpendicular to the surface. During on-specular HREELS measurements (*i.e.*, the angle incidence equals the angle of scattering), both dipole and impact scatterings will be detected. If one needs to determine the orientation of specific vibrational mode, one can tilt the surface slightly to conduct off-specular measurements where electrons resulting from dipole scattering cannot enter the detector. As a result, the peaks associated with vibrational modes more perpendicular to the surface will decrease significantly, while those more parallel to the surface will remain relatively unchanged. Therefore, HREELS can be used to measure dipole moments that have either parallel to perpendicular components to the surface. In addition, due to the use of electrons, HREELS is highly surface-sensitive, which makes HREELS an ideal technique for studying vibrational modes on the surface.

2.4 Theoretical Methods

2.4.1 Density Functional Theory

Density Functional Theory (DFT) uses electron density approximation to simplify the Schrodinger Equation to significantly reduce computation expense for calculating catalytic

systems of interest. Using the DFT method, many useful information for catalysis can be computed, such as binding energies, activation energies, binding configurations, vibrational frequencies, and density of states. Such information often provides insights into reaction mechanisms that are difficult to reveal otherwise. This section provides a brief overview of the DFT method, which has been summarized in greater detail by Chen *et al.*.[1]

Equation 2.7 below is the Schrodinger Equation that describes the wave-like properties of matters that DFT is based on.

$$\widehat{H}\,\Psi = \varepsilon\,\Psi \tag{2.7}$$

The Hamiltonian describes the state of the system resulting from all the interactions. The eigenfunction, wave function, describes the characteristic states of the system. The eigenvalues represent the energy of the system. Solving this equation numerically is computationally very expensive and therefore not feasible for most catalytic systems. The Hamiltonian consists of three terms as shown in Equation 2.8. The first term accounts for the kinetic energy of the electrons, the second term describes the electron-nucleus interaction, and the third term describes the electron-electron interaction. While the first two terms are relatively easy to calculate, computing the third term is very expensive.

$$\widehat{H} = -\frac{1}{2}\sum_{i=1}^{n}\nabla_i^2 - \sum_{\mu=1}^{N}\sum_{i=1}^{n}\frac{z_\mu}{r_{\mu i}} + \sum_{i=1}^{n-1}\sum_{j=i+1}^{n}\frac{1}{r_{\mu i}} \tag{2.8}$$

In order to simplify this equation so that it is computationally feasible, the DFT method solves for electron density instead of individual electrons and effectively reduces the many-body problem into a single-body problem based on the Hohenberg–Kohn theorem, as shown in the Kohn-Sham equation (Equation 2.9). The first term represents the kinetic energy. The second term is the effective potential (Equation 2.10), which consists of the nucleus-electron interaction, electron-electron Coulomb interaction, and a third term called exchange correlation potential that

accounts for the rest of the interactions. Given the exact exchange correlation potential, the exact electron density can be calculated. Two main exchange correlations used in DFT calculations are the local density approximation (LDA) and the general gradient approximation (GGA). LDA assumes that the electron density to be a uniform electron cloud, whereas GGA accounts for the first-order gradient of electron density and is more accurate. Commonly used GGA functionals include the PW91, PBE, and RPBE functionals.[1]

$$\left(-\frac{1}{2}\nabla^2 + v_{eff}(r) - \varepsilon_j\right)\varphi(r) = 0 \tag{2.9}$$

$$v_{eff}(r) = v(r) + \int \frac{\rho(r')}{|r-r'|}dr' + v_{xc} \tag{2.10}$$

After selecting the proper exchange correlation, the total energy of the system can be iteratively computed in the following manner. Equation 2.11 is first used to calculate an initial guess of electron density, which is then used in Equation 2.10 to solve for the effective potential that is substituted into Equation 2.9 to solve for the Kohn-Sham orbitals. The KS orbitals are then used to calculate the electron density using Equation 2.11. until the electron density is self-consistent within a specified tolerance.

$$\rho(r) = \sum_{i=1}^{n}|\varphi_i(r)|^2 \tag{2.11}$$

The electron density can then be used to calculate the total energy of the system using Equation 2.12, where the first term represents the kinetic energy for non-interacting systems, the second term is due to Coulomb electron-electron interaction, the third term accounts for the electron-nucleus interaction, and the fourth term represents the exchange correlation.

$$E[\rho] = -\frac{1}{2}\sum_{i=1}^{n}\langle\varphi_i|\nabla^2|\varphi_i\rangle + \frac{1}{2}\int\int \frac{\rho(r)\rho(r')}{|r-r'|}dr\,dr' - \int v(r)\rho(r)dr + E_{xc}(\rho) \tag{2.12}$$

In order to further simplify the calculations and reduce the computational expense, pseudopotentials and periodic boundary conditions are used in slab DFT calculations. The use of pseudopotential is based on the assumption that core electrons do not participate in chemical reactions, and therefore an effective potential can be used to replace the core electrons. The periodic boundary condition is based on Bloch's theorem by using the product of a planewave and a periodic function to represent the wave function of an electron, as shown in Equation 2.13. The periodic function can be further expanded into Equation 2.14, in which the G terms accounts for the wave vectors of the reciprocal lattice vectors. Ideally, an infinite number of planewaves are needed to achieve a perfect expansion. Nonetheless, due to the finite energy of the wave function, the planewave basis set must be cut at certain energies. In order to achieve desired precision, the cutoff energy for each element has to be tested individually.

$$\psi_{nk}(r) = e^{ik\cdot r} u_{nk}(\mathrm{r}) \tag{2.13}$$

$$u_{nk}(r) = \sum_{G} C_{\mathrm{n},k} + G e^{iG\cdot r} \tag{2.14}$$

2.5 References

(1) Chen, J. G.; Menning, C. A.; Zellner, M. B. Monolayer Bimetallic Surfaces: Experimental and Theoretical Studies of Trends in Electronic and Chemical Properties. *Surf. Sci. Rep.* **2008**, *63* (5), 201–254. https://doi.org/10.1016/j.surfrep.2008.02.001.

(2) Cumpson, P. J.; Seah, M. P. Elastic Scattering Corrections in AES and XPS . II . Estimating Attenuation Lengths and Conditions Required for Their Valid Use in Overlayer/Substrate Experiments. *Surf. Interface Anal.* **1997**, *25* (6), 430–446. https://doi.org/10.1002/(SICI)1096-9918(199706)25:6<430::AID-SIA254>3.0.CO;2-7.

(3) Masel, R. I. *Principles of Adsorption and Reaction on Solid Surfaces*; Wiley: New York, 1996.

(4) Redhead, P. a. Thermal Desorption of Gases. *Vacuum* **1962**, *12* (4), 203–211. https://doi.org/10.1016/0042-207X(62)90978-8.

(5) Soriaga, M. P.; Chen, X.; Li, D. High Resolution Electron Energy-Loss Spectroscopy. In *Applications of physical methods to inorganic and bioinorganic chemistry*; Wiley: Hoboken, NJ, 2007.

Chapter 3: Cobalt-Modified Molybdenum Carbide as a Selective Catalyst for Hydrodeoxygenation of Furfural

3.1 Introduction

The catalytic upgrading of biomass into chemicals and fuels is a promising method to address the current energy and environmental challenges.[1-5] Many biomass-derived molecules contain excess oxygen, which leads to low energy density and undesired reactivity to produce byproducts[6] when used directly in the fuel and chemical sectors. In order to convert these molecules into more valuable products, the excess oxygen needs to be selectively removed via the hydrodeoxygenation (HDO) reaction without carbon-carbon bond scission. Among the biomass derivatives, furfural is a promising platform chemical that can be produced from the dehydration of xylose, a derivative from hemicellulose.[7] Furfural is an example of the over-functionalized molecules that can be upgraded efficiently with the HDO reaction.

In this work, we focused on the conversion of furfural into 2-methylfuran (2-MF), which is a promising fuel additive due to its high blending research octane number.[7] In the conversion from furfural to 2-MF, C=O bond cleavage of the external carbonyl group is required via the HDO reaction. To selectively break the C=O bond, a catalyst should bind to oxygen strongly enough to cleave the C=O bond to produce 2-MF and atomic oxygen, but weakly enough so that the oxygen atom can be easily removed to complete the catalytic cycle. Thus, the oxygen binding energy of the catalyst should play an important role in controlling the catalytic activity and stability. Previously, copper-based catalysts have been reported to be active for the furfural HDO reaction.[8] However, these reactions used copper chromite, which is toxic and not environmentally friendly. More recently, bimetallic catalysts $FeNi/SiO_2$ and bimetallic surfaces Fe/Ni(111) and Co/Pt(111)

were reported to selectively convert furfural to 2-MF.[9-11] Bimetallic catalysts typically possess different d-band characteristics and thus different binding energies from their parent metals. This unique property allows the tuning of the activity and selectivity of the monometallic catalysts with admetals.[12] However, this unique property is structurally dependent. For example, it was reported that the structure of a Co-overlayer deposited on Pt(111) showed higher 2-MF activity than the Pt/Co/Pt(111) subsurface structure.[11] At elevated temperatures, the Co-overlayer on Pt can easily diffuse into the subsurface, decreasing the HDO activity for 2-MF production.

On the other hand, molybdenum carbide (Mo_2C) possesses similar bulk electronic properties to Pt[13] and can also serve as a diffusion barrier to prevent the metal overlayer from diffusing into the subsurface,[14] making it a good substrate to maintain the metal overlayer structure. By replacing the Pt substrate with Mo_2C, the cost of the catalyst can also be significantly reduced. In addition, Mo_2C is a selective catalyst for the C=O bond scission. For example, Mo_2C has been shown as a highly selective catalyst for the HDO reaction of C3 molecules, such as propanol and propanal, to produce propylene.[15] Mo_2C was also reported to selectively convert furfural to 2-MF but deactivated quickly.[16] The cause of the deactivation was considered to be poisoned by the strong bonding of atomic oxygen[17] and the polymeric derivatives of furfural[16] by blocking the active sites on Mo_2C.

It has been reported that admetals can be used to modify the binding energies of carbon, oxygen and hydrogen on Mo_2C.[18] This property can potentially be used to reduce the furfural and oxygen binding energies on Mo_2C to enhance the stability of the catalyst. In order to solve the stability issues associated with the bimetallic and Mo_2C catalysts, this work combines the advantages of both types of catalysts and uses Co overlayer to modify Mo_2C. In this way, the Co overlayer reduces the oxygen and furfural binding energies on Mo_2C to prevent the poison by these

adsorbates to increase the catalyst stability, and the Mo_2C substrate serves as a diffusion barrier to stabilize the Co overlayer structure. Density functional theory (DFT) was used to calculate the binding energies and bond lengths of furfural on Mo_2C(0001) and Co/Mo_2C/Mo(0001). The gas-phase products were determined using temperature-programmed desorption (TPD) and the surface intermediates and adsorption configurations were identified using high-resolution electron energy loss spectroscopy (HREELS) under ultra-high vacuum (UHV) conditions. Parallel flow reactor experiments were performed to verify the stability trend between Mo_2C and Co/Mo_2C powder catalysts at ambient pressure.

3.2 Experimental and Theoretical Methods

3.2.1 DFT Calculations

All DFT calculations were preformed using the Vienna *Ab initio* Simulation Package (VASP) [19-21] with the Projector Augmented Wave (PAW) method.[22] Generalized Gradient Approximation (GGA)[23] and the PW91 functional[24] were used with a kinetic cutoff energy of 400 eV. The total energies were minimized self-consistently using a convergence threshold of 10^{-6} eV. The nuclear degrees of freedom were optimized to a force convergence threshold of 0.05 eV $Å^{-1}$. A periodic 4x4 unit cell and a 3 x 3 x 1 Monkhorst–Pack k-point grid were used for all slabs. The lattice constants of Mo-terminated Mo_2C (0001) was previously reported.[25] The Mo_2C(0001) surface was modeled by adding 20 Å of vacuum onto a slab containing six alternate layers of Mo and C, with a ratio of Mo/C=2. The Co-modified Mo_2C(0001) surface was modeled by adding an atomic layer of Co over the Mo_2C surface. The metal overlayer and the top Mo_2C layer were allowed to relax. The calculations were carried out with the implementation of spin-polarization. The binding energy of the adsorbate on each surface was calculated by subtracting the free energies of the slab and gas-phase adsorbate from that of the slab with adsorbate.

3.2.2 Surface Science Experiments

The TPD experiments were carried out in an ultra-high vacuum (UHV) chamber with a base pressure of $5x10^{-10}$ Torr. The chamber is equipped with an Auger electron spectrometer (AES), a mass spectrometer (MS), a sputter gun and metal sources as previously described.[26] A Mo(110) single crystal was spot-welded to two tantalum posts for resistive heating. A K-type thermocouple was spot-welded to the back of the crystal for temperature measurements. The HREELS experiments were performed in a separate UHV chamber equipped with similar instruments as the TPD chamber in addition to the HREELS spectrometer, as reported previously.[27] Samples were prepared in the upper chamber and subsequently lowered to the HREELS chamber for measurements.

The procedure for preparing carbide-modified Mo(110) has been previously reported.[28] In a typical experiment, the Mo(110) crystal was cleaned using Ne^+ sputtering at 1000 K, followed by annealing to 1200 K. Trace amount of carbon on the surface was titrated with oxygen at 1000 K and subsequently annealed to 1200 K. Carbide-modified Mo(110) surface, as a model surface for Mo_2C, was synthesized using cycles of ethylene dosing at 600 K and annealing to 1200 K until a Mo/C atomic ratio of 2:1 was reached. Based on previous literature, the as-synthesized surface should be Mo-terminated with a p(4×4) LEED pattern.[29,30] The Co overlayer was deposited onto the Mo_2C/Mo(110) surface using a metal evaporation source. 5L of hydrogen, corresponding to half of the saturation coverage of atomic hydrogen, followed by 4L of furfural were introduced into the chamber through a stainless-steel dosing line. For TPD experiments, the surfaces were ramped at 3K/s and the desorbed gases were detected by the MS. For HREELS experiments, the samples were flashed to the desired temperatures at 3K/s and then cooled down to 100K before the spectra were recorded.

Furfural (Sigma Aldrich, 99%) was transferred into a stainless-steel cylinder under N_2 atmosphere and subsequently purified using freeze-pump-thaw cycles. Ethylene, hydrogen, oxygen, neon and carbon monoxide gases were of research purity and were used without further purification.

3.2.3 Synthesis and Characterization of Powder Mo_2C and Co/Mo_2C Catalysts

Ammonium molybdate tetrahydrate (99.98%, Sigma) was grinded and calcined in a muffle oven with a ramp rate of 10K/min to 773K to synthesize MoO_3. To carburize MoO_3, 40mg of the as-synthesized MoO_3 was heated in a quartz tube reactor using a mixture of H_2 and CH_4 (45mL/min; 90/10 v/v) at a ramp rate of 5K/min to 573K and held for 2 hours. The sample was then ramped to 973K at 0.5K/min and held at 973K for 2 hours. Then the sample was cooled to 750K and held for 1 hour and the gas was switched to 40mL/min H_2 to reduce the carburized β-Mo_2C sample.

Co/MoO_3 was synthesized first by dropwise adding an appropriate amount of cobalt (II) nitrate hexahydrate solution to the ammonium molybdate tetrahydrate solution under stirring. The precipitate formed was dried at 393K for 3 hours and calcined in a muffle oven to 773K at a ramp rate of 10K/min. 40mg of the as-synthesized Co/MoO_3 was carburized and reduced using the same procedure as that for MoO_3.

XRD patterns of the powder catalysts were obtained using a Rigaku Ultima X-Ray Diffractometer equipped with a Ni filtered Cu Kα radiation source operated at 40 kV and 44mA. Each sample was scanned at a step size of 0.01^o at a rate of 6^o/min between 20^o and 80^o.

3.2.4 Reactor Experiments

The vapor phase reaction of furfural over powder catalysts was carried out at atmospheric pressure in a quartz tube reactor housed within a tube furnace (Applied Test System). All flow lines were heated to above 453K to prevent the condensation of effluent. After the reduction of the Mo_2C and Co/Mo_2C catalysts at 750K, the temperature was lowered to the reaction temperature of 523K, at which point the gases were switched to 20 mL/min H_2. After obtaining a stable baseline, furfural vapor at a space velocity of 0.10 mL/(g_{cat}*s) was introduced into the quartz tube reactor by directing the H_2 through a bubbler containing furfural preheated to 323K. The molar ratio of hydrogen to furfural was 80. The gas effluent from the reactor was measured by a residual gas analyzer (Stanford Research System RGA200) equipped with a quadruple mass spectrometer.

3.3 Results and Discussion

3.3.1 DFT Calculations

DFT calculations were performed to investigate the adsorption configurations of furfural on $Mo_2C(0001)$ and $Co/Mo_2C(0001)$. The atomic assignment is shown in Scheme 1 and the side views of adsorbed furfural are shown in Figure 3.1. Table 3.1 summaries the C1-C2 and C1-O1 bond lengths and the binding energies of furfural on the two surfaces. Compared to gas phase furfural, the C1-O1 bonds of adsorbed furfural on the $Co/Mo_2C(0001)$ and $Mo_2C(0001)$ surfaces are both elongated, consistent with a η_2(C,O) bonding configuration via the carbonyl group. The elongated C1-O1 bonds should facilitate the C1-O1 bond scission and the subsequent 2-MF formation on both surfaces. In addition, the C1-C2 bonds are shortened on both surfaces, indicating that the C-C scission pathway to form furan is not preferred.

As summarized in Table 3.1, the oxygen and furfural binding energies are both stronger on $Mo_2C(0001)$ than on $Co/Mo_2C(0001)$. This difference suggests that the surface oxygen and furfural can be more easily removed from $Co/Mo_2C(0001)$ during the reaction, leaving the active sites open for the subsequent reaction. Under UHV conditions, surface oxygen is likely to recombine with surface carbon and desorb in the form of CO; under reactor condition at ambient pressure with excess hydrogen, surface oxygen can be removed in the form of water. Since furfural likely undergoes polymerization,[16] a lower furfural binding energy should facilitate the desorption of furfural to avoid the poisoning by furfural and related polymeric species.

In addition, since it is not likely for the Co coverage of the powder catalysts to be exactly 1ML, the Co-Mo interface and multilayer Co on Mo_2C surfaces were briefly investigated. Calculations on the Co-Mo interface suggests that furfural adsorbs in an unstable geometry and the furfural binding energy on the Co site is much lower than that on the Mo sites, which could potentially result in a lower 2-MF activity on this interface. On the other hand, the similar furfural binding energies on surfaces with Co coverage beyond 1ML should suggest similar 2-MF activities on these surfaces.

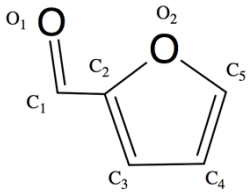

Scheme 3.1 Atomic assignment of the furfural molecule.

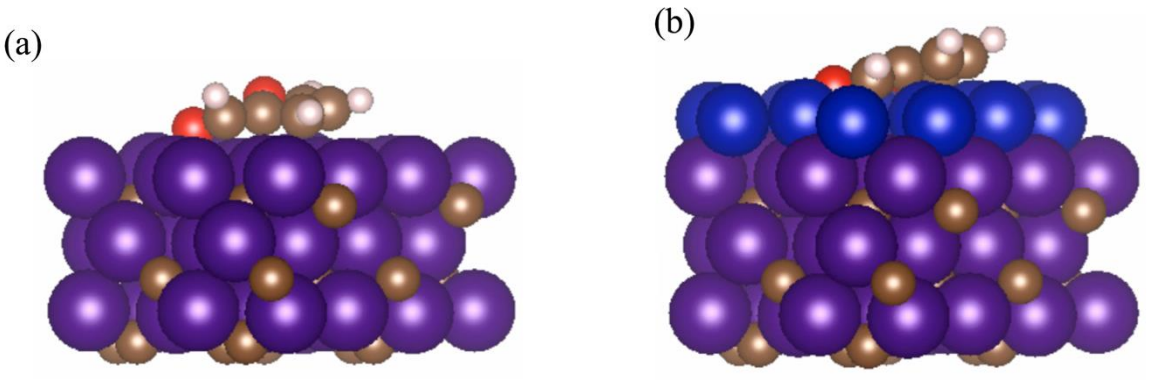

Figure 3.1 Side views of furfural absorbed on (a) $Mo_2C(0001)$ and (b) $Co/Mo_2C(0001)$.

Table 3.1 Comparison of the bond lengths (Å) and binding energies (eV) of furfural on $Mo_2C(0001)$, $Co/Mo_2C(0001)$

	C_1-O_1(Å)	C_1-C_2(Å)	$\frac{d(C_1-O_1)}{d(C_1-C_2)}$	Furfural binding Energy (eV)	Oxygen binding energy (eV)
Gas phase	1.232	1.452	0.848		
$Mo_2C(0001)$	1.36	1.422	0.956	-3.62	-9.467
$Co/Mo_2C(0001)$	1.349	1.416	0.953	-2.087	-7.963

3.3.2 TPD Results on Model Surfaces

TPD experiments were performed on $Mo_2C/Mo(110)$ and $Co/Mo_2C/Mo(110)$ surfaces to determine the gas-phase products from the reactions and the stability of the surfaces. Figure 3.2 (a)-(b) show the TPD spectra of 2-MF desorbed from $Mo_2C/Mo(110)$ and monolayer (1ML) $Co/Mo_2C/Mo(110)$ in three successive experiments without cleaning the surface after each TPD measurement. As shown in Figure 3.2 (a), for the first TPD experiment, a relatively large amount of 2-MF desorbs from Mo_2C at 263K. However, for the second and third TPD experiments, the yield of 2-MF decreases significantly. In contrast, Figure 3.2 (b) shows that a nearly constant

amount of 2-MF desorbs at 301K from Co/Mo_2C/Mo(110) in the three successive TPD experiments.

Comparing the results from the first TPD experiments, the 2-MF yield of Mo_2C/Mo(110) is higher than that of Co/Mo_2C/Mo(110), which is consistent with the trend of oxygen binding energies shown in Table 3.1. The high oxygen binding energy of Mo_2C/Mo(110) promotes the C=O bond cleavage and improves the HDO activity, but also obstructs the removal of the surface oxygen. Comparing the stability for 2-MF production between the two surfaces, Mo_2C/Mo(110) deactivates rapidly after the first TPD experiment, while Co/Mo_2C/Mo(110) maintains comparable activity in subsequent TPD experiments. Figure 3.2(c) shows the CO desorption in the first TPD experiments of both surfaces. No CO desorbs from Mo_2C/Mo(110), while there are two CO desorption peaks from Co/Mo_2C/Mo(110) resulting from the removal of surface oxygen by reacting with carbon. These results suggest that Mo_2C/Mo(110) binds to oxygen too strongly such that the atomic oxygen remain on the surface, blocking the active sites and poisoning the catalytic surface. But the lower oxygen binding energy of Co/Mo_2C/Mo(110) facilitates the facile removal of surface oxygen during the reaction, leaving the active sites available for the next reaction.

Quantification of the gas-phase products is achieved using a previously reported procedure.[31] The results (Table 3.2) indicate that 2-MF and furan are the two furanic compounds observed. The reaction pathways for 2-MF and furan formation are shown in Scheme 3.2. The selectivity to 2-MF is 88% for Mo_2C/Mo(110) and 72% for Co/Mo_2C/Mo(110). Similar to the 2-MF production, the furan production on Mo_2C/Mo(110) decreases rapidly after the first TPD experiment. This again suggests that the surface deactivated after the first TPD experiment. Meanwhile, on Co/Mo_2C/Mo(110) the activities for 2-MF and furan production remain relatively

constant for the three successive TPD experiments, indicating that the stability of Co/Mo_2C/Mo(110) is better than that of Mo_2C/Mo(110).

Investigation of the effect of cobalt coverage on the 2-MF activity suggests that the Mo-Co interface is slightly less active towards 2-MF production compared to the Mo_2C/Mo(110) and 1ML Co/Mo_2C/Mo(110) surfaces, while surfaces with Co coverage greater than 1ML show similar 2-MF activities, consistent with the DFT calculations. The results on the stabilities of Mo_2C/Mo(110), 0.25ML, 1ML and 2ML Co/Mo_2C/Mo(110) show that the presence of Co enhances the stability of not only 1ML Co/Mo_2C, but also partially covered or multilayer Co/Mo_2C surfaces.

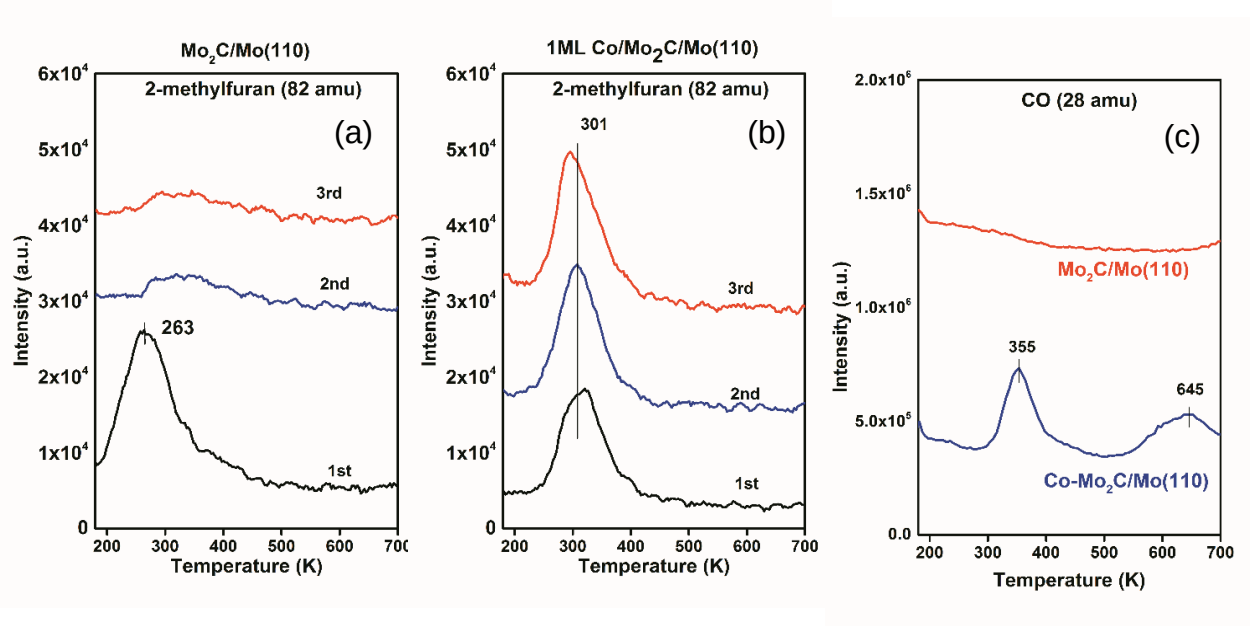

Figure 3.2 Spectra of 2-MF (82 amu) with an exposure of 4L furfural on hydrogen pre-dosed (a) Mo_2C/Mo(110) and (b) monolayer (1ML) Co/Mo_2C/Mo(110) surfaces from three successive experiments; (c): Spectra of CO (28 amu) with an exposure of 4L furfural on corresponding hydrogen pre-dosed surfaces.

Table 3.2 Activities (molecules per metal atom) for the production of furanic compounds on hydrogen pre-dosed surfaces from TPD experiments

	2-MF	Furan	Total activity of furanic compound
Mo_2C/Mo(110) 1st	0.0249	0.0043	0.0292
Mo_2C/Mo(110) 2nd	0.0041	0.0000	0.0041
Mo_2C/Mo(110) 3rd	0.0037	0.0000	0.0037
1ML Co/Mo_2C/Mo(110) 1st	0.0144	0.0040	0.0185
1ML Co/Mo_2C/Mo(110) 2nd	0.0149	0.0041	0.0189
1ML Co/Mo_2C/Mo(110) 3rd	0.0152	0.0058	0.0210

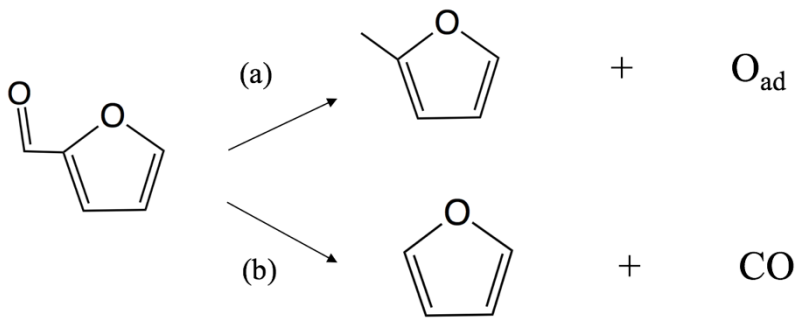

Scheme 3.2 Possible reaction pathways of furfural on Mo_2C/Mo(110) and Co/Mo_2C/Mo(110):

(a) 2-MF formation; (b) furan formation.

3.3.3 HREELS Measurements

HREELS experiments were performed to identify the adsorption configurations of furfural and reaction intermediates on the Mo_2C/Mo(110) and Co/Mo_2C/Mo(110) surfaces. The assignments for the vibrational modes of furfural molecule are shown in Table 3.3. Figure 3.3 (a) compares the spectra of furfural on Mo_2C/Mo(110) at different temperatures. The spectrum of molecularly absorbed furfural at 100K generally matches the Raman spectrum of liquid-phase furfural.[32] The vibrational peaks at 1060 cm^{-1} (ν_{ring}(C-O)), 1436 cm^{-1} (ν_{ring}(C=C)), 1624 cm^{-1}

($\nu_{aliphatic}$(C=O)) and 3067 cm^{-1} (ν_{ring}(C-H)) are characteristic of furfural. After increasing the temperature to 200 and 250K, the relative intensity of the peak at 1624 cm^{-1}($\nu_{aliphatic}$(C=O)) decreases, suggesting that the C=O bond in the carbonyl group is weakened. This is consistent with the DFT calculation that furfural binds to the surface in a η_2(C,O) bonding configuration via the carbonyl group. The intensity of the peak at 2854 cm^{-1} ($\nu_{aliphatic}$(C-H)) increases as the temperature increases, likely due to the hydrogenation of the carbonyl group. This is consistent with previous literature[33] that the hydrogenation of the carbonyl group is a critical step to the formation of 2-MF.

Figure 3.3 (b) compares the HREEL spectra of molecularly adsorbed 2-MF on Mo_2C and the surface intermediates at 200K on Mo_2C/Mo(110) and Co/Mo_2C/Mo(110) after dosing furfural and hydrogen on the surfaces. The spectra of furfural on Mo_2C/Mo(110) and Co/Mo_2C/Mo(110) show the characteristic vibrational modes of molecularly adsorbed 2-MF, indicating the formation of intermediates similar to 2-MF on both surfaces. This is consistent with the 2-MF onset desorption temperatures of 200K (Mo_2C/Mo(110)) and 235K (Co/Mo_2C/Mo(110)) in the TPD experiments as shown in Figure 3.2 (a) and (b). The similarity between the surface intermediates on Mo_2C/Mo(110) and Co/Mo_2C/Mo(110) are consistent with the similar HDO activities shown in the TPD results.

Table 3.3 Vibrational mode assignment for furfural molecule

Mode	Frequency (cm^{-1})		
	Raman[30]	H/Ni(111)[10]	H/Mo_2C/Mo(110)[a]
ω_{ring}(C-H)		771	765
ν_{ring}(C-O)	1025		1060
ν_{ring}(C=C)	1446	1448	1436
$\nu_{aliphatic}$(C=O)	1684	1637	1624
$\nu_{aliphatic}$(C-H)		2882	2852
ν_{ring}(C-H)	3153	3112	3067

Abbreviation: ω – wagging, ν – stretching

a. 4L furfural on hydrogen pre-dosed Mo_2C/Mo(110) at 100K

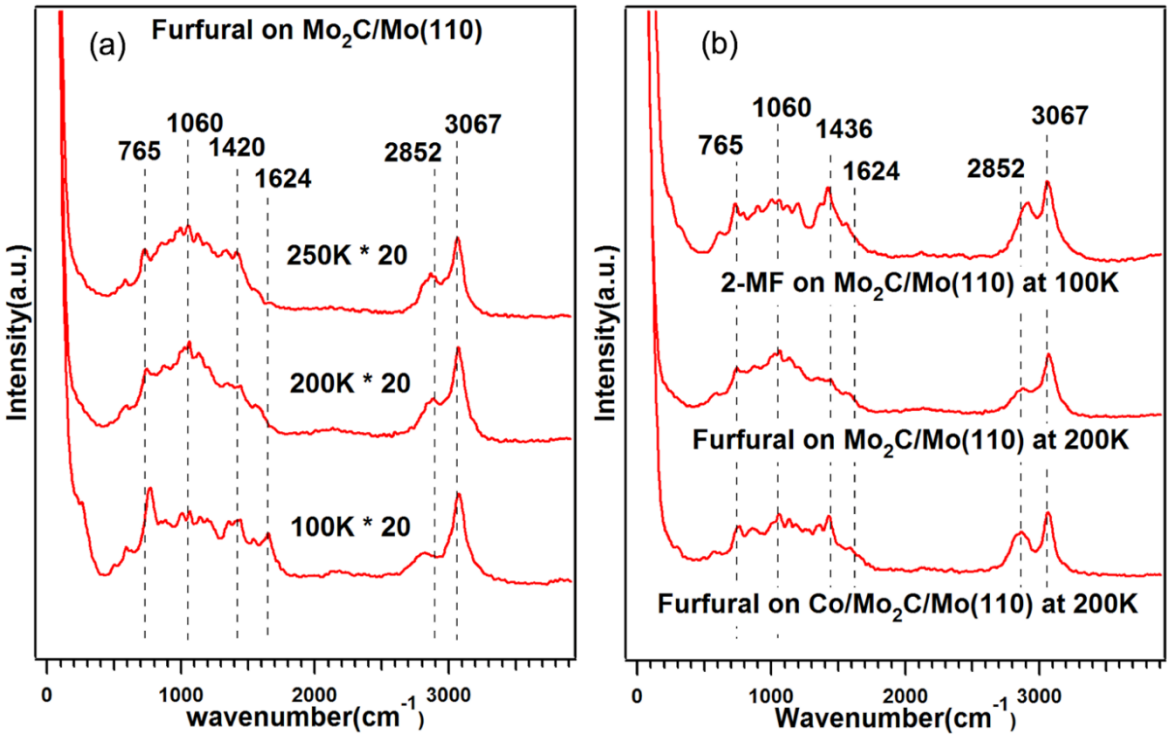

Figure 3.3 HREEL spectra of (a) Furfural on Mo_2C/Mo(110) at different temperatures and (b) 4L 2-MF on Mo_2C/Mo(110) at 100K and 4L furfural on hydrogen pre-dosed Mo_2C/Mo(110) and Co/Mo_2C/Mo(110) surfaces at 200K.

3.3.4 Reactor Evaluation of Powder Catalysts: Bridging the Pressure and Materials Gaps

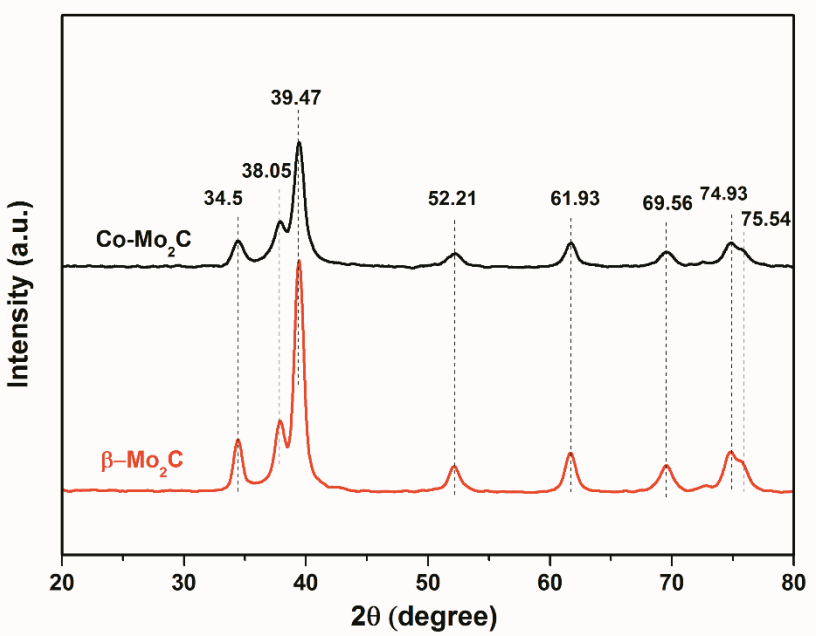

Figure 3.4 XRD patterns of spent β-Mo_2C and 2 wt% Co/Mo_2C catalysts.

Since DFT and TPD results suggested that Co/Mo_2C/Mo(110) should be more stable than Mo_2C/Mo(110) for the HDO reaction of furfural, porous Mo_2C and Co/Mo_2C catalysts were synthesized and a vapor phase flow reactor was used to evaluate the stability of the catalysts. XRD analysis on the spent Mo_2C and Co/Mo_2C catalysts was performed to verify the formation of Mo_2C. As shown in Figure 3.4, the 2θ of 34.5°, 38.05°, 39.47°, 52.21°, 61.93°, 69.56°, 74.93° and 75.54° correspond to the (100), (002), (101), (102), (110), (103), (112) and (201) facets of β-Mo_2C (Joint Committee on Powder Diffraction Standards, no. 35-0787). With the addition of Co, the pattern does not change, likely due to the low loading of Co. In addition, since Mo_2C is a metal diffusion barrier, Co should remain on the surface of the Mo_2C particles.

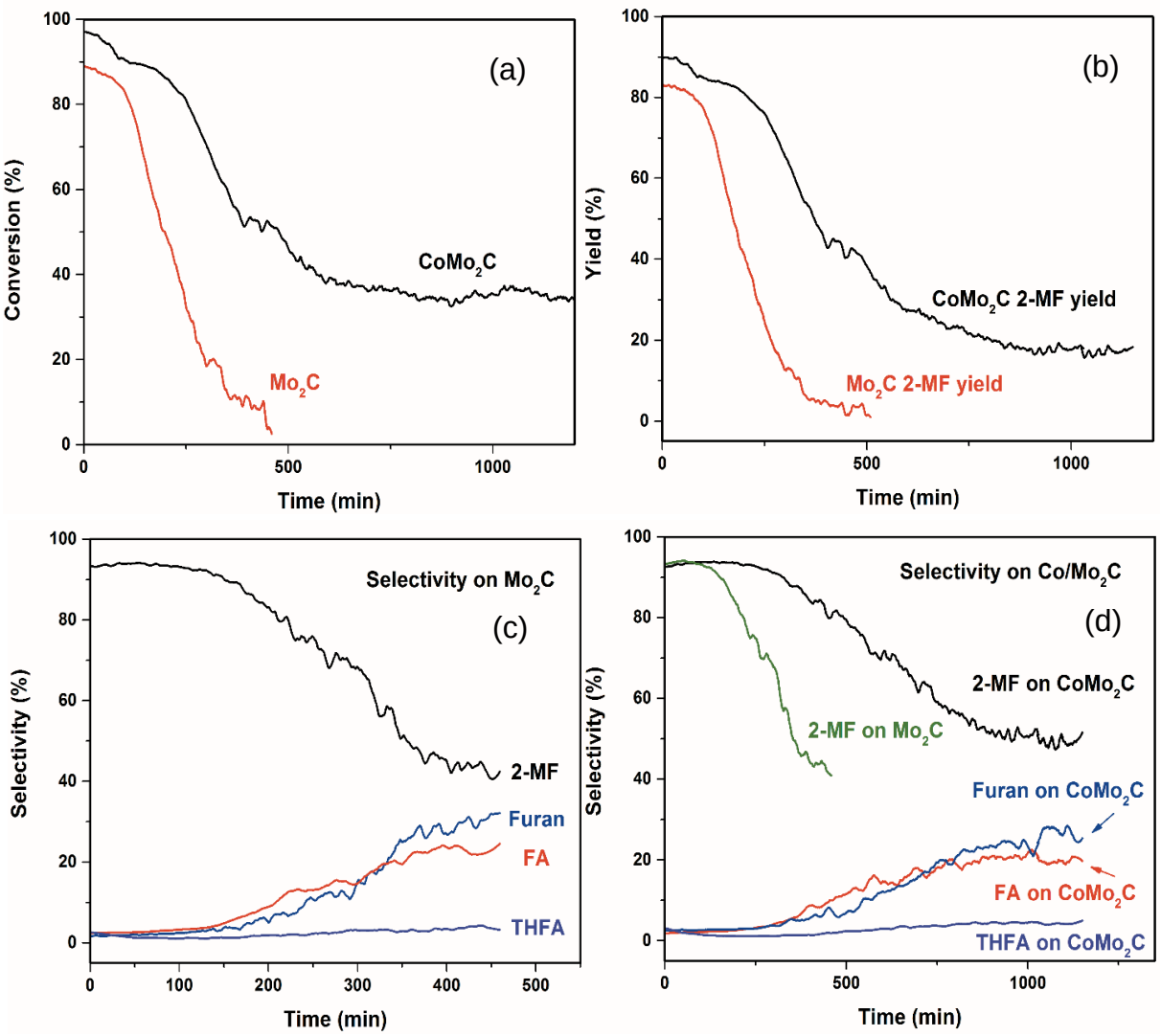

Figure 3.5 Comparison of (a) furfural conversion, (b) 2-MF yield and (c)(d) products selectivity on Mo_2C and Co/Mo_2C. The selectivity to 2-MF on the Mo_2C catalyst (green) is shown in (d) for comparison. The furfural space velocity was 0.10 mL/(gcat*s) as 20 mL/min of hydrogen flowed through a bubbler containing furfural preheated to 323 K. The molar ratio of hydrogen to furfural was 80.

The conversion of furfural (Figure 3.5(a)) and 2-MF yield (Figure 3.5(b)) show the same trend, with the initial conversions (> 87%) and 2-MF yield (>80%) being high on both Mo_2C and Co/Mo_2C with a subsequent decrease. The steady-state furfural conversion over Co/Mo_2C is

approximately 35%, while that of Mo_2C drops to below 5%, confirming that Co/Mo_2C is more stable than Mo_2C. The initial selectivity to 2-MF is above 90% for both Mo_2C and Co/Mo_2C. Over time, the selectivity to 2-MF decreases, although it remains as a major product over both catalysts. The selectivity to furan and furfuryl alcohol (FA) increases with reaction time over both catalysts, while the selectivity to tetrahydrofurfuryl alcohol (THFA) is always under 6%. It should be pointed out that FA and THFA were not detected in the TPD experiments on model surfaces, likely due to the different hydrogen partial pressure between the UHV and reactor environments. Overall, the flow reactor results are consistent with the trends from DFT calculations and UHV experiments on model surfaces, which show that $Co/Mo_2C/Mo(110)$ and $Mo_2C/Mo(110)$ have similar selectivity to 2-MF, but the stability of $Co/Mo_2C/Mo(110)$ is better than $Mo_2C/Mo(110)$, possibly due to the lower oxygen and furfural binding energies on $Co/Mo_2C/Mo(110)$. The general similarity between the behaviors of $Mo_2C/Mo(110)$ and $Co/Mo_2C/Mo(110)$ model surfaces and their corresponding powder catalysts suggests the feasibility of using surface science approaches to guide the design of efficient HDO catalysts.

3.4 Conclusions

Based on the results and discussion presented above, the following conclusions can be made regarding the potential utilization of Co/Mo_2C as an active and stable HDO catalyst:

(1) DFT calculations predict that the external carbonyl C=O bond in furfural is elongated on both $Mo_2C/Mo(110)$ and $Co\text{-}Mo_2C/Mo(110)$ surfaces due to the strong interaction between the carbonyl group and the surfaces, which should promote the C=O bond scission to form 2-MF. DFT calculations also indicate that the binding energies of oxygen and furfural on $Co/Mo_2C(0001)$ are weaker than on $Mo_2C(0001)$, suggesting that Co/Mo_2C might be more resistant to poisoning from surface oxygen, furfural and associated polymeric species.

(2) TPD results under UHV conditions verify the enhanced stability of Co-Mo_2C/Mo(110) due to the facile removal of oxygen. HREELS results indicate that an intermediate similar to 2-MF is formed on Mo_2C/Mo(110) and Co-Mo_2C/Mo(110), consistent with the desorption of 2-MF in the TPD experiments.

(3) Parallel flow reactor evaluations on powder Mo_2C and Co-Mo_2C catalysts further confirm the DFT predictions and surface science experiments that Co/Mo_2C is more stable than Mo_2C, while the HDO selectivity is similar for both catalysts.

(4) The general similarity between model surfaces and powder catalysts suggests the feasibility of using surface science approaches to identify promising catalyst candidates and using reactor studies to bridge the pressure and materials gaps.

Overall, it can be concluded that oxygen and furfural binding energies play an important role in stabilizing the catalyst for the furfural HDO reaction without affecting the HDO selectivity. This work shows the potential of modifying Mo_2C with metal overlayer to improve the catalyst stability and provides insights into the design of more efficient Mo_2C-based HDO catalysts for upgrading biomass-derived oxygenates.

3.5 Acknowledgements

Reprinted from *Lin, Z., Wan, W., Yao, S. & Chen, J. G. Cobalt-modified molybdenum carbide as a selective catalyst for hydrodeoxygenation of furfural. Appl. Catal. B Environ. 233, 160–166 (2018)*, with permission from Elsevier. Copyright © 2018 Elsevier. I acknowledge the assistance from Dr. Binhang Yan for the flow reactor experiments, Dr. Baohuai Zhao for the XRD analysis and Dr. Zhifeng Jiang for the surface science experiments.

3.6 References

(1) Chheda, J. N.; Huber, G. W.; Dumesic, J. A. Liquid-Phase Catalytic Processing of Biomass-Derived Oxygenated Hydrocarbons to Fuels and Chemicals. *Angew. Chemie - Int. Ed.* **2007**, *46* (38), 7164–7183. https://doi.org/10.1002/anie.200604274.

(2) Huber, G. W.; Corma, A. Synergies between Bio- and Oil Refineries for the Production of Fuels from Biomass. *Angew. Chemie - Int. Ed.* **2007**, *46* (38), 7184–7201. https://doi.org/10.1002/anie.200604504.

(3) Wang, H.; Male, J.; Wang, Y. Recent Advances in Hydrotreating of Pyrolysis Bio-Oil and Its Oxygen-Containing Model Compounds. *ACS Catal.* **2013**, *3* (5), 1047–1070. https://doi.org/10.1021/cs400069z.

(4) Huber, G. W.; Iborra, S.; Corma, A. Synthesis of Transportation Fuels from Biomass: Chemistry, Catalysts, and Engineering. *Chem. Rev.* **2006**, *106* (9), 4044–4098. https://doi.org/10.1021/cr068360d.

(5) Wettstein, S. G.; Martin Alonso, D.; Gürbüz, E. I.; Dumesic, J. A. A Roadmap for Conversion of Lignocellulosic Biomass to Chemicals and Fuels. *Curr. Opin. Chem. Eng.* **2012**, *1* (3), 218–224. https://doi.org/10.1016/j.coche.2012.04.002.

(6) Xiong, K.; Yu, W.; Vlachos, D. G.; Chen, J. G. Reaction Pathways of Biomass-Derived Oxygenates over Metals and Carbides: From Model Surfaces to Supported Catalysts. *ChemCatChem* **2015**, *7* (9), 1402–1421. https://doi.org/10.1002/cctc.201403067.

(7) Lange, J. P.; Van Der Heide, E.; Van Buijtenen, J.; Price, R. Furfural-A Promising Platform for Lignocellulosic Biofuels. *ChemSusChem* **2012**, *5* (1), 150–166. https://doi.org/10.1002/cssc.201100648.

(8) Burnett, L. W.; Johns, I. B.; Holdren, R. F.; Hixon, R. M. Production of 2-Methylfuran by Vapor-Phase Hydrogenation of Furfural. *Ind. Eng. Chem.* **1948**, *40* (3), 502–505. https://doi.org/10.1021/ie50459a034.

(9) Sitthisa, S.; An, W.; Resasco, D. E. Selective Conversion of Furfural to Methylfuran over Silica-Supported NiFe Bimetallic Catalysts. *J. Catal.* **2011**, *284* (1), 90–101. https://doi.org/10.1016/j.jcat.2011.09.005.

(10) Yu, W.; Xiong, K.; Ji, N.; Porosoff, M. D.; Chen, J. G. Theoretical and Experimental Studies of the Adsorption Geometry and Reaction Pathways of Furfural over FeNi Bimetallic Model Surfaces and Supported Catalysts. *J. Catal.* **2014**, *317*, 253–262. https://doi.org/10.1016/j.jcat.2014.06.025.

(11) Jiang, Z.; Wan, W.; Lin, Z.; Xie, J.; Chen, J. G. Understanding the Role of M/Pt(111) (M=Fe, Co, Ni, Cu) Bimetallic Surfaces for Selective Hydrodeoxygenation of Furfural. *ACS Catal.* **2017**, *7* (9), 5758–5765. https://doi.org/10.1021/acscatal.7b01682.

(12) Chen, J. G.; Menning, C. A.; Zellner, M. B. Monolayer Bimetallic Surfaces: Experimental and Theoretical Studies of Trends in Electronic and Chemical Properties. *Surf. Sci. Rep.* **2008**, *63* (5), 201–254. https://doi.org/10.1016/j.surfrep.2008.02.001.

(13) Levy, R. B.; Boudart, M. Platinum-Like Behavior of Tungsten Carbide in Surface Catalysis. *Science (80-.).* **1973**, *181* (4099), 547–549. https://doi.org/10.1126/science.181.4099.547.

(14) Tripathi, C. C.; Kumar, M.; Kumar, D. Atom Beam Sputtered Mo2C Films as a Diffusion Barrier for Copper Metallization. *Appl. Surf. Sci.* **2009**, *255* (6), 3518–3522. https://doi.org/10.1016/j.apsusc.2008.09.076.

(15) Ren, H.; Yu, W.; Salciccioli, M.; Chen, Y.; Huang, Y.; Xiong, K.; Vlachos, D. G.; Chen, J. G. Selective Hydrodeoxygenation of Biomass-Derived Oxygenates to Unsaturated Hydrocarbons Using Molybdenum Carbide Catalysts. *ChemSusChem* **2013**, *6* (5), 798–801. https://doi.org/10.1002/cssc.201200991.

(16) Xiong, K.; Lee, W. S.; Bhan, A.; Chen, J. G. Molybdenum Carbide as a Highly Selective Deoxygenation Catalyst for Converting Furfural to 2-Methylfuran. *ChemSusChem* **2014**, *7* (8), 2146–2149. https://doi.org/10.1002/cssc.201402033.

(17) Liu, P.; Rodriguez, J. A. Water-Gas-Shift Reaction on Molybdenum Carbide Surfaces: Essential Role of the Oxycarbide. *J. Phys. Chem. B* **2006**, *110* (39), 19418–19425. https://doi.org/10.1021/jp0621629.

(18) Yu, W.; Salciccioli, M.; Xiong, K.; Barteau, M. A.; Vlachos, D. G.; Chen, J. G. SI-Theoretical and Experimental Studies of C-C versus C-O Bond Scission of Ethylene Glycol Reaction Pathways via Metal-Modified Molybdenum Carbides. *ACS Catal.* **2014**, *4* (5), 1409–1418. https://doi.org/10.1021/cs500124n.

(19) Kresse, G.; Hafner, J. Ab Initio Molecular Dynamics for Liquid Metals. *Phys. Rev. B* **1993**, *47* (1), 558–561. https://doi.org/10.1103/PhysRevB.47.558.

(20) Kresse, G.; Furthmüller, J. Efficiency of Ab-Initio Total Energy Calculations for Metals and Semiconductors Using a Plane-Wave Basis Set. *Comput. Mater. Sci.* **1996**, *6* (1), 15–50. https://doi.org/10.1016/0927-0256(96)00008-0.

(21) Kresse, G.; Furthmuller, J. Efficient Iterative Schemes for Ab Initio Total-Energy Calculations Using a Plane-Wave Basis Set. *Phys. Rev. B* **1996**, *54* (16), 11169–11186.

(22) Kresse, G.; Joubert, D. From Ultrasoft Pseudopotentials to the Projector Augmented-Wave Method. *Phys. Rev. B* **1999**, *59* (3), 1758–1775. https://doi.org/10.1103/PhysRevB.59.1758.

(23) Teter, M. P.; Payne, M. C.; Allan, D. C. Solution of Schrodinger's Equation for Large Systems. *Phys. Rev. B* **1989**, *40* (18), 12255–12263. https://doi.org/10.1103/PhysRevB.40.12255.

(24) Perdew, J.; Chevary, J.; Vosko, S.; Jackson, K.; Pederson, M.; Singh, D.; Fiolhais, C. Atoms, Molecules, Solids, and Surfaces: Applications of the Generalized Gradient Approximation for Exchange and Correlation. *Phys. Rev. B* **1992**, *46* (11), 6671–6687. https://doi.org/10.1103/PhysRevB.48.4978.2.

(25) Kitchin, J. R.; Nørskov, J. K.; Barteau, M. A.; Chen, J. G. Trends in the Chemical Properties of Early Transition Metal Carbide Surfaces: A Density Functional Study. *Catal. Today* **2005**, *105* (1 SPEC. ISS.), 66–73. https://doi.org/10.1016/j.cattod.2005.04.008.

(26) Salciccioli, M.; Yu, W.; Barteau, M. A.; Chen, J. G.; Vlachos, D. G. Differentiation of O-H and C-H Bond Scission Mechanisms of Ethylene Glycol on Pt and Ni/Pt Using Theory and Isotopic Labeling Experiments. *J. Am. Chem. Soc.* **2011**, *133* (20), 7996–8004. https://doi.org/10.1021/ja201801t.

(27) Meng, J.; Menning, C. A.; Zellner, M. B.; Chen, J. G. Surface Science Effects of Bimetallic Modi Fi Cation on the Decomposition of CH 3 OH and H 2 O on Pt / W (110) Bimetallic Surfaces. *Surf. Sci.* **2010**, *604*, 1845–1853. https://doi.org/10.1016/j.susc.2010.07.015.

(28) Hwu, H. H.; Chen, J. G. Reactions of Methanol and Water over Carbide-Modified Mo(110). *Surf. Sci.* **2003**, *536* (1–3), 75–87. https://doi.org/10.1016/S0039-6028(03)00607-1.

(29) Frühberger, B.; Chen, J. G. Reaction of Ethylene with Clean and Carbide-Modified Mo(110): Converting Surface Reactivities of Molybdenum to Pt-Group Metals. *J. Am. Chem. Soc.* **1996**, *118* (46), 11599–11609. https://doi.org/10.1021/ja960656l.

(30) Frühberger, B.; Chen, J. G.; Eng, J. J.; Bent, B. E. Reactivities of Carbon- and Nitrogen-modified Mo(110) A Comparison of Modification Effects by Surface and Interstitial Adatoms. *J. Vac. Sci. Technol. A Vacuum, Surfaces, Film.* **1996**, *14* (3), 1475–1481. https://doi.org/10.1116/1.579972.

(31) Myint, M.; Yan, Y.; Chen, J. G. Reaction Pathways of Propanal and 1-Propanol on Fe/Ni(111) and Cu/Ni(111) Bimetallic Surfaces. *J. Phys. Chem. C.* **2014**, *118*, 11340–11349. https://doi.org/10.1021/jp501208q.

(32) Kim, T.; Assary, R. S.; Curtiss, L. A.; Marshall, L.; Stair, P. C. Vibrational Properties of Levulinic Acid and Furan Derivatives : Raman Spectroscopy and Theoretical Calculations.

J. Raman Spectrosc. **2011**, *42*, 2069–2076. https://doi.org/10.1002/jrs.2951.

(33) Shi, Y.; Yang, Y.; Li, Y. W.; Jiao, H. Mechanisms of Mo_2C(101)-Catalyzed Furfural Selective Hydrodeoxygenation to 2-Methylfuran from Computation. *ACS Catal.* **2016**, *6* (10), 6790–6803. https://doi.org/10.1021/acscatal.6b02000.

Chapter 4: 1,2-Propanediol as a Surrogate Molecule of Glycerol for Mechanistic Studies of Selective Hydrodeoxygenation Reactions over Molybdenum Carbide and Copper-Modified Molybdenum Carbide Surfaces

4.1 Introduction

The production of fuels and chemicals from renewable biomass resources has drawn significant attention in recent years.[1–8] Biodiesel production is a promising approach of utilizing biomass to help reduce the environmental impact from fossil fuels.[9] Biodiesel is produced mainly via the transesterification reaction of triglyceride with methanol, in which glycerol is formed as a by-product.[10] As the biodiesel production grows rapidly, there is a large surplus of glycerol, which is generally considered as a platform molecule that can be upgraded into many value-added chemicals. Glycerol can be converted using enzymatic and chemical methods. The enzymatic transformations of glycerol have shown promise in producing specialty chemicals, such as 2,3-butanediol,[11,12] or intermediates that can be further upgraded by chemical methods, such as 3-hydroxypropanal.[13–15] On the other hand, chemical conversions of glycerol provide added capability for upgrading glycerol via a variety of pathways. Typical chemical conversion pathways for glycerol include selective oxidation,[16,17] etherification,[18,19] acetylation,[20,21] reforming,[22,23] dehydration,[24,25] and selective hydrogenolysis/hydrodeoxygenation.[26,27] Among these approaches, selective hydrodeoxygenation (HDO) is a particularly interesting approach, in which glycerol can be upgraded into various specialty chemicals, such as allyl alcohol, acetol and propanal. It is generally accepted that Cu-based catalysts are very selective in converting glycerol into 1,2-PDO. In this process glycerol is typically first catalyzed by acid sites into the

acetol intermediate, which is then hydrogenated by the surface Cu sites to form 1,2-PDO.[28–35] Under ultra-high vacuum (UHV) conditions, due to low hydrogen partial pressure, the final product of glycerol HDO reaction over Cu sites should likely be acetol instead. Wan *et al.* have demonstrated that the bond-breaking sequences of glycerol can be tuned by controlling the coverage of Cu modifiers on a molybdenum carbide (Mo_2C) surface, in which the oxygen binding energy of the surface plays an important role in determining the final HDO products.[36] Despite the promising results on the Cu/Mo_2C surfaces, the low vapor pressure and high viscosity of glycerol make it particularly difficult to conduct gas-phase mechanistic studies on both model surfaces and the corresponding powder catalysts. The elucidation of reaction mechanism and activation barriers by *ab initio* computation is also expensive due to the structural complexity resulting from the presence of three -OH groups in glycerol. To date, only very few fundamental studies for glycerol have been done on model surfaces using surface science techniques, mainly due to the experimental difficulties in introducing pure glycerol into ultra-high vacuum (UHV) systems.[36,37]

To this end, this work compares the reaction pathways of glycerol, 1,2- and 1,3-PDO, in an attempt to evaluate whether the diols can serve as model compounds for the study of gas-phase glycerol reaction under UHV conditions. 1,2- and 1,3-PDO are chosen because their structures are similar to that of glycerol and that both diols contain one less -OH functional group than glycerol. The higher vapor pressures of these diols ease the difficulty in introducing reactant into the UHV chamber and also make it potentially possible to carry out gas-phase reactor evaluation on the corresponding powder catalysts. Temperature-programmed desorption (TPD) experiments were performed to probe the gas-phase products from the reactions, and high-resolution electron energy loss spectroscopy (HREELS) measurements were conducted to

identify the surface reaction intermediates. The results show that 1,2-PDO and glycerol undergo similar reaction pathways via similar intermediates on the Mo and Cu sites of the Cu/Mo_2C surfaces, suggesting the feasibility of using 1,2-PDO as a surrogate molecule for further mechanistic studies of glycerol.

4.2 Experimental Methods

The TPD experiments were conducted in a UHV chamber described previously.[38,39] Briefly, a Mo(110) single crystal was spot-welded onto two tantalum posts connected to a manipulator. The tantalum posts served as the medium for resistive heating as well as cooling by liquid nitrogen. A type-K thermocouple was spot-welded to the crystal for temperature measurements. The chamber was equipped with an Auger electron spectroscopy (AES), a quadrupole mass spectrometer (QMS), a sputter gun and two metal sources for physical vapor disposition (PVD). Glycerol and the diols were transferred into a glass cylinder and purified using freeze-pump-thaw cycles. The purity of all chemicals were confirmed using the QMS before performing experiments. In a typical TPD experiment, the Mo(110) single crystal was cleaned by Ne^+ sputtering, followed by annealing to 1200K. In order to synthesize Mo_2C/Mo(110), ethylene was dosed to the surface at 600K, followed by annealing to 1200K to achieve a Mo-terminated Mo_2C surface with a p(4x4) LEED pattern. The synthesis cycle was repeated until a surface C/Mo atomic ratio between 0.2 and 0.3 was determined by AES. The Cu modifier was deposited to the as-synthesized Mo_2C/Mo(110) surface at 600K using a PVD metal source. Subsequently, 5 Langmuir (L, 1 L=1*10^{-6} Torr*s) of hydrogen was dosed to the surface, followed by dosing the desired amount of glycerol or diols. Because of the low vapor pressure of glycerol, the glycerol cylinder and the stainless-steel dosing tubes were maintained at above 400K. The surface was then lowered to 110K and ramped to 800K at a rate of 3K/s facing the

QMS for the detection of the desorbed gas-phase products. HREELS experiments were performed in a separate UHV chamber equipped with the same capabilities as the TPD chamber, with the addition of the HREEL spectrometer. In a typical experiment, the surface was prepared using the same procedure as the TPD experiments. The surface was then ramped to the desired temperature and cooled down to 100K before the HREEL spectra were recorded.

4.3 Results and Discussion

Before the discussion of using 1,2-PDO as a surrogate molecule, the promising result adapted from Wan et al.[36] regarding the tunable glycerol C-O bond breaking sequence is illustrated in Figure 4.1. TPD experiments were conducted to probe the reaction pathway of glycerol on Cu-Mo_2C/Mo(110) with different Cu coverages. The sharp peaks at 270K of 39, 57 and 74 amu are attributed to the cracking fragments from the adsorbed glycerol. On Mo_2C/Mo(110), propylene (39amu) is the only product observed with a broad peak that spans from 200K to 600K. As the Cu coverage increases, the intensity of the propylene peak decreases. When the surface is fully covered by Cu (coverage greater than 1ML), no propylene is produced, suggesting that propylene is produced on the uncovered Mo_2C/Mo(110). Also observed was the increase and subsequent decrease of ally alcohol peak (57amu) as Cu coverage increases. This is an indication that that ally alcohol is produced at the Cu-Mo_2C/Mo(110) interface. A Cu coverage that is too low or too high would inhibit the allyl alcohol production. In addition to the propylene and allyl alcohol observed, acetol (74amu) is also produced on the surface. The peak intensity of acetol increases continuously as the Cu coverage increases, suggesting that acetol is produced on Cu rather than on Mo_2C/Mo(110) or the Cu-Mo_2C/Mo(110) interface. These results provide us important insights that the product selectivity on Mo_2C/Mo(110) can be tuned using metal modifiers.

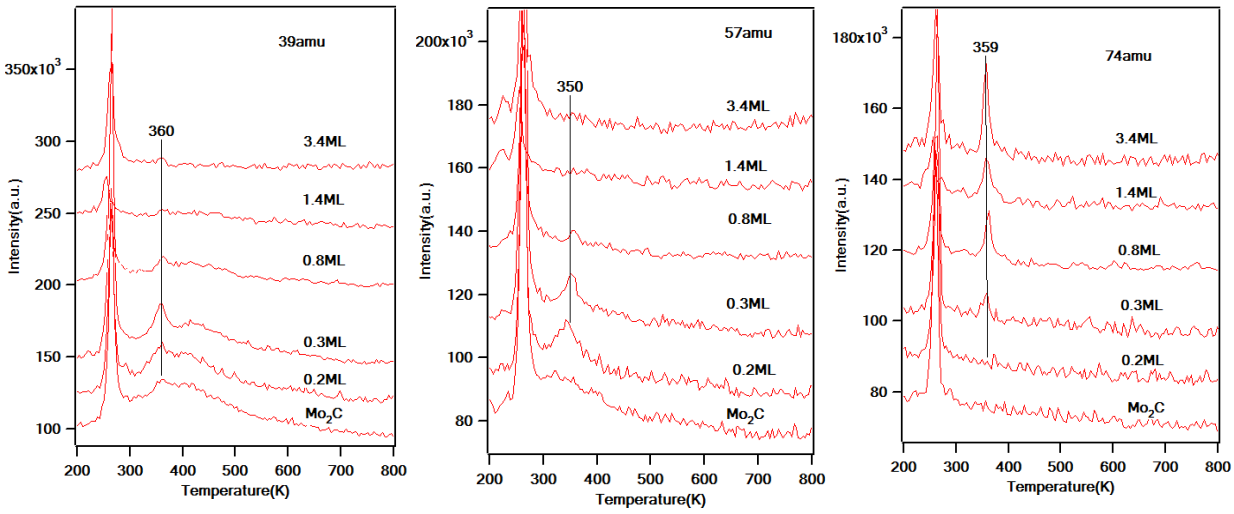

Figure 4.1. TPD spectra of (a) propylene (39amu), (b) allyl alcohol (57amu) and (c) acetol (74amu) after exposure of 4L glycerol on hydrogen pre-dosed Mo_2C/Mo(110) and Cu-Mo_2C/Mo(110) with different Cu coverages.

Figure 4.2 shows the TPD spectra of propylene after dosing glycerol, 1,2- and 1,3-PDO on the Mo_2C and 0.8ML Cu/Mo_2C surfaces. The sharp peaks at 263K, 211K and 229K represent the cracking fragments of desorbed glycerol, 1,2- and 1,3-PDO, respectively. For glycerol and 1,2-PDO on Mo_2C (Figure 4.2(a)), the broad peaks between 250K and 700K are contributed from the desorption of propylene, which is a product from glycerol and 1,2-PDO from the unselective HDO. One should note that for 1,3-PDO, there is also a broad peak between 350K and 700K. This peak is also from the desorption of propylene but has a different peak shape than those of glycerol and 1,2-PDO. Since there the m/z=57 peak is not observed from the reactions of all three molecules on Mo_2C (Figure 4.3), allyl alcohol is not formed and only propylene is produced on Mo_2C. The similar peak shapes and desorption temperatures of propylene from 1,2-PDO and glycerol suggest that these two molecules likely undergo similar C-O bond scission steps to produce propylene. As Cu coverage increases to 0.8ML (Figure 4.2(b)), the propylene

peaks from all three molecules decrease, which is consistent with a previous study[36] that propylene is produced on the Mo site. For glycerol on 0.8 ML Cu/Mo_2C, on top of the broad propylene peak there is another sharp peak at 363K, which is contributed from allyl alcohol/propanal formation that only occurs on the Cu/Mo_2C interface.[36]

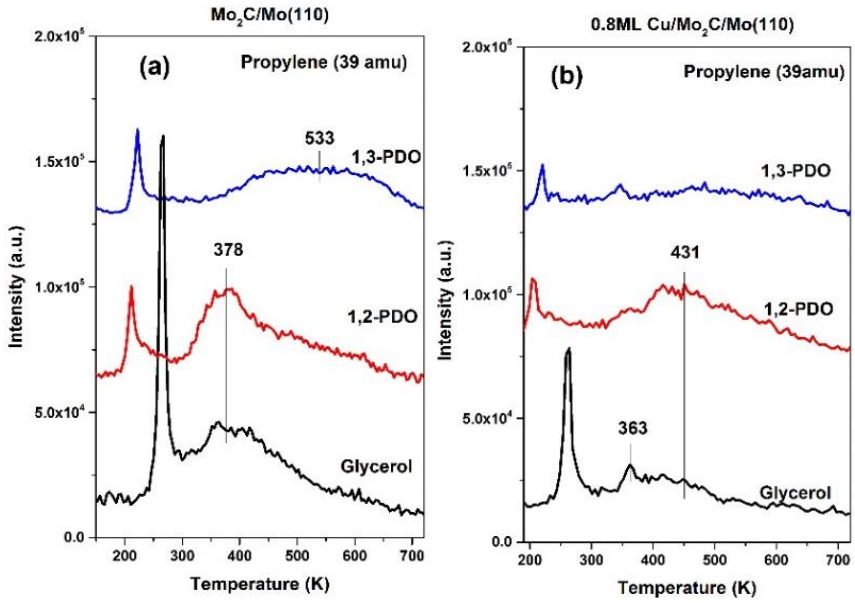

Figure 4.2 TPD spectra of propylene following an exposure of 4L glycerol, 1,2-PDO and 1,3-PDO over hydrogen pre-dosed (a) Mo_2C and (b) 0.8ML Cu/Mo_2C.

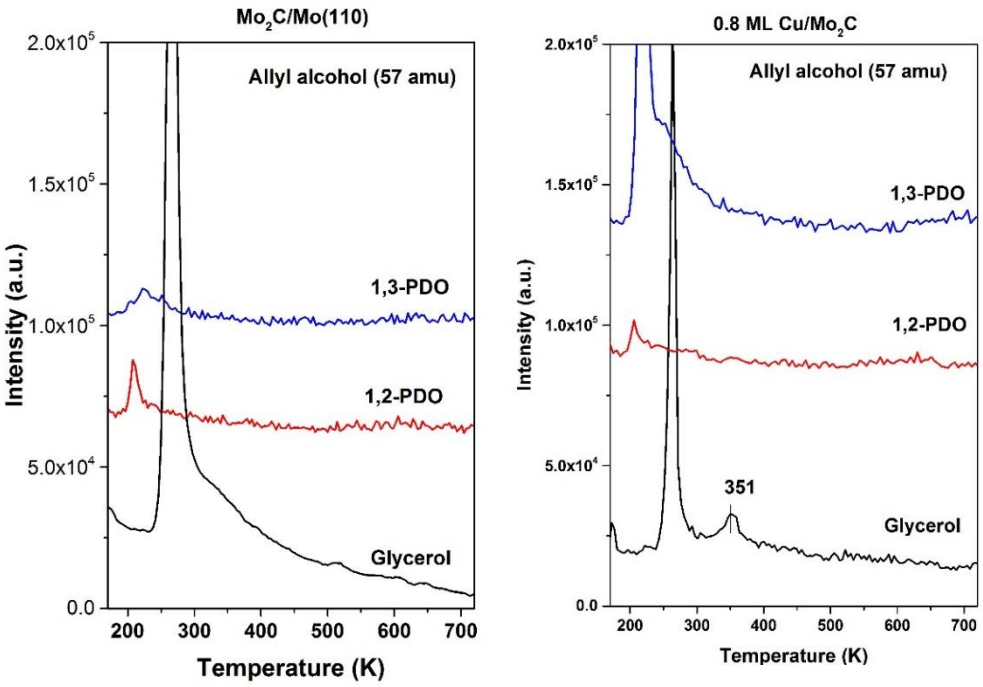

Figure 4.3. Spectra of allyl alcohol after an exposure of 4L glycerol, 1,2-PDO and 1,3-PDO over hydrogen pre-dosed (a) Mo_2C/Mo(110) and (b) 0.8ML Cu/Mo_2C/Mo(110).

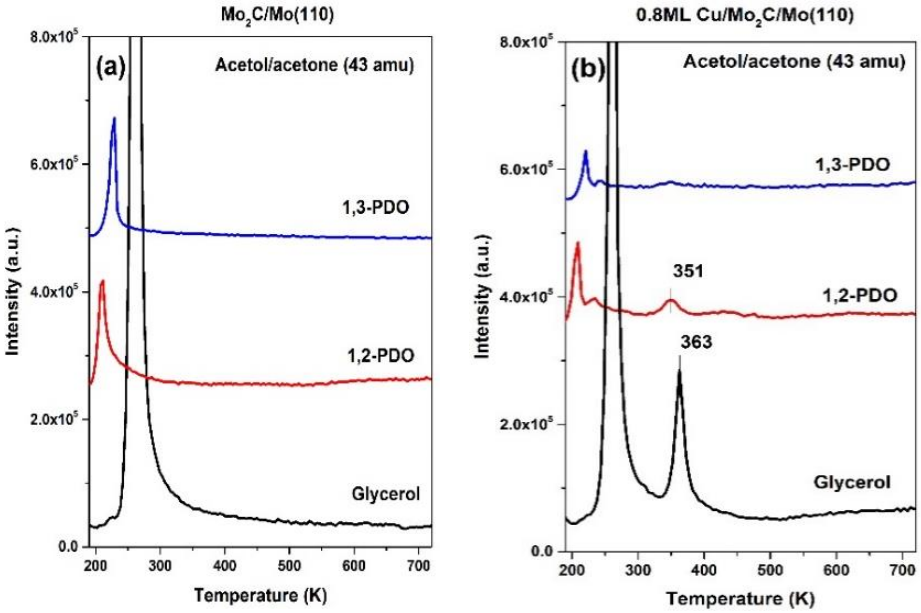

Figure 4.4 TPD spectra of acetol/acetone following an exposure of 4L glycerol, 1,2-PDO and 1,3-PDO over hydrogen pre-dosed (a) Mo_2C and (b) 0.8ML Cu/Mo_2C.

Figure 4.4 shows the desorption of acetol and acetone (43 amu) produced from glycerol and 1,2-PDO. One should note that both acetol and acetone have a common cracking fragment of 43 amu. Similar to the 39 amu spectra in Figure 4.2, the sharp peaks at 263K, 211K and 229K in Figure 4.4 are from the cracking fragment of glycerol, 1,2- and 1,3-PDO, respectively. On Mo_2C (Figure 4.4 (a)), there are no additional peaks besides the cracking fragments of the reactant molecules. On the 0.8 ML Cu/Mo_2C surface (Figure 4.4 (b)) the peaks around 363K and 351K are observed for glycerol and 1,2-PDO, respectively. Since the amount of acetol and acetone produced from glycerol and 1,2-PDO increases as the Cu coverage increases, these products are likely formed on the Cu site of the Cu/Mo_2C surfaces, rather than the Cu/Mo_2C interfacial site. The production of acetol from glycerol and acetone from 1,2-PDO indicates that glycerol and 1,2-PDO undergo similar bond breaking sequence on the Cu site, which selectively cleaves the primary C-O bond and dehydrogenates the secondary –OH group. On the other hand, no 43 amu peak is produced from 1,3-PDO. Instead, 29 amu and 58 amu peaks at 341K were detected after dosing 1,3-PDO. As the Cu coverage increases, the peak areas of 29 amu and 58 amu also increase, suggesting that propanal is produced from 1,3-PDO on the Cu sites. The reaction pathways of glycerol, 1,2- and 1,3-PDO are summarized in Scheme 4.1. Compared to the Mo site that cleaves all the C-O bonds of C3 polyols, the Cu site can only cleave one C-O bond, likely due to the lower oxygen binding energy of Cu. Note that since the Cu modifier may agglomerate during the deposition process at 600K, the surfaces with Cu coverage greater than 1ML are not discussed in this work. The quantification results of all the C3 products from glycerol, 1,2- and 1,3-PDO on the Mo_2C and 0.8ML Cu/Mo_2C surfaces are shown in Table 4.1.

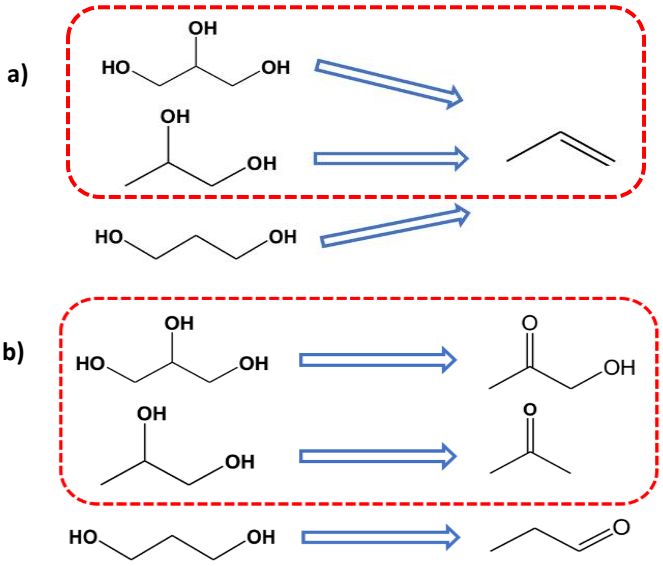

Scheme 4.1 Reaction pathways of glycerol, 1,2- and 1,3-PDO over (a) Mo site and (b) Cu site on Mo_2C and Cu/Mo_2C surfaces.

Table 4.1 Activity (molecules per metal atom) of C3 products from glycerol and diols over corresponding surfaces.

	θ_{Cu} (ML)	Propylene	Acetol	Acetone	Allyl alcohol /Propanal	Total
Glycerol	0	0.061	0.000	0.000	0.000	0.061
	0.8	0.021	0.051	0.000	0.007	0.079
1,2-PDO	0	0.040	0.000	0.000	0.000	0.040
	0.8	0.026	0.000	0.006	0.000	0.032
1,3-PDO	0	0.030	0.000	0.000	0.000	0.030
	0.8	0.013	0.000	0.000	0.007	0.020

θ_{Cu}: coverage of copper. ML: monolayer

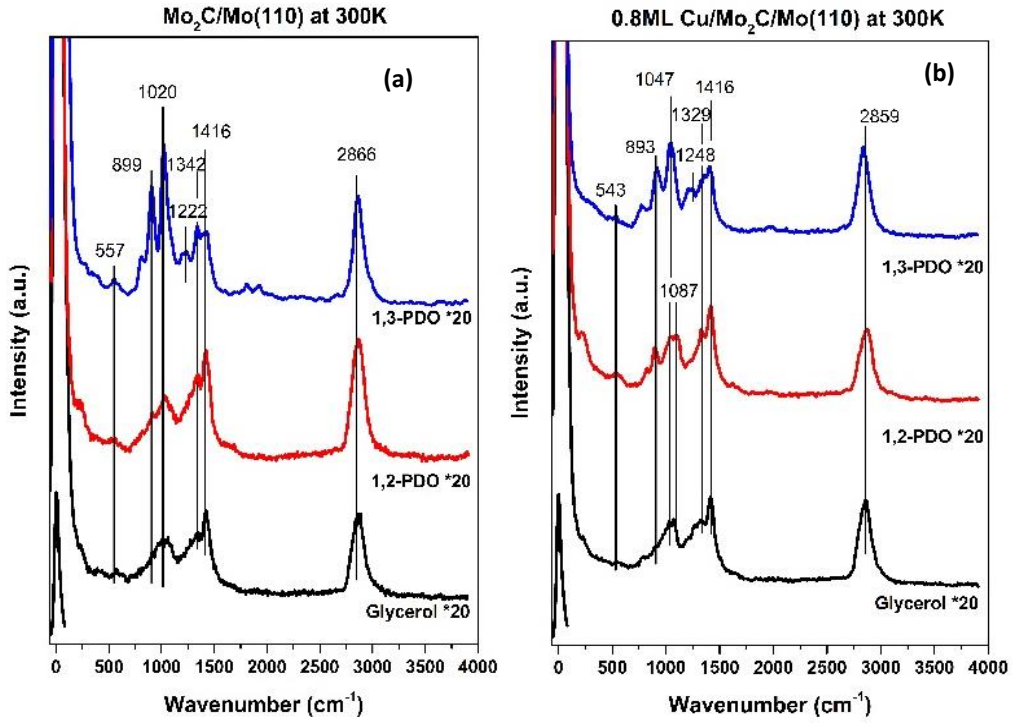

Figure 4.5. Comparison of HREEL spectra after an exposure of 4L of glycerol, 1,2-and 1,3-PDO over hydrogen pre-dosed (a) Mo_2C and (b) 0.8ML Cu/Mo_2C at 300K.

HREELS measurements were performed to compare the surface reaction intermediates of glycerol and 1,2- and 1,3-PDO. The vibrational mode assignments are summarized in Table 4.2. Shown in Figure 4.5 are the HREEL spectra of glycerol, 1,2- and 1,3-PDO on the Mo_2C and 0.8ML Cu/Mo_2C surfaces at 300K. In general, the spectra of glycerol and 1,2-PDO are very similar on both the Mo_2C and 0.8ML Cu/Mo_2C surfaces, indicating that both molecules likely produce similar intermediates. The spectra for molecularly adsorbed glycerol, 1,2- and 1,3-PDO are shown in Figure 4.6. Even though the spectra of molecularly adsorbed 1,2-PDO and glycerol appear slightly different, the spectra of both molecules become very similar when temperature is increased to 300K and above. In contrast, the 1,3-PDO spectra on both surfaces are quite different than the other two molecules, especially in the region between 890 cm^{-1} and 1100 cm^{-1}. The $\rho_r(CH_2)$ mode

of 1,3-PDO on both Mo_2C (899 cm^{-1}) and 0.8ML Cu/Mo_2C (893 cm^{-1}) are more intense than those of glycerol and 1,2-PDO on the corresponding surfaces, consistent with the fact that there are more -CH_2 groups in 1,3-PDO than in glycerol and 1,2-PDO. Furthermore, on Mo_2C, the ν(CO) mode at 1020 cm^{-1} of 1,3-PDO is more intense than those of 1,2-PDO and glycerol, indicating that the C-O bond of 1,3-PDO is better preserved than those of glycerol and 1,2-PDO, which is consistent with the TPD observations that propylene is formed at higher onset temperature from 1,3-PDO (350K) than from glycerol (210 K) or 1,2-PDO (300K). Additionally, on the 0.8ML Cu/Mo_2C surface, there are two peaks at 1047 cm^{-1} and 1087 cm^{-1} that represent the ν(CO) mode for 1,2-PDO and glycerol, respectively. These two peaks correspond to the two types of C-O bonds in 1,2-PDO and glycerol (primary and secondary). In comparison, only one peak is observed at 1047 cm^{-1} for 1,3-PDO, consistent with the presence of only one type of C-O bond (primary) in 1,3-PDO. When the surface temperature is further increased to 400K, glycerol and 1,2-PDO still show very similar spectra on both Mo_2C and 0.8ML Cu/Mo_2C, but the differences between 1,3-PDO and the other two become more significant. (Figure 4.7)

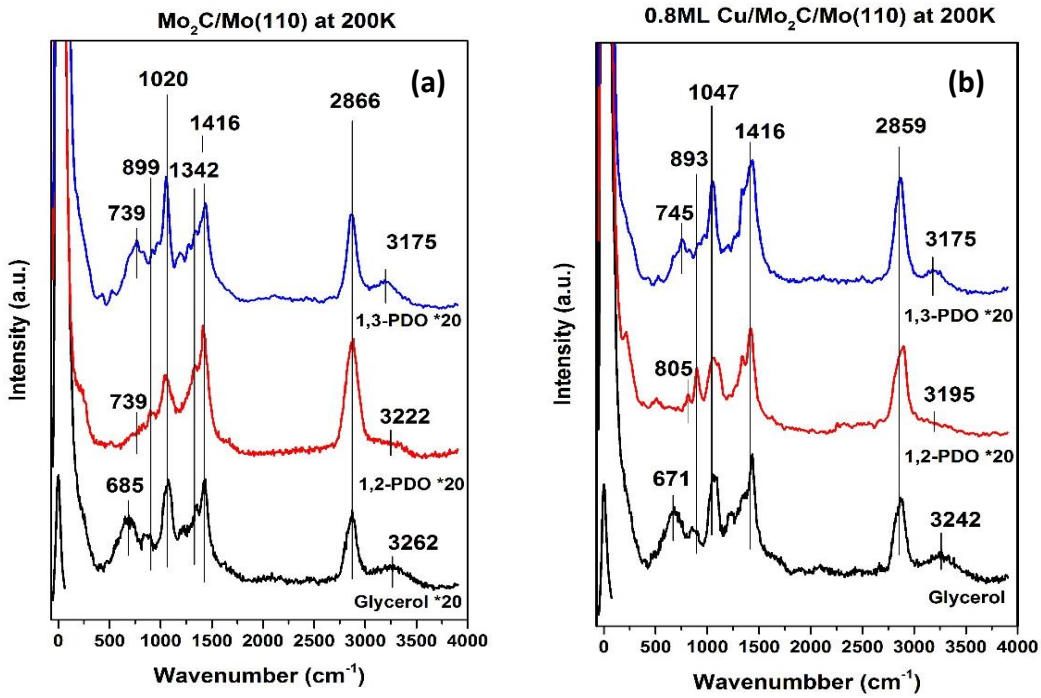

Figure 4.6. Comparison of HREEL spectra after an exposure of 4L of glycerol, 1,2-and 1,3-PDO over hydrogen pre-dosed (a) Mo_2C/Mo(110) and 0.8ML Cu/Mo_2C/Mo(110) at 200K.

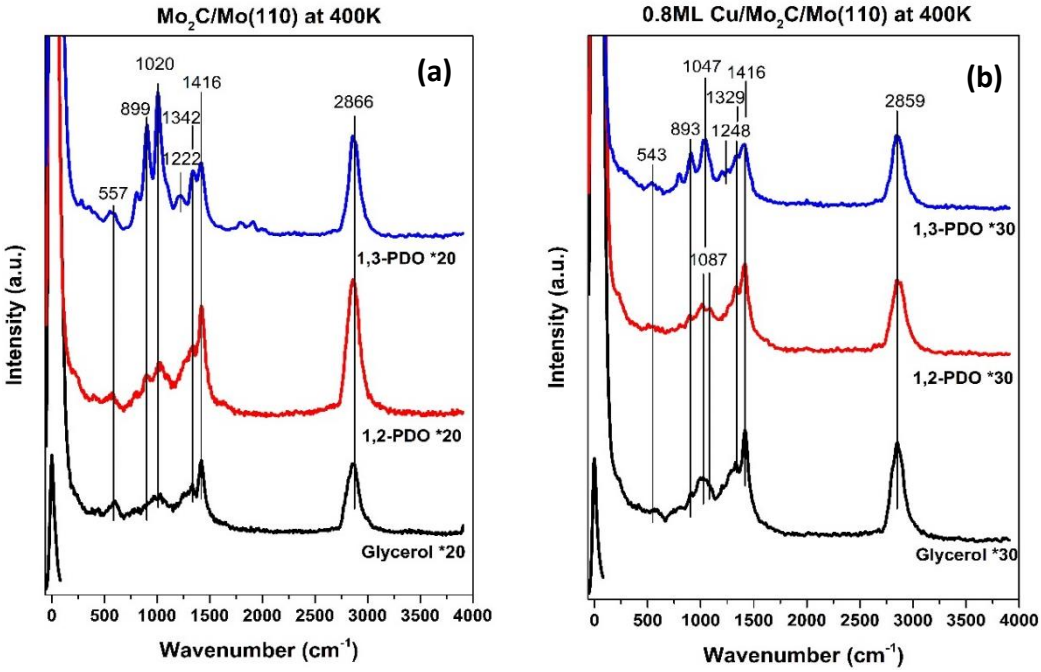

Figure 4.7. Comparison of HREEL spectra after an exposure of 4L glycerol, 1,2- and 1,3-PDO over hydrogen pre-dosed (a) Mo_2C/Mo(110) and (b) 0.8ML Cu/Mo_2C/Mo(110) at 400K.

Table 4.2 Vibrational mode assignments for glycerol, 1,2- and 1,3-PDO over corresponding surfaces

Mode	Frequency (cm^{-1})			
	Ethylene glycol on Mo_2C/Mo(110)[a]	1,2-PDO liquid IR [b]	Mo_2C/Mo(110)[c]	0.8ML Cu/Mo_2C/Mo(110) [c]
$\boldsymbol{\nu(MO)}$			557	543
$\boldsymbol{\rho_r(CH_2)}$	879	839	899	893
$\boldsymbol{\nu(CO)}$	1069	1046	1020	1047
$\boldsymbol{\nu(CO)}$		1138		1087
$\boldsymbol{\rho_t(CH_2)}$	1260	1289	1222	1248
$\boldsymbol{\rho_w(CH_2)}$	1360		1342	1329
$\boldsymbol{\delta(CH_2)}$	1441	1455	1416	1416
$\boldsymbol{\nu(CH)}$	2916	2935	2866	2859

δ - deformation, ρ_r - rocking, ν - stretching, ρ_t - torsion, ρ_w - wagging.

[a] ref [40],

[b] ref [41],

[c] This work

4.4 Conclusions

In summary, TPD experiments show that glycerol and 1,2-PDO undergo similar bond breaking sequence on the Mo and Cu sites of the Cu/Mo_2C surface. The Mo site tends to cleave all the C-O bond of both molecules to form propylene, while the Cu site breaks the primary C-O bonds to form acetol and acetone, respectively. The resemblance between the HREEL spectra of 1,2-PDO and glycerol indicates that glycerol and 1,2-PDO likely undergo primary C-O bond scission to form similar intermediates. Overall, these results suggest that 1,2-PDO can potentially

be used as a surrogate molecule for glycerol. The higher vapor pressure of 1,2-PDO eases the dosing process in UHV chambers and should allow for gas-phase flow reactor evaluations. The simpler structure of 1,2-PDO should also significantly reduce the computational expense for activation barrier calculations. These will facilitate further mechanistic studies on the C-O bond breaking sequence of glycerol and provide insights into designing more efficient catalysts for the selective HDO of glycerol.

4.5 Acknowledgements

Reprinted with permission from *Lin, Z., Wan, W. & Chen, J. G. 1,2-Propanediol as a Surrogate Molecule of Glycerol for Mechanistic Studies of Selective Hydrodeoxygenation Reactions over Mo_2C and Cu/Mo_2C Surfaces. ACS Sustain. Chem. Eng. 7, 8077–8082 (2019)*. Copyright © 2019 American Chemical Society. I acknowledge Dr. Weiming Wan for his help with experiments and valuable discussion.

4.6 References

(1) Huber, G. W.; Iborra, S.; Corma, A. Synthesis of Transportation Fuels from Biomass: Chemistry, Catalysts, and Engineering. *Chem. Rev.* **2006**, *106* (9), 4044–4098. https://doi.org/10.1021/cr068360d.

(2) Chheda, J. N.; Huber, G. W.; Dumesic, J. A. Liquid-Phase Catalytic Processing of Biomass-Derived Oxygenated Hydrocarbons to Fuels and Chemicals. *Angew. Chemie - Int. Ed.* **2007**, *46* (38), 7164–7183. https://doi.org/10.1002/anie.200604274.

(3) Wang, H.; Male, J.; Wang, Y. Recent Advances in Hydrotreating of Pyrolysis Bio-Oil and Its Oxygen-Containing Model Compounds. *ACS Catal.* **2013**, *3* (5), 1047–1070. https://doi.org/10.1021/cs400069z.

(4) Jiang, Z.; Wan, W.; Lin, Z.; Xie, J.; Chen, J. G. Understanding the Role of M / Pt (111) (M = Fe , Co , Ni , Cu) Bimetallic Surfaces for Selective Hydrodeoxygenation of Furfural. *ACS Catal.* **2017**, *7* (9), 5758–5765. https://doi.org/10.1021/acscatal.7b01682.

(5) Wan, W.; Jenness, G. R.; Xiong, K.; Vlachos, D. G.; Chen, J. G. Ring-Opening Reaction of

Furfural and Tetrahydrofurfuryl Alcohol on Hydrogen-Predosed Iridium(1 1 1) and Cobalt/Iridium(1 1 1) Surfaces. *ChemCatChem* **2017**, *9* (9), 1701–1707. https://doi.org/10.1002/cctc.201601646.

(6) Sauter, W.; Bergmann, O. L.; Schröder, U. Hydroxyacetone: A Glycerol-Based Platform for Electrocatalytic Hydrogenation and Hydrodeoxygenation Processes. *ChemSusChem* **2017**, *10* (15), 3105–3110. https://doi.org/10.1002/cssc.201700996.

(7) Robinson, A. M.; Hensley, J. E.; Will Medlin, J. Bifunctional Catalysts for Upgrading of Biomass-Derived Oxygenates: A Review. *ACS Catal.* **2016**, *6* (8), 5026–5043. https://doi.org/10.1021/acscatal.6b00923.

(8) Lin, Z.; Chen, R.; Qu, Z.; Chen, J. G. Hydrodeoxygenation of Biomass-Derived Oxygenates over Metal Carbides: From Model Surfaces to Powder Catalysts. *Green Chem.* **2018**, *20* (12), 2679–2696. https://doi.org/10.1039/C8GC00239H.

(9) Lin, L.; Cunshan, Z.; Vittayapadung, S.; Xiangqian, S.; Mingdong, D. Opportunities and Challenges for Biodiesel Fuel. *Appl. Energy* **2011**, *88* (4), 1020–1031. https://doi.org/10.1016/j.apenergy.2010.09.029.

(10) Okoye, P. U.; Hameed, B. H. Review on Recent Progress in Catalytic Carboxylation and Acetylation of Glycerol as a Byproduct of Biodiesel Production. *Renew. Sustain. Energy Rev.* **2016**, *53*, 558–574. https://doi.org/10.1016/j.rser.2015.08.064.

(11) Ripoll, V.; de Vicente, G.; Morán, B.; Rojas, A.; Segarra, S.; Montesinos, A.; Tortajada, M.; Ramón, D.; Ladero, M.; Santos, V. E. Novel Biocatalysts for Glycerol Conversion into 2,3-Butanediol. *Process Biochem.* **2016**, *51* (6), 740–748. https://doi.org/10.1016/J.PROCBIO.2016.03.006.

(12) Metsoviti, M.; Paramithiotis, S.; Drosinos, E. H.; Galiotou-Panayotou, M.; Nychas, G.-J. E.; Zeng, A.-P.; Papanikolaou, S. Screening of Bacterial Strains Capable of Converting Biodiesel-Derived Raw Glycerol into 1,3-Propanediol, 2,3-Butanediol and Ethanol. *Eng. Life Sci.* **2012**, *12* (1), 57–68. https://doi.org/10.1002/elsc.201100058.

(13) Toraya, T.; Shirakashi, T.; Kosuga, T.; Fukui, S. Substrate Specificity of Coenzyme B12-Dependent Diol Dehydrase: Glycerol as Both a Good Substrate and a Potent Inactivator. *Biochem. Biophys. Res. Commun.* **1976**, *69* (2), 475–480. https://doi.org/10.1016/0006-291X(76)90546-5.

(14) Foraget, R. G.; Foster, M. A. Glycerol Fermentation in Klebsiella Pneumoniae: Functions of the Coenzyme B12-Dependent Glycerol and Diol Dehydratases. *J. Bacteriol.* **1982**, *149* (2), 413–419.

(15) Abeles, R. H.; Brownstein, A. M.; Randles, C. H. β-Hydroxypropionaldehyde, an Intermediate in the Formation of 1,3-Propanediol by Aerobacter Aerogenes. *Biochim. Biophys. Acta* **1960**, *41* (3), 530–531. https://doi.org/10.1016/0006-3002(60)90054-8.

(16) Carrettin, S.; McMorn, P.; Johnston, P.; Griffin, K.; Hutchings, G. J. Selective Oxidation of Glycerol to Glyceric Acid Using a Gold Catalyst in Aqueous Sodium Hydroxide. *Chem. Commun.* **2002**, No. 7, 696–697. https://doi.org/10.1039/b201112n.

(17) Qi, J.; Xin, L.; Chadderdon, D. J.; Qiu, Y.; Jiang, Y.; Benipal, N.; Liang, C.; Li, W. Electrocatalytic Selective Oxidation of Glycerol to Tartronate on Au/C Anode Catalysts in Anion Exchange Membrane Fuel Cells with Electricity Cogeneration. *Appl. Catal. B Environ.* **2014**, *154–155*, 360–368. https://doi.org/10.1016/j.apcatb.2014.02.040.

(18) Lemos, C. O. T.; Rade, L. L.; Barrozo, M. A. D. S.; Fernandes, L. D.; Cardozo-Filho, L.; Hori, C. E. Optimization of Catalytic Glycerol Etherification with Ethanol in a Continuous Reactor. *Energy and Fuels* **2017**, *31* (5), 5158–5164. https://doi.org/10.1021/acs.energyfuels.7b00194.

(19) Zhou, J.; Wang, Y.; Guo, X.; Mao, J.; Zhang, S. Etherification of Glycerol with Isobutene on Sulfonated Graphene: Reaction and Separation. *Green Chem.* **2014**, *16* (11), 4669–4679. https://doi.org/10.1039/C4GC01044B.

(20) Troncea, S. B.; Wuttke, S.; Kemnitz, E.; Coman, S. M.; Parvulescu, V. I. Hydroxylated Magnesium Fluorides as Environmentally Friendly Catalysts for Glycerol Acetylation. *Appl. Catal. B Environ.* **2011**, *107* (3–4), 260–267. https://doi.org/10.1016/j.apcatb.2011.07.021.

(21) Kim, I.; Kim, J.; Lee, D. A Comparative Study on Catalytic Properties of Solid Acid Catalysts for Glycerol Acetylation at Low Temperatures. *Appl. Catal. B Environ.* **2014**, *148–149*, 295–303. https://doi.org/10.1016/j.apcatb.2013.11.008.

(22) Karim, A. M.; Howard, C.; Roberts, B.; Kovarik, L.; Zhang, L.; King, D. L.; Wang, Y. In Situ X-Ray Absorption Fine Structure Studies on the Effect of PH on Pt Electronic Density during Aqueous Phase Reforming of Glycerol. *ACS Catal.* **2012**, *2* (11), 2387–2394. https://doi.org/10.1021/cs3005049.

(23) Esteve-Adell, I.; Crapart, B.; Primo, A.; Serp, P.; Garcia, H. Aqueous Phase Reforming of Glycerol Using Doped Graphenes as Metal-Free Catalysts. *Green Chem.* **2017**, *19* (13), 3061–3068. https://doi.org/10.1039/C7GC01058C.

(24) Katryniok, B.; Paul, S.; Dumeignil, F. Recent Developments in the Field of Catalytic Dehydration of Glycerol to Acrolein. *ACS Catal.* **2013**, *3* (8), 1819–1834. https://doi.org/10.1021/cs400354p.

(25) Zhang, H.; Hu, Z.; Huang, L.; Zhang, H.; Song, K.; Wang, L.; Shi, Z.; Ma, J.; Zhuang, Y.; Shen, W.; et al. Dehydration of Glycerol to Acrolein over Hierarchical ZSM-5 Zeolites: Effects of Mesoporosity and Acidity. *ACS Catal.* **2015**, *5* (4), 2548–2558. https://doi.org/10.1021/cs5019953.

(26) Li, B.; Wang, J.; Yuan, Y.; Ariga, H.; Takakusagi, S.; Asakura, K. Carbon Nanotube-Supported RuFe Bimetallic Nanoparticles as Efficient and Robust Catalysts for Aqueous-Phase Selective Hydrogenolysis of Glycerol to Glycols. *ACS Catal.* **2011**, *1* (11), 1521–1528. https://doi.org/10.1021/cs200386q.

(27) Huang, Z.; Cui, F.; Kang, H.; Chen, J.; Zhang, X.; Xia, C. Highly Dispersed Silica-Supported Copper Nanoparticles Prepared by Precipitation− Gel Method: A Simple but Efficient and Stable Catalyst for Glycerol Hydrogenolysis. *Chem. Mater.* **2008**, *20*, 5090–5099. https://doi.org/doi: 10.1021/cm8006233.

(28) Wang, S.; Liu, H. Selective Hydrogenolysis of Glycerol to Propylene Glycol on Cu–ZnO Catalysts. *Catal. Letters* **2007**, *117* (1–2), 62–67. https://doi.org/10.1007/s10562-007-9106-9.

(29) Dasari, M. A.; Kiatsimkul, P.-P.; Sutterlin, W. R.; Suppes, G. J. Low-Pressure Hydrogenolysis of Glycerol to Propylene Glycol. *Appl. Catal. A Gen.* **2005**, *281* (1–2), 225–231. https://doi.org/10.1016/J.APCATA.2004.11.033.

(30) Guo, L.; Zhou, J.; Mao, J.; Guo, X.; Zhang, S. Supported Cu Catalysts for the Selective Hydrogenolysis of Glycerol to Propanediols. *Appl. Catal. A Gen.* **2009**, *367* (1–2), 93–98. https://doi.org/10.1016/J.APCATA.2009.07.040.

(31) Mane, R. B.; Hengne, A. M.; Ghalwadkar, A. A.; Vijayanand, S.; Mohite, P. H.; Potdar, H. S.; Rode, C. V. Cu:Al Nano Catalyst for Selective Hydrogenolysis of Glycerol to 1,2-Propanediol. *Catal. Letters* **2010**, *135* (1–2), 141–147. https://doi.org/10.1007/s10562-010-0276-5.

(32) Yuan, Z.; Wang, J.; Wang, L.; Xie, W.; Chen, P.; Hou, Z.; Zheng, X. Biodiesel Derived Glycerol Hydrogenolysis to 1,2-Propanediol on Cu/MgO Catalysts. *Bioresour. Technol.* **2010**, *101* (18), 7088–7092. https://doi.org/10.1016/J.BIORTECH.2010.04.016.

(33) Akiyama, M.; Sato, S.; Takahashi, R.; Inui, K.; Yokota, M. Dehydration–hydrogenation of Glycerol into 1,2-Propanediol at Ambient Hydrogen Pressure. *Appl. Catal. A Gen.* **2009**, *371* (1–2), 60–66. https://doi.org/10.1016/J.APCATA.2009.09.029.

(34) Nakagawa, Y.; Tomishige, K. Heterogeneous Catalysis of the Glycerol Hydrogenolysis. *Catal. Sci. Technol.* **2011**, *1* (2), 179. https://doi.org/10.1039/c0cy00054j.

(35) Zhu, S.; Gao, X.; Zhu, Y.; Zhu, Y.; Zheng, H.; Li, Y. Promoting Effect of Boron Oxide on Cu/SiO2 Catalyst for Glycerol Hydrogenolysis to 1,2-Propanediol. *J. Catal.* **2013**, *303*, 70–79. https://doi.org/10.1016/J.JCAT.2013.03.018.

(36) Wan, W.; Ammal, S. C.; Lin, Z.; You, K.-E.; Heyden, A.; Chen, J. G. Controlling Reaction Pathways of Selective C–O Bond Cleavage of Glycerol. *Nat. Commun.* **2018**, *9* (1), 4612. https://doi.org/10.1038/s41467-018-07047-7.

(37) Skoplyak, O.; Barteau, M. A.; Chen, J. G. Enhancing H2 and CO Production from Glycerol Using Bimetallic Surfaces. *ChemSusChem* **2008**, *1* (6), 524–526. https://doi.org/10.1002/cssc.200800053.

(38) Hwu, H. H.; Chen, J. G. Reactions of Methanol and Water over Carbide-Modified Mo(1 1 0). *Surf. Sci.* **2003**, *536* (1–3), 75–87. https://doi.org/10.1016/S0039-6028(03)00607-1.

(39) Frühberger, B.; Chen, J. G. Reaction of Ethylene with Clean and Carbide-Modified Mo(110): Converting Surface Reactivities of Molybdenum to Pt-Group Metals. *J. Am. Chem. Soc.* **1996**, *118* (46), 11599–11609. https://doi.org/10.1021/ja960656l.

(40) Yu, W.; Salciccioli, M.; Xiong, K.; Barteau, M. A.; Vlachos, D. G.; Chen, J. G. Theoretical and Experimental Studies of C-C versus C-O Bond Scission of Ethylene Glycol Reaction Pathways via Metal-Modified Molybdenum Carbides. *ACS Catal.* **2014**, *4* (5), 1409–1418. https://doi.org/10.1021/cs500124n.

(41) Ayre, C. R.; Madix, R. J. The Adsorption and Reaction of 1,2-Propandiol on Ag (110) under Oxygen Lean Conditions. *Surf. Sci.* **1994**, *303*, 279–296. https://doi.org/10.1016/0039-6028(94)90776-5.

Chapter 5: Controlling Extent of C-O Bond Scission of Glycerol over Molybdenum Nitride Surfaces

5.1 Introduction

Our world is currently undergoing a transition from a fossil fuel-based economy to a more sustainable one supported by various renewable energy technologies.[1,2] Many different approaches for replacing fossil fuels have been developed, among which biodiesel production is promising in that it can turn agricultural and animal wastes into fuels.[3] During the biodiesel production, glycerol is formed as a major byproduct. As biodiesel production continues to grow, a large amount of glycerol is produced, making glycerol abundant and relatively inexpensive.[4] Glycerol has also been identified as one of the top twelve biomass building blocks that can be converted into high-value chemicals and materials.[5] Therefore, implementing technologies for upgrading glycerol can significantly benefit the overall process economics. The multiple -OH functional groups in glycerol allow for conversion into a variety of value-added compounds. To date, various approaches for upgrading glycerol have been identified.[4] Glycerol can be upgraded through enzymatic transformation,[6–9] selective oxidation,[10,11] dehydration,[12,13] reforming,[14,15] etherification,[16,17] hydrogenolysis/hydrodeoxygenation (HDO).[4,18–20] Among these pathways, HDO is a particularly interesting route that yields different valuable chemicals. Nevertheless, the selective scission of specific C-O bonds in glycerol while preserving others remains as a challenge for the highly functionalized glycerol molecule. On the other hand, the presence of multiple -OH groups within glycerol also makes it a suitable model compound for studying higher sugar molecules. Previously, we have demonstrated Cu/Mo_2C as a promising HDO catalyst that allows for controllable C-O bond scission of glycerol.[21] By tuning the Cu coverage on Mo_2C, selective

cleavage of one, two, and three C-O bonds of glycerol can be achieved on the Cu site, Cu/Mo_2C interface site, and Mo_2C site of the catalytic surface, respectively. However, one issue with Mo_2C-based catalysts is that during the synthesis of powder Mo_2C catalyst, carbon layers accumulate on Mo_2C, lowering the activity of the surface and inhibiting the correlation between experimental results and density functional theory (DFT) calculations.[22] To solve these issues, we investigate Mo_2N as an alternative to Mo_2C. Mo_2N has been widely used for the removal of heteroatoms in hydrocarbons, such as N, O, and S, due to the strong interaction between Mo_2N and the heteroatom.[23] But to the best of our knowledge, there has not been a combined experimental and theoretical study on the glycerol hydrodeoxygenation reaction over a Mo_2N model surface so far. During the synthesis of Mo_2N, surface N can desorb in the form of N_2, thus avoiding the accumulation of large amount of N that may block the Mo sites. Instead, this synthesis procedure yields a clean N-terminated surface. In addition to the capability of Mo_2N to cleave all three C-O bonds of glycerol, the single layer of N atoms on the surface also changes the binding configuration of glycerol to facilitate the scission of two C-O bonds, which was only achievable on the Cu/Mo_2C interface. The addition of Cu changes the selectivity of the surface towards products of one C-O bond scission.

In this work, we combine model surface experiments and DFT calculations to demonstrate Mo_2N as an alternative for Mo_2C for tuning the C-O bond scission of glycerol. To investigate whether Mo_2N can catalyze both total and selective C-O bond scission for other C3 molecules, we also evaluated the reaction pathways of 1,2- and 1,3-propanediols on Mo_2N. Temperature-programed desorption (TPD) experiments were performed to probe the gas-phase reaction products and DFT calculations were performed to identify the glycerol HDO mechanism. The results suggest that Mo_2N has a similar activity to Mo_2C, with added functionality.

5.2 Materials and Methods

5.2.1 Synthesis of Mo_2N Thin Films

Mo_2N thin films were synthesized from parent metal foils under the same gas condition and temperature profile. 0.127 mm thick Nb (Alfa Aesar, 99.95%), 0.1 mm thick W (Alfa Aesar, 99.95%), and 0.1 mm thick Mo (Alfa Aesar, 99.95%) foils were cut into 1 cm x 2 cm rectangles. Cut foils were sonicated for 5 minutes in ethanol to remove surface oils, washed in deionized (DI) water, sonicated for 5 minutes in 1 M NaOH to remove surface oxides, and received a final wash in DI water prior to being loaded into a horizontal quartz tube furnace. All sonication was done at room temperature. Under a 150 sccm flow of 100% ammonia, the furnace temperature was ramped from 298 K to 1123 K at a linear rate over 2 hours. The temperature dwelled for 10 hours and was gradually cooled under the same gas condition. Once cooled to room temperature, the furnace was purged with Ar and nitride foils were removed.

5.2.2 Transition Metal Nitride Characterization

Mo_2N foils were characterized using both x-ray photoelectron spectroscopy (XPS) and x-ray diffraction (XRD). An ultra-high vacuum (UHV) chamber equipped with XPS was used to quantify parent metal to nitrogen ratios. The UHV chamber had a base pressure of 2×10^{-9} torr. XPS measurements were conducted using a PHI 5600 XPS with a hemispherical analyzer and an Al X-ray source. Multiplex scans were calibrated to the adventitious carbon peak at 284.4 eV. XRD measurements were conducted using a Cu Kα X-ray source. A PANalytical XPERT3 Powder XRD was used to collect both symmetric and glancing incident (3°) scans.

5.2.3 UHV Model Surface Experiments

The TPD experiments were conducted in a stainless-steel ultrahigh vacuum (UHV) chamber with a base pressure of $5*10^{-10}$ Torr. The chamber is equipped with a quadruple mass spectrometer, an Auger electron spectrometer (AES), an ion sputtering gun, and two metal sources for physical vapor deposition (PVD). The as-synthesized Mo_2N thin film is spot-welded to the chamber via two tantalum heating posts for resistive heating as well as cooling with liquid nitrogen. The temperature of the thin film is measured by a K-type thermocouple welded to the back of the film. In a typical experiment, the Mo_2N thin film was cleaned using Ne^+ sputtering, followed by annealing at 1200 K for 2 minutes. Residual surface carbon was removed by exposing the surface to oxygen at 800 K and sequent annealing to 1200 K. This cycle was repeated until the surface was free of carbon and oxygen as indicated by AES. Additionally, to synthesize Cu-modified Mo_2N, the clean Mo_2N surface was exposed to a heated Cu source for the PVD process. The Cu coverage was controlled by the deposition time and current. Upon the completion of surface synthesis, the surface was cooled to 150K and were expose to 4 L (Langmuir, 1 L = $1*10^{-6}$ Torr*s) of H_2 and 4 L of glycerol with the surface facing the stainless-steel dosing tube. The surface was then heated up at a heating rate of 3K/s in front of the mass spectrometer that recorded the desorption of gas-phase products.

All gases (H_2, O_2, Ne) were used without further purification. The reactant molecules (glycerol, 1,2- and 1,3-propanediol, Sigma Aldrich) were purified using freeze-pump-thaw cycles.

5.2.4 DFT Calculations

The deoxygenation mechanism of glycerol was examined on the γ-Mo_2N(111) surface using density functional theory calculations. All structural optimizations and energy calculations were performed with the Vienna *ab initio* simulation package (VASP).[24–27] The calculation

methodology relied on a generalized gradient approximation (GGA) within the Perdew-Burke-Ernzerhof formalism (PBE)[28] along with Grimme's D3 dispersion correction.[29] A cut-off energy of 500 eV was selected for the plane-wave basis. Following the procedure explained by Henson and coworkers,[30] we constructed the structure of bulk fcc γ-Mo_2N by removing 50% of the nitrogen atoms from the perfect fcc structure in the 100/010 direction to obtain a ratio of Mo:N = 2:1. The optimized structure became tetragonal with cell parameters of 4.24 Å and 3.97 Å with the selected level of theory. These values are in good agreement with the experimental value of 4.16 Å from the X-ray diffraction[31] and 4.19-4.23 Å from previous DFT calculations with different levels of theory.[30,32,33] Here, we chose the N-terminated Mo_2N(111) surface for the mechanistic study because the (111) surface is one of the major exposed surfaces of the Mo_2N catalysts[34–36] and the N-terminated (111) surface has been reported to be thermodynamically more stable than the Mo-terminated (111) surface.[37] The (2×2) surface unit with cell parameters of (11.98 Å × 9.95 Å × 22.17 Å) considered here consists of 7 atomic layers of Mo_2N and a 15 Å vacuum added in *z*-direction. In order to create a nonpolar slab, both sides of the slab are terminated by an N-layer. A Monkhorst-Pack (MP)[38] k-point mesh of 3×3×1 was used, and all atoms were fully relaxed except for the bottom two atomic layers of Mo_2N during structural optimization. Dipole and quadrupole corrections to the energy were taken into account using a modified version of the Makov and Payne method[39] and Harris-Foulke-type corrections[40] were included for the forces. The climbing image-NEB[41] and Dimer methods[42,43] were used to optimize all transition state structures.

5.3 Results and Discussion

5.3.1 Comparison of Glycerol Reaction Pathways on Mo_2N and Mo_2C

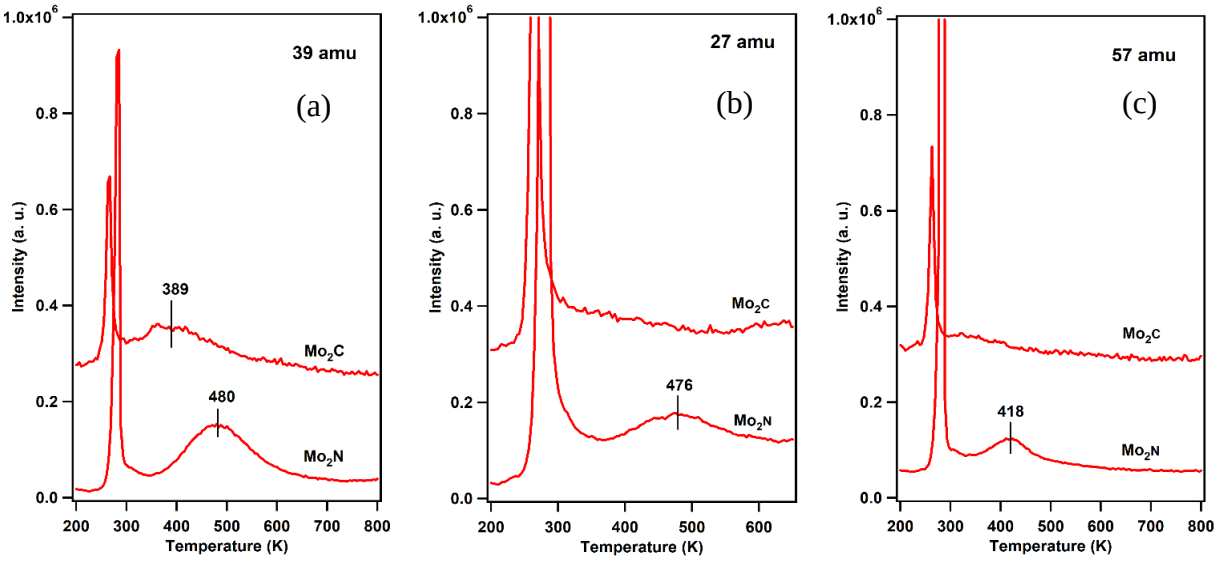

Figure 5.1. Comparison of temperature-programmed desorption spectra of (a) propylene (39 amu), (b) propanal (27 amu), and (c) allyl alcohol (57 amu) from H_2 pre-adsorbed Mo_2N and Mo_2C surfaces after exposing the surfaces to 4L of glycerol.

TPD experiments were performed to compare the reaction pathways of glycerol over Mo_2N and Mo_2C. The results show that both Mo_2N and Mo_2C can break all the C-O bonds in glycerol to form propylene. In addition, Mo_2N can also break two C-O bonds of glycerol to produce propanal and allyl alcohol. Figure 5.1 compares the desorption of propylene, propanal, and allyl alcohol from Mo_2N and Mo_2C after dosing glycerol to the surfaces. From Figure 5.1 (a), propylene is produced on both surfaces. On Mo_2C, the propylene peak has an onset temperature of around 300 K and a peak temperature of 389 K. On Mo_2N, the propylene peak has higher onset (~350 K) and peak (480 K) temperatures. This suggests that both surfaces are active for breaking all C-O bonds of glycerol. Figures 5.1 (b) and (c) show the spectra of propanal and allyl alcohol on Mo_2N and Mo_2C. On Mo_2C, no such molecules are produced. But on Mo_2N, propanal desorption was

observed, with a peak temperature of 476 K. Allyl also form over Mo_2N, with a desorption peak temperature of 418 K. Clearly, while Mo_2C only catalyzes three C-O bond scissions of glycerol to produce propylene, Mo_2N is active for breaking three or two C-O bonds of glycerol to form propylene, allyl alcohol, and propanal. The formation of products from two C-O bond scissions, namely allyl alcohol and propanal, is only achievable on the Cu/Mo_2C interface, according to our previous study.[21]

5.3.2 Reaction Pathways on the Mo_2N and Cu sites of Cu/Mo_2N

In order to probe the effect of Cu addition on the reaction pathway, TPD experiments of surfaces with different Cu coverages were performed. From these experiments, two distinct sites were identified, the Mo_2N site and the Cu site. The reaction pathways of glycerol on the Cu/Mo_2N system are summarized in Scheme 5.1. On the Mo_2N site, glycerol can undergo three C-O bond scissions to form propylene, or two C-O bond scissions to produce allyl alcohol and propanal. On the Cu site, glycerol can only undergo one C-O bond scission to form acetol. Figure 5.2 (a)-(d) show the different products observed on the Mo_2N surface modified by different coverages of Cu. In Figure 5.2 (a), propylene desorption peaks were observed on all surfaces spanning from 350 K to 700 K, with a peak temperature of 480 K. As the Cu coverage increases, the propylene yield decreases, as indicated by the decrease in peak area, suggesting that propylene is formed on the Mo_2N site. This observation is similar to that on Mo_2C.[21] Figure 5.2(b) shows the desorption of propanal, with a peak temperature of 476 K. The yield of propanal also decreases with the increase of Cu coverage, suggesting that propanal is produced on the Mo_2N site. In addition to the propanal peaks, there is another sharp peak at 368K, which is part of the cracking pattern of another product, acetol, that will be discussed further in the next paragraph. In Figure 5.2 (c), the desorption of allyl alcohol was observed with a peak temperature of 418 K. Similar to the propylene and propanal

peaks, the propanal peak area also decrease as the Cu coverage increases. This suggests that all three molecules are produced on the Mo_2N site. Figure 5.2 (d) shows the desorption peak of acetol, a product formed after only one C-O bond scission of glycerol. In contrast to all the other products, the yield of acetol increases as Cu coverage increases, suggesting that acetol is formed on the Cu site of the surface. This result is similar to that on the Cu site of the Cu/Mo_2C surface.[21]

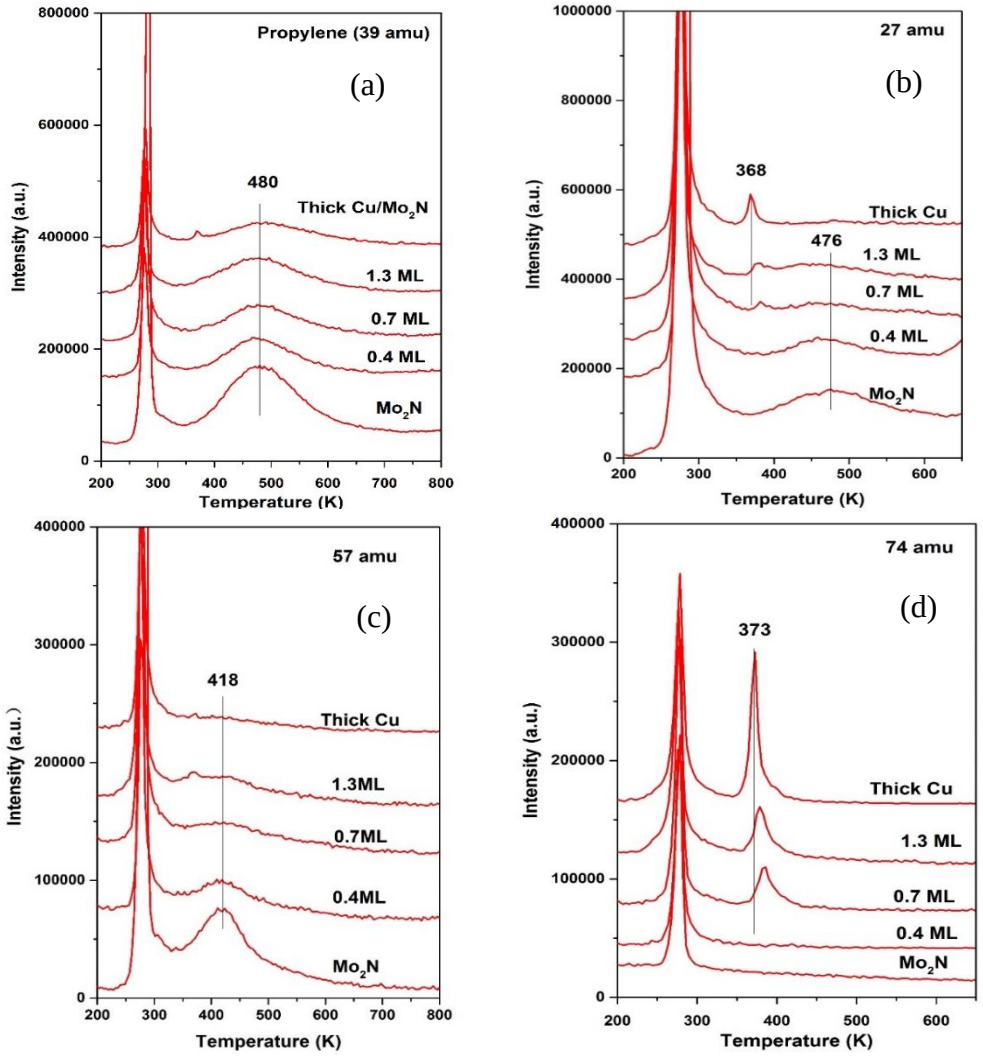

Figure 5.2. Desorption of (a) propylene (m/z = 39), (b) propanal (m/z = 27), (c) allyl alcohol (m/z = 57), and (d) acetol (m/z = 74) after an exposure of 4L of glycerol on hydrogen pre-adsorbed Mo_2N surfaces modified by different coverages of Cu.

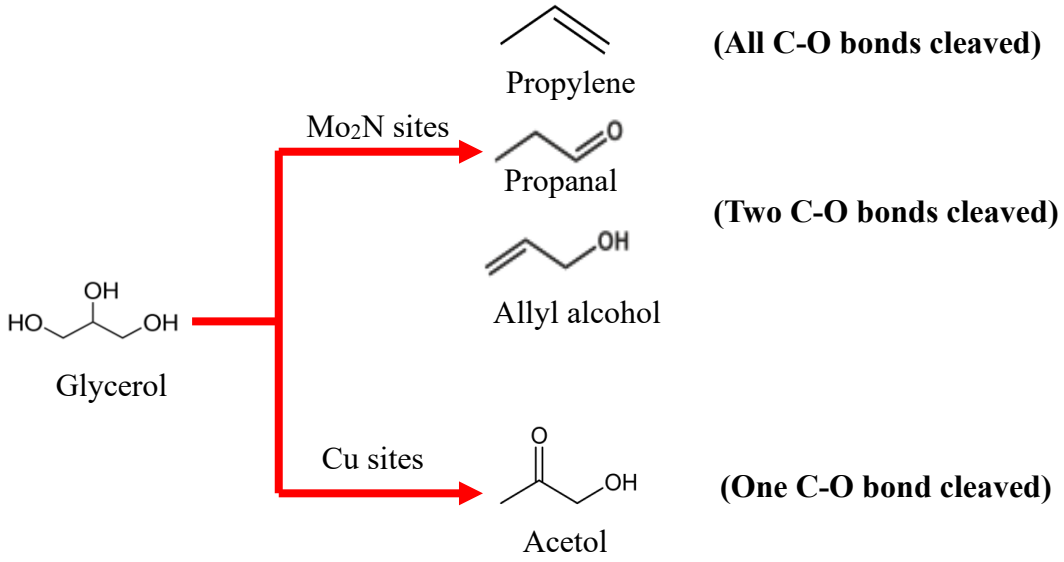

Scheme 5.1. Summary of reaction pathways of the selective hydrodeoxygenation of glycerol on the Mo_2N and Cu sites of the Cu/Mo_2N surface.

5.3.3 Quantification Results of the Reactions

Quantification of product yields from the glycerol reactions on the corresponding surfaces was performed and the results are shown in Figure 5.3 and Table 5.1. The total product yields on all surfaces are comparable to those on the Cu/Mo_2C system.[21] A change in product distribution was noticed as the Cu coverage was varied. On Mo_2N, propylene accounts for 51% of the total yield, while propanal and allyl alcohol take up 23% and 26%, respectively. As the Cu coverage increases, the yields of propylene, propanal, and allyl alcohol decrease. In the meantime, the acetol yield continues to increase and becomes dominant on the thick Cu surface.

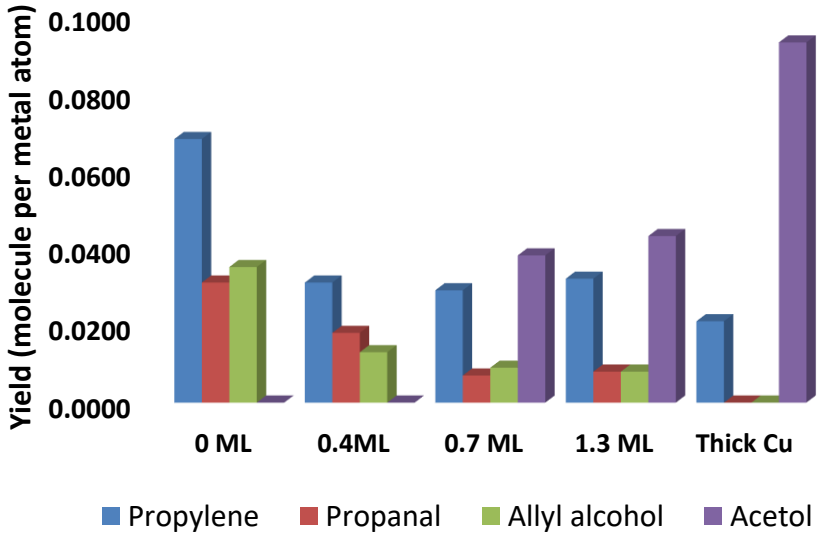

Figure 5.3. Product distribution from the glycerol TPD experiments.

Table 5.1. Product yields (molecule per metal atom) from glycerol on Mo_2N and Cu/Mo_2N with corresponding Cu coverages. The selectivity of the products is shown in parenthesis

	0 ML Cu	**0.4ML Cu**	**0.7 ML Cu**	**1.3 ML Cu**	**Thick Cu**
Propylene	0.068 (51%)	0.031 (50%)	0.029 (35%)	0.032 (35%)	0.021 (18%)
Propanal	0.0310 (23%)	0.018 (29%)	0.0070 (8%)	0.008 (9%)	0.000 (0%)
Allyl alcohol	0.0350 (26%)	0.013 (21%)	0.009 (11%)	0.008 (9%)	0.000 (0%)
Acetol	0.000 (0%)	0.000 (0%)	0.038 (46%)	0.043 (47%)	0.093 (82%)
Total	0.1341	0.0620	0.0830	0.0910	0.114

5.3.4 Theoretical Investigation of the Deoxygenation Mechanism of Glycerol on Mo_2N Catalyst Model

The reaction mechanism of the glycerol HDO is examined computationally on the N-terminated $Mo_2N(111)$ surface using the DFT methodology to understand the experimentally observed trend in product selectivity. In our earlier work,[21] the glycerol HDO mechanism was examined at different active sites of a Cu/Mo_2C catalyst model. In agreement with the experimental observations, the calculated reaction energy profiles predicted that the Mo sites are very active for cleaving all three C-O bonds of glycerol producing propylene and the Cu/Mo_2C interface sites prefer to cleave two C-O bonds forming allyl alcohol and propanal. In contrast, the Cu sites are active for cleaving only one C-O bond leading to the formation of acetol. Our current experimental studies on the Cu/Mo_2N catalysts (Table 5.1) revealed that the product yield of acetol increases with increasing Cu coverage suggesting that acetol is produced mainly on the Cu surface. These results indicate that the Cu sites supported on both Mo_2C and Mo_2N behave similarly and that the glycerol HDO mechanism on the Cu surface supported on Mo_2N is expected to be very similar to that of the Mo_2C supported Cu surface which we examined in detail in our earlier reports.[21,44] However, the products observed on the clean Mo_2N and Mo_2C surfaces clearly differ for the glycerol HDO under similar operating conditions. While propylene is the only main product observed on the Mo_2C surface,[21] formation of allyl alcohol and propanal were also observed in addition to propylene on the Mo_2N surface (Table 5.1). Thus, in the present study, we examined the deoxygenation mechanism of glycerol on the N-terminated $Mo_2N(111)$ surface and compared the results with our earlier work on the $Mo_2C(0001)$ surface with the aim of understanding the difference in reaction mechanism on these two surfaces.

The elementary reaction pathways calculated for the glycerol deoxygenation reaction on the Mo_2N surface are illustrated in Figure 5.4, and the corresponding structures are depicted in Figures 5.5 and 5.6. The available adsorption sites on the N-terminated Mo_2N (111) surface are the surface Mo sites ($*_{Mo}$) and surface N sites ($*_N$). Only H atoms were found to adsorb on the N sites and all the other intermediate species adsorb on the Mo sites. As shown in the inset of Figure 5.4, glycerol prefers to adsorb on the Mo_2N surface with two oxygen atoms interacting with the surface Mo sites and the H atoms of two O-H groups exhibiting strong H-bonding interactions with the surface N atoms. The calculated binding energy (-1.56 eV) suggests that the adsorption of glycerol on the N-terminated Mo_2N surface is about 0.6 eV less stable than on the Mo_2C surface[21] where glycerol binds with all three oxygen atoms. In agreement with the results on the Mo_2C surface, activation barriers calculated for the initial O-H and C-OH bond cleavages of glycerol on the Mo_2N(111) surface (Figure 5.4) suggested that the O-H bond dissociations are preferred over C-OH bond dissociations. Furthermore, our calculations (Figure 5.4) predicted lower activation barriers for transferring H atoms from the OH groups to the nearest surface N atoms relative to the transfer to the nearest Mo sites and the secondary O-H bond scission to the surface N atom (E_{ZPE}^{act} = 0.11 eV) is both kinetically and thermodynamically preferred over the primary O-H scission (E_{ZPE}^{act} = 0.53 eV). The secondary O-H cleavage process producing an alkoxide species (CH_2OH-CHO-CH_2OH*, 2B) is exothermic by -1.46 eV which is very similar to that on the Mo_2C(0001) surface.[21] It should be noted here that the reactant and product states depicted in Figure 5.4 constitute one discrete state, although written as having multiple species for clarity, *i.e.*, the dissociated atoms/fragments stay on the surface and the energy calculations include the lateral interactions between these species.

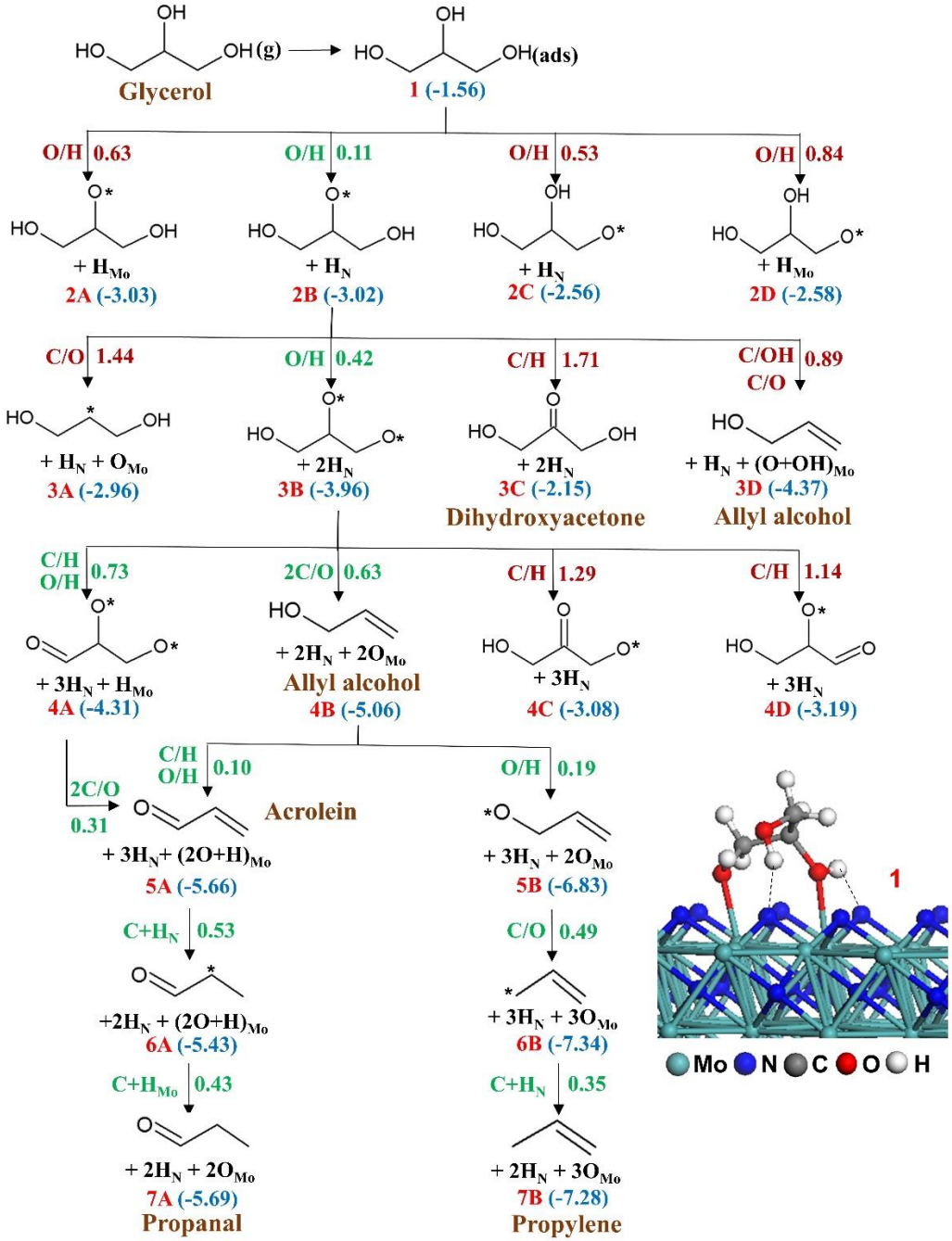

Figure 5.4. Schematic of the reaction pathways for glycerol decomposition on the N-terminated $Mo_2N(111)$ catalyst model. The activation barriers (in eV) of the elementary reactions with respective bond dissociation (/) or association (+) are shown next to the arrows. The numbers shown in parentheses are the energies of the intermediates relative to gas phase glycerol and the

initial catalyst model. All energies are zero-point corrected. * represents an undercoordinated atom and the most favorable pathway is shown in green.

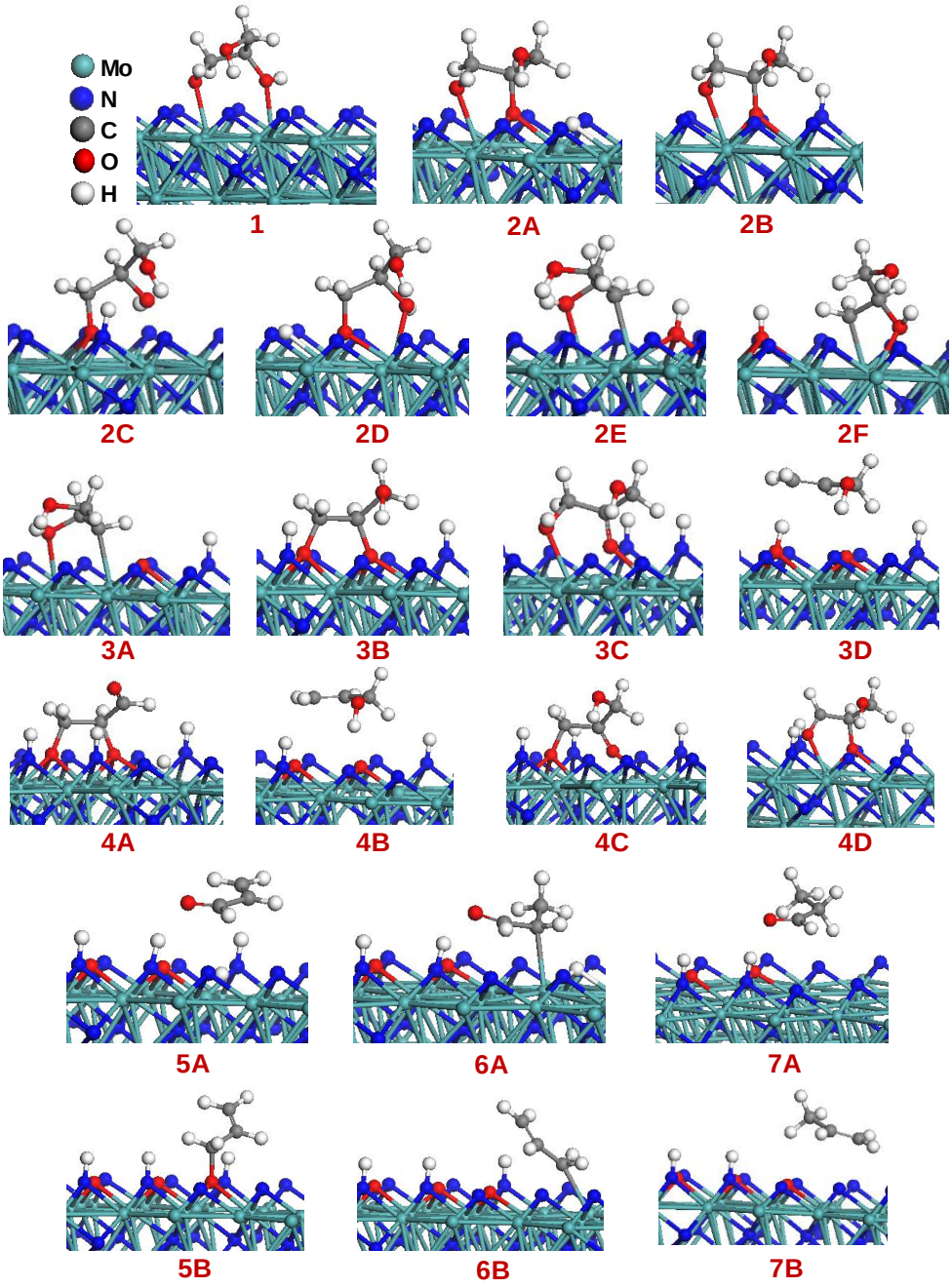

Figure 5.5. Side view of intermediate structures involved in the glycerol deoxygenation pathways on the N-terminated γ-Mo_2N (111) surface model. The numbers correspond to the states provided in Figure 5.4.

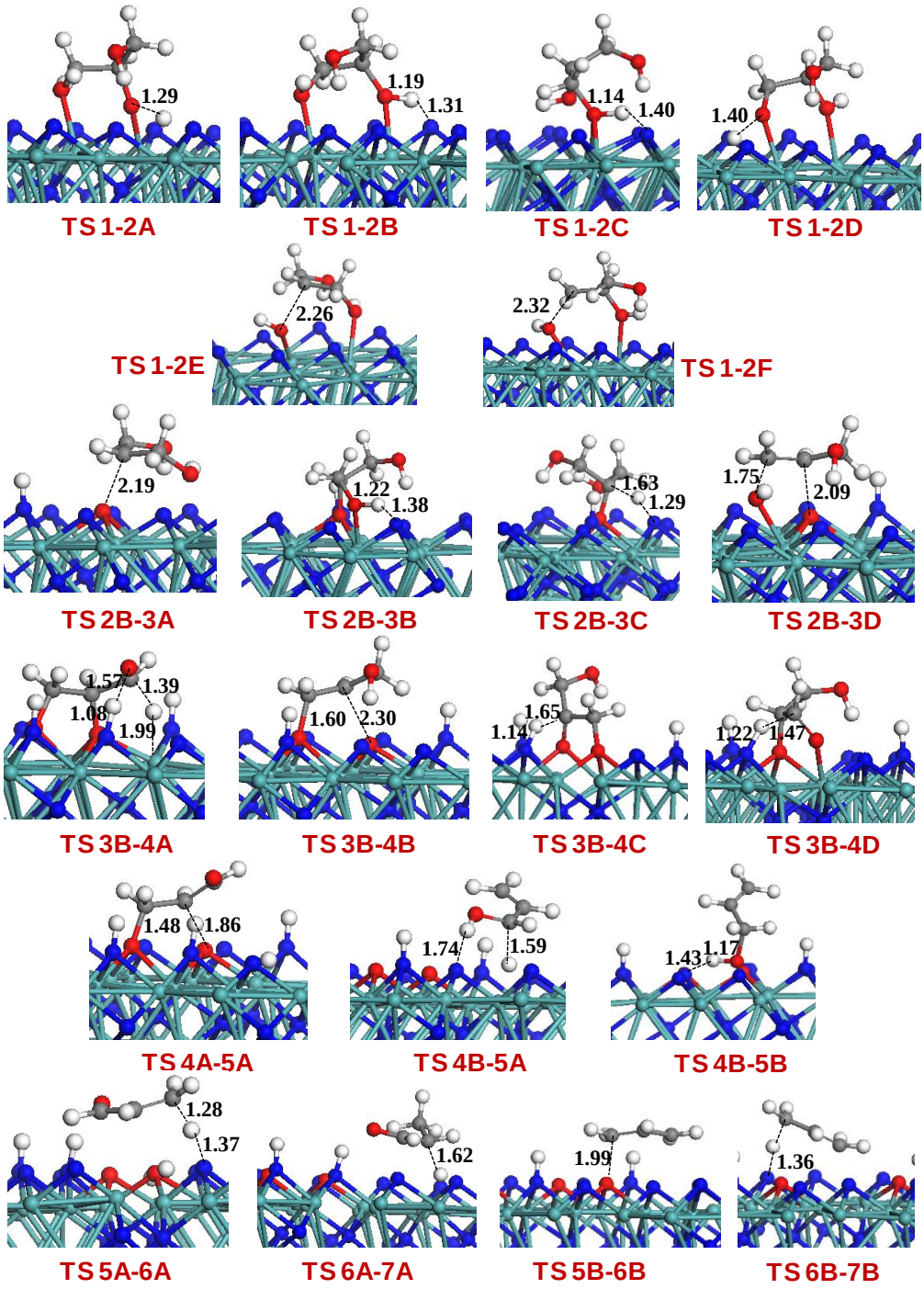

Figure 5.6. Side view of transition state (TS) structures involved in the glycerol deoxygenation pathways on the N-terminated γ-Mo_2N (111) surface model. The TS numbers correspond to the states provided in Figure 5.4. Bond distances shown next to the breaking/forming bonds are in Å.

The terminal O-H bond cleavage of the alkoxide species (2B) was found to be the next favorable elementary reaction with an activation barrier of 0.42 eV which is much lower than the C-O (2B → 3A) and C-H (2B → 3C) bond scissions at the secondary carbon. A concerted C-O cleavage at the secondary carbon and C-OH cleavage at the terminal carbon leading to the formation of allyl alcohol (2B → 3D) was found to be thermodynamically more favorable by 0.41 eV relative to the O-H cleavage; however, the required activation barrier for this step is 0.47 eV higher than the O-H cleavage. It appears that the favorable pathway for the formation of allyl alcohol is a concerted cleavage of two C-O bonds from the intermediate CH_2OH-CHO-CH_2O* (3B) which possesses a lower activation barrier (E_{ZPE}^{act} = 0.63 eV) than the C-H bond scissions at the middle (3B → 4C) or terminal (3B → 4D) carbon atoms. The third O-H or C-OH dissociations from intermediate 3B are not possible since the dissociated O/OH species cannot bind on the Mo site which is blocked by a surface N atom (Figure 5.5). However, a concerted cleavage of C-H and O-H bonds at the third carbon of 3B producing the CHO-CHO-CH_2O* (4A) intermediate is possible which has an activation barrier of only 0.1 eV higher than the concerted C-O cleavage reaction of 3B producing allyl alcohol (4B). The concerted C-O cleavage from the intermediate 4A exhibits a much lower activation barrier of 0.31 eV which leads to the formation of acrolein (CHO-CH=CH_2, 5A). The lower activation barrier observed for the C-O cleavages of acrolein production (4A → 5A) relative to that of allyl alcohol production (3B → 4B) is due to the presence of a carbonyl group (C=O) at the terminal position of intermediate 4A which promotes the C-O cleavage at the neighboring position.

Acrolein (5A) can also be produced from concerted C-H and O-H cleavages of allyl alcohol (4B) which requires an activation barrier of only 0.1 eV. While the concerted TSs of both elementary reactions, 3B→4A and 4B→5A exhibit mainly the characteristics of C-H bond

dissociations (Figure 5.6), the O-H bond dissociation occurs without any barrier in both cases and takes place simultaneously with a C-H bond dissociation. Acrolein (5A) is converted to propanal (7A) via hydrogenation and the preferred pathway for the hydrogenation of acrolein was found to be the abstraction of an H atom by the terminal -CH_2 from the surface N (5A→6A; E_{ZPE}^{act} = 0.53 eV) followed by the abstraction of a second H atom by the middle -CH group from the surface Mo site (6A→7A; E_{ZPE}^{act} = 0.43 eV). The overall hydrogenation process (5A → 7A) is nearly thermoneutral with an exothermicity of only -0.03 eV. In another possible pathway, allyl alcohol (4B) can readsorb on the neighboring Mo site and undergo O-H bond scission to produce CH_2O-$CH{=}CH_2$* (5B). Although the activation barrier of this process is 0.09 eV higher than the acrolein formation process (4B→5A), it is thermodynamically more favored by 1.17 eV. Our NEB calculations suggested that the formation of acrolein from 5B via C-H dissociation requires an activation barrier as high as 1.7 eV and thus, we did not consider this pathway. The C-O cleavage of the intermediate 5B was found to be the next favorable process with an activation of barrier of 0.49 eV and an exothermicity of another 0.51 eV. The formation of propylene from intermediate 6B is completed by the hydrogenation of the terminal -CH_2 group (E_{ZPE}^{act} = 0.35 eV). Overall, the activation barriers of the elementary processes involved in the conversion of allyl alcohol to propanal and propylene are quite similar; however, the formation of propylene is thermodynamically more favorable by 1.59 eV than propanal because of the deposition of an additional O atom on the Mo_2N surface.

In order to correlate the computational predictions with experimental TPD observations, Figure 5.7 illustrates the Gibbs free energy profiles calculated at the experimental reaction conditions (T = 350 K and P_{gas} = 10^{-9} atm) for the minimum energy pathways of glycerol decomposition on the Mo_2N surface. The favorable pathway involves two consecutive O-H bond

cleavages followed by two concerted C-O bond scissions leading to the formation of allyl alcohol (4B). Calculated free energies further suggest that the desorption of allyl alcohol is favorable at low temperatures which agrees with the allyl alcohol desorption peak observed at 418 K (Figures 5.1 (c) & 5.2 (c)) which is lower than the desorption temperature of propanal and propylene. Our earlier work on the $Cu/Mo_2C(0001)$ catalyst model[21] suggested that glycerol undergoes three consecutive O-H bond cleavages with very low activation barriers (≤ 0.2 eV) followed by three consecutive C-O bond cleavages, leading to the preferred production of propylene on the Mo sites (Figure 5.8). Since the third O-H dissociation is blocked by the presence of surface N atoms on the Mo_2N surface, this catalyst prefers to produce allyl alcohol. Very small activation barriers associated with the initial C-H/O-H bond scissions (0.10 eV) or O-H scission (0.19 eV) of the terminal $-CH_2OH$ of allyl alcohol (4B) suggest that allyl alcohol can undergo further reaction on the Mo_2N surface to produce propanal and propylene. This correlates well with the TPD results displaying desorption peaks for propanal and propylene at higher temperatures of 476 K and 480 K, respectively (Figure 5.1), *i.e.*, it suggests that these two products are produced from allyl alcohol. Free energy profiles (Figure 5.7) further indicate that the formation of propylene from allyl alcohol is thermodynamically more favorable than the formation of propanal which could explain the higher yield of propylene (51%) observed experimentally compared to propanal (23%) as shown in Table 5.1.

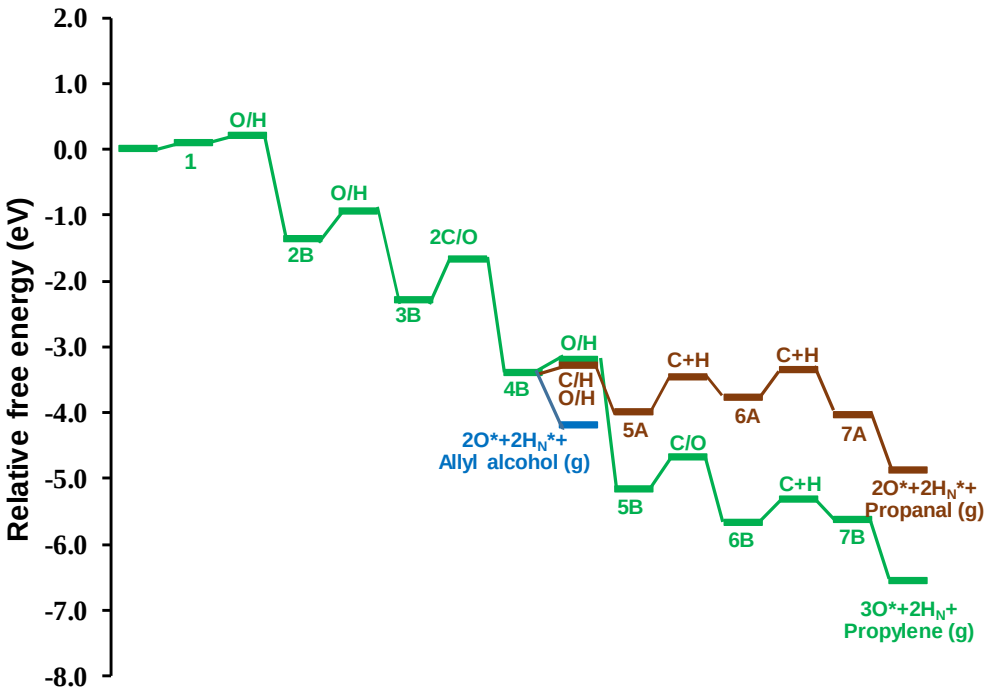

Figure 5.7. Free energy profiles for the minimum energy pathways of the glycerol decomposition on the N-terminated $Mo_2N(111)$ catalyst model (T = 350 K; $P_{gas} = 10^{-9}$ atm). All energies are with reference to the sum of the energies of gas phase glycerol and the initial catalyst model. The numbering of intermediate states corresponds to the states in Figure 5.4 and the respective bond dissociations (/) and associations (+) are shown at the transition states.

The strong exothermicity observed for both O-H and C-O bond scissions of glycerol on the Mo_2N surface implies that the dissociated O atoms can bind strongly on this surface even in the presence of neighboring N atoms. A comparison of the free energy profiles for the conversion of glycerol to propylene on the Mo sites of our $Cu/Mo_2C(0001)$ catalyst model[21] and the N-terminated $Mo_2N(111)$ surface model (Figure 5.8) indicates that the adsorption of O and H atoms on the Mo_2N surface is slightly weaker than on the Mo_2C surface. The conversion of glycerol to propylene results in deposition of 3 oxygen and 2 hydrogen atoms on the catalyst surface. Although the final state with adsorbed O and H atoms for the Mo_2N surface was found to be about 2 eV less stable

relative to the one on the Mo_2C surface, the reaction remains strongly exergonic by -6.58 eV on the Mo_2N surface. Based on DFT calculations, Dlugogorski and coworkers also observed stable O atoms adsorbed on the N-vacant Mo sites during NO reduction and H atoms adsorbed strongly on the surface N sites during H_2 dissociation on the $Mo_2N(111)$ surface.[37,45] Experimental studies performed by He *et al.* revealed the transformation of γ-Mo_2N into a $Mo_2O_xN_y$ phase in the presence of NO and this phase can be reduced back to γ-Mo_2N by H_2.[46] Thus, here we examined the removal process of adsorbed oxygen atoms on the Mo_2N surface by H_2 to form H_2O and the results are provided in Table 5.2. The calculated activation barriers and reaction energies revealed that the formation of OH from adsorbed O atoms is favored only by the direct dissociation of gas phase H_2 onto O rather than transferring H atoms adsorbed on the surface Mo or N sites. Similarly, H_2O formation preferably occurs via the disproportionation reaction of two neighboring OH rather than transferring H atoms to OH from the neighboring Mo or N sites. These results are consistent with our earlier work on the Cu/Mo_2C catalyst model[21] and also experimental reports on Mo_2C[47] and Mo_2N[46] suggesting that the adsorbed O on the Mo sites can be removed by excess H_2. Although the activation barriers calculated for the most favorable pathways of the OH (E_{ZPE}^{act} = 0.59 eV) and H_2O formation (E_{ZPE}^{act} = 0.93 eV) processes on the Mo_2N surface are about 0.2 eV higher than the corresponding processes on the Mo_2C surface, H_2O desorption from two adsorbed OH (E_{ZPE}^{rxn} = 1.22 eV calculated from reactions (6) & (7)) on the Mo_2N surface is thermodynamically favored by 0.16 eV relative to the Mo_2C surface. Thus, the oxygen removal process appears to be more facile on the Mo_2N surface.

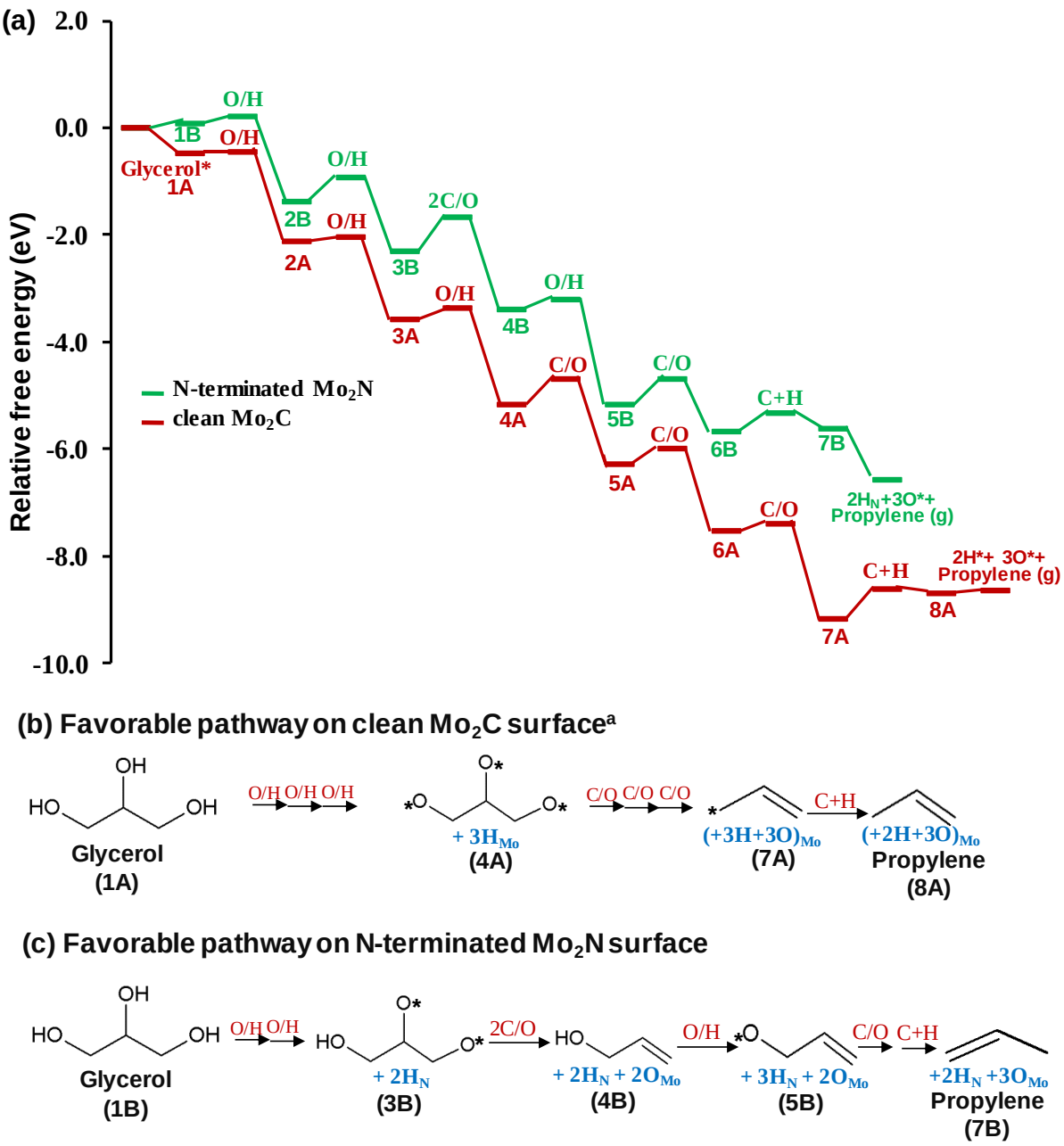

Figure 5.8. (a) Free energy profiles for the conversion of glycerol to propylene on the N-terminated Mo_2N (111) surface and on the Mo sites of the Cu/Mo_2C (0001) catalyst model[a] (T = 350 K; P_{gas} = 10^{-9} atm). All energies are with reference to the sum of the energies of gas phase glycerol and the initial catalyst model. The respective bond dissociations(/) and associations(+)

are shown at the transition states. (b)-(c) Schematic of the favorable pathways on the two surface models. ([a] see reference 21)

Table 5.2. Zero-point energy corrected reaction energies (ΔE_{ZPE}**)** and activation barriers (E_{ZPE}^{act}) calculated for the removal of adsorbed oxygen atoms from the N-terminated Mo_2N (111) catalyst model

Reaction	ΔE_{ZPE} **(eV)**	E_{ZPE}^{act} **(eV)**
N-terminated Mo_2N (111) surface[a]		
(1) $O_{Mo} + H_{Mo} \rightarrow OH_{Mo} + *_{Mo}$	0.86	1.77
(2) $O_{Mo} + H_{N} \rightarrow OH_{Mo} + *_{N}$	0.75	1.78
(3) $O_{Mo} + H_2(g) \rightarrow OH_{Mo} + H_{Mo}$	-0.58	0.59
(4) $OH_{Mo} + H_{Mo} \rightarrow H_2O_{Mo} + *_{Mo}$	1.42	2.02
(5) $OH_{Mo} + H_{N} \rightarrow H_2O_{Mo} + *_{N}$	1.15	1.27
(6) $OH_{Mo} + OH_{Mo} \rightarrow H_2O_{Mo} + O_{Mo}$	0.62	0.93
(7) $H_2O_{Mo} \rightarrow H_2O(g) + *_{Mo}$	0.60	0.60
Mo sites of the Cu/Mo_2C catalyst model[b]		
(1) $O_{Mo} + H_2(g) \rightarrow OH_{Mo} + H_{Mo}$	-0.56	0.38
(2) $OH_{Mo} + OH_{Mo} \rightarrow H_2O_{Mo} + O_{Mo}$	0.42	0.75
(3) $H_2O_{Mo} \rightarrow H_2O(g) + *_{Mo}$	0.94	0.94

[a] $*_{Mo}$ and $*_{N}$ correspond to the empty surface Mo site and surface N site, respectively on the Mo_2N surface.

[b] see Ref. 21

5.4 Conclusions

In conclusion, this work demonstrates for the first time Mo_2N as an alternative to Mo_2C for the selective HDO of glycerol. Compared to the synthesis of Mo_2C that accumulates carbon on the surface, the synthesis of Mo_2N leaves a well-defined N-terminated surface that allows for better correlation with model surface calculations. TPD experiments show that Mo_2N has similar activity to Mo_2C, with added functionality, resulting from the N modification of the surface. Both Mo_2N and Mo_2C cleave all the C-O bonds in glycerol to form propylene. In addition, Mo_2N alone can also break two C-O bonds to produce allyl alcohol and propanal, which was only achievable on the Cu/Mo_2C interface. The addition of Cu to Mo_2N shifts the reaction pathway to only one C-O bond scission to form acetol. DFT results obtained from the glycerol decomposition on the N-terminated Mo_2N (111) surface model are in good agreement with experimental observations. Comparison of these results with our earlier mechanistic study on the Mo_2C surface model provide clear evidence that the Mo_2N surface can exhibit a comparably similar activity relative to the Mo_2C surface for the glycerol HDO. Importantly, the surface N atoms of Mo_2N play a critical role in determining the mechanism and product selectivity. The activity of selective C-O bond scission of Mo_2N is also confirmed with 1,2- and 1,3-PDO, suggesting that Mo_2N can be used for the selective HDO reaction for other C3 oxygenates. Overall, this work provides insights into the controllable C-O bond scission of glycerol over Mo_2N-based catalytic materials. Such insights can also be applied to the rational catalyst design for the upgrading of other important biomass-derived oxygenates.

5.5 Acknowledgements

Reused with permission from *Lin, Z., Ammal, S. C., Denny, S. R., Rykov, S., You, K.-E., Heyden, A., Chen, J. G., Controlling Extent of C-O Bond Scission of Glycerol over Molybdenum Nitride Surfaces. (Manuscript in Preparation).* I acknowledge Dr. Saial Ammal, Kyung-Eun You, and Prof. Andreas Heyden for their work on DFT calculations and paper writing, Dr. Brian Tackett for his help with Mo_2N thin film synthesis, Steven R. Denny for thin film characterization and surface science experiments, and Dr. Sergey Rykov for the maintenance of UHV instruments.

5.6 References

(1) Chu, S.; Cui, Y.; Liu, N. The Path towards Sustainable Energy. *Nature Materials*. Nature Publishing Group December 20, 2016, pp 16–22. https://doi.org/10.1038/nmat4834.

(2) Chu, S.; Majumdar, A. Opportunities and Challenges for a Sustainable Energy Future. *Nature* **2012**, *488*. https://doi.org/10.1038/nature11475.

(3) Engelhaupt, E. Biodiesel Boom Creates Glut of Glycerin. *Environ. Sci. Technol.* **2007**, *41* (15), 5175.

(4) Pagliaro, M.; Ciriminna, R.; Kimura, H.; Rossi, M.; Della Pina, C. From Glycerol to Value-Added Products. *Angew. Chemie - Int. Ed.* **2007**, *46* (24), 4434–4440. https://doi.org/10.1002/anie.200604694.

(5) Werpy, T.; Petersen, G. *Top Value Added Chemicals from Biomass Volume I-Results of Screening for Potential Candidates from Sugars and Synthesis Gas Produced by the Staff at Pacific Northwest National Laboratory (PNNL) National Renewable Energy Laboratory (NREL) Office of Biomass*; 2004.

(6) Ripoll, V.; de Vicente, G.; Morán, B.; Rojas, A.; Segarra, S.; Montesinos, A.; Tortajada, M.; Ramón, D.; Ladero, M.; Santos, V. E. Novel Biocatalysts for Glycerol Conversion into 2,3-Butanediol. *Process Biochem.* **2016**, *51* (6), 740–748. https://doi.org/10.1016/J.PROCBIO.2016.03.006.

(7) Metsoviti, M.; Paramithiotis, S.; Drosinos, E. H.; Galiotou-Panayotou, M.; Nychas, G.-J. E.; Zeng, A.-P.; Papanikolaou, S. Screening of Bacterial Strains Capable of Converting Biodiesel-Derived Raw Glycerol into 1,3-Propanediol, 2,3-Butanediol and Ethanol. *Eng. Life Sci.* **2012**, *12* (1), 57–68. https://doi.org/10.1002/elsc.201100058.

(8) Toraya, T.; Shirakashi, T.; Kosuga, T.; Fukui, S. Substrate Specificity of Coenzyme B12-Dependent Diol Dehydrase: Glycerol as Both a Good Substrate and a Potent Inactivator. *Biochem. Biophys. Res. Commun.* **1976**, *69* (2), 475–480. https://doi.org/10.1016/0006-291X(76)90546-5.

(9) Foraget, R. G.; Foster, M. A. Glycerol Fermentation in Klebsiella Pneumoniae: Functions of the Coenzyme B12-Dependent Glycerol and Diol Dehydratases. *J. Bacteriol.* **1982**, *149* (2), 413–419.

(10) Carrettin, S.; McMorn, P.; Johnston, P.; Griffin, K.; Hutchings, G. J. Selective Oxidation of Glycerol to Glyceric Acid Using a Gold Catalyst in Aqueous Sodium Hydroxide. *Chem. Commun.* **2002**, No. 7, 696–697. https://doi.org/10.1039/b201112n.

(11) Qi, J.; Xin, L.; Chadderdon, D. J.; Qiu, Y.; Jiang, Y.; Benipal, N.; Liang, C.; Li, W. Electrocatalytic Selective Oxidation of Glycerol to Tartronate on Au/C Anode Catalysts in Anion Exchange Membrane Fuel Cells with Electricity Cogeneration. *Appl. Catal. B Environ.* **2014**, *154–155*, 360–368. https://doi.org/10.1016/j.apcatb.2014.02.040.

(12) Katryniok, B.; Paul, S.; Dumeignil, F. Recent Developments in the Field of Catalytic Dehydration of Glycerol to Acrolein. *ACS Catal.* **2013**, *3* (8), 1819–1834. https://doi.org/10.1021/cs400354p.

(13) Zhang, H.; Hu, Z.; Huang, L.; Zhang, H.; Song, K.; Wang, L.; Shi, Z.; Ma, J.; Zhuang, Y.; Shen, W.; et al. Dehydration of Glycerol to Acrolein over Hierarchical ZSM-5 Zeolites: Effects of Mesoporosity and Acidity. *ACS Catal.* **2015**, *5* (4), 2548–2558. https://doi.org/10.1021/cs5019953.

(14) Karim, A. M.; Howard, C.; Roberts, B.; Kovarik, L.; Zhang, L.; King, D. L.; Wang, Y. In Situ X-Ray Absorption Fine Structure Studies on the Effect of PH on Pt Electronic Density during Aqueous Phase Reforming of Glycerol. *ACS Catal.* **2012**, *2* (11), 2387–2394. https://doi.org/10.1021/cs3005049.

(15) Esteve-Adell, I.; Crapart, B.; Primo, A.; Serp, P.; Garcia, H. Aqueous Phase Reforming of Glycerol Using Doped Graphenes as Metal-Free Catalysts. *Green Chem.* **2017**, *19* (13), 3061–3068. https://doi.org/10.1039/C7GC01058C.

(16) Lemos, C. O. T.; Rade, L. L.; Barrozo, M. A. D. S.; Fernandes, L. D.; Cardozo-Filho, L.; Hori, C. E. Optimization of Catalytic Glycerol Etherification with Ethanol in a Continuous Reactor. *Energy and Fuels* **2017**, *31* (5), 5158–5164. https://doi.org/10.1021/acs.energyfuels.7b00194.

(17) Zhou, J.; Wang, Y.; Guo, X.; Mao, J.; Zhang, S. Etherification of Glycerol with Isobutene on Sulfonated Graphene: Reaction and Separation. *Green Chem.* **2014**, *16* (11), 4669–4679. https://doi.org/10.1039/C4GC01044B.

(18) Dodekatos, G.; Schünemann, S.; Tüysüz, H. Recent Advances in Thermo-, Photo-, and Electrocatalytic Glycerol Oxidation. *ACS Catal.* **2018**, *8* (7), 6301–6333. https://doi.org/10.1021/acscatal.8b01317.

(19) Li, B.; Wang, J.; Yuan, Y.; Ariga, H.; Takakusagi, S.; Asakura, K. Carbon Nanotube-Supported RuFe Bimetallic Nanoparticles as Efficient and Robust Catalysts for Aqueous-Phase Selective Hydrogenolysis of Glycerol to Glycols. *ACS Catal.* **2011**, *1* (11), 1521–1528. https://doi.org/10.1021/cs200386q.

(20) Huang, Z.; Cui, F.; Kang, H.; Chen, J.; Zhang, X.; Xia, C. Highly Dispersed Silica-Supported Copper Nanoparticles Prepared by Precipitation− Gel Method: A Simple but Efficient and Stable Catalyst for Glycerol Hydrogenolysis. *Chem. Mater.* **2008**, *20*, 5090–5099. https://doi.org/doi: 10.1021/cm8006233.

(21) Wan, W.; Ammal, S. C.; Lin, Z.; You, K.-E.; Heyden, A.; Chen, J. G. Controlling Reaction Pathways of Selective C–O Bond Cleavage of Glycerol. *Nat. Commun.* **2018**, *9* (1), 4612. https://doi.org/10.1038/s41467-018-07047-7.

(22) Kimmel, Y. C.; Esposito, D. V.; Birkmire, R. W.; Chen, J. G. Effect of Surface Carbon on the Hydrogen Evolution Reactivity of Tungsten Carbide (WC) and Pt-Modified WC Electrocatalysts. *Int. J. Hydrogen Energy* **2012**, *37* (4), 3019–3024. https://doi.org/10.1016/J.IJHYDENE.2011.11.079.

(23) Furimsky, E. Metal Carbides and Nitrides as Potential Catalysts for Hydroprocessing. *Applied Catalysis A: General*. February 10, 2003, pp 1–28. https://doi.org/10.1016/S0926-860X(02)00428-3.

(24) Kresse, G.; Furthmüller, J. Efficient Iterative Schemes for Ab Initio Total-Energy Calculations Using a Plane-Wave Basis Set. *Phys. Rev. B* **1996**, *54* (16), 11169–11186. https://doi.org/10.1103/PhysRevB.54.11169.

(25) Kresse, G.; Furthmüller, J. Efficiency of Ab Initio Total Energy Calculations for Metals and Semiconductors Using a Plane Wave Basis Set. *Comput. Mat. Sci.* **1996**, *6* (1), 15. https://doi.org/Doi 10.1016/0927-0256(96)00008-0.

(26) Kresse, G.; Hafner, J. Ab Initio Molecular Dynamics for Liquid Metals. *Phys. Rev. B* **1993**, *47* (1), 558–561. https://doi.org/10.1103/PhysRevB.47.558.

(27) Kresse, G.; Hafner, J. Ab-Initio Molecular-Dynamics Simulation of the Liquid-Metal Amorphous-Semiconductor Transition in Germanium. *Phys. Rev. B* **1994**, *49* (20), 14251–14269.

(28) Perdew, J. P.; Burke, K.; Ernzerhof, M. Generalized Gradient Approximation Made Simple.

Phys. Rev. Lett. **1996**, *77* (18), 3865–3868.

(29) Grimme, S.; Antony, J.; Ehrlich, S.; Krieg, H. A Consistent and Accurate Ab Initio Parametrization of Density Functional Dispersion Correction (DFT-D) for the 94 Elements H-Pu. *J. Chem. Phys.* **2010**, *132* (15). https://doi.org/Artn 154104Pmid 2042316510.1063/1.3382344.

(30) Matanovic, I.; Garzon, F. H.; Henson, N. J. Electro-Reduction of Nitrogen on Molybdenum Nitride: Structure, Energetics, and Vibrational Spectra from DFT. *Phys. Chem. Chem. Phys.* **2014**, *16* (7), 3014–3026. https://doi.org/10.1039/c3cp54559h.

(31) Bull, C. L.; Kawashima, T.; McMillan, P. F.; Machon, D.; Shebanova, O.; Dalsenberger, D.; Soignard, E.; Takayama-Muromachi, E.; Chapon, L. C. Crystal Structure and High-Pressure Properties of Gamma-Mo2N Determined by Neutron Powder Diffraction and X-Ray Diffraction. *J. Solid State Chem.* **2006**, *179* (6), 1762–1767. https://doi.org/10.1016/j.jssc.2006.03.011.

(32) Frapper, G.; Pelissier, M.; Hafner, J. CO Adsorption on Molybdenum Nitride's Gamma-Mo2N(100) Surface: Formation of N=C=O Species? A Density Functional Study. *J. Phys. Chem. B* **2000**, *104* (50), 11972–11976. https://doi.org/DOI 10.1021/jp0026179.

(33) Zhao, J. K.; Cui, C. N.; Wang, H.; Han, J. Y.; Zhu, X. L.; Ge, Q. F. Insights into the Mechanism of Ammonia Decomposition on Molybdenum Nitrides Based on DFT Studies. *J. Phys. Chem. C* **2019**, *123* (1), 554–564. https://doi.org/10.1021/acs.jpcc.8b10101.

(34) Liu, H. C.; Wang, H.; Shen, J. H.; Sun, Y.; Liu, Z. M. Preparation and Evaluation of Ammonia Decomposition Catalysts by High-Throughput Technique. *React. Kinet. Catal. Lett.* **2008**, *93* (1), 11–17. https://doi.org/10.1007/s11144-008-5155-3.

(35) Wei, Z. B. Z.; Grange, P.; Delmon, B. XPS and XRD Studies of Fresh and Sulfided Mo2N. *Appl. Surf. Sci.* **1998**, *135* (1–4), 107–114. https://doi.org/Doi 10.1016/S0169-4332(98)00267-0.

(36) Ozkan, U. S.; Zhang, L. P.; Clark, P. A. Performance and Postreaction Characterization of Gamma-Mo2N Catalysts in Simultaneous Hydrodesulfurization and Hydrodenitrogenation Reactions. *J. Catal.* **1997**, *172* (2), 294–306. https://doi.org/DOI 10.1006/jcat.1997.1873.

(37) Altarawneh, M.; Jaf, Z.; Oskierski, H.; Jiang, Z. T.; Gore, J.; Dlugogorski, B. Z. Conversion of NO into N-2 over Gamma-Mo2N. *J. Phys. Chem. C* **2016**, *120* (39), 22270–22280. https://doi.org/10.1021/acs.jpcc.6b04107.

(38) Monkhorst, H. J.; Pack, J. D. Special Points for Brillouin-Zone Integrations. *Phys. Rev. B* **1976**. https://doi.org/10.1103/PhysRevB.13.5188.

(39) Makov, G.; Payne, M. C. Periodic Boundary-Conditions in Ab-Initio Calculations. *Phys. Rev. B* **1995**, *51* (7), 4014–4022.

(40) Harris, J. Simplified Method for Calculating the Energy of Weakly Interacting Fragments. *Phys. Rev. B* **1985**, *31* (4), 1770–1779.

(41) Henkelman, G.; Uberuaga, B. P.; Jónsson, H. Climbing Image Nudged Elastic Band Method for Finding Saddle Points and Minimum Energy Paths. *J. Chem. Phys.* **2000**, *113* (22), 9901–9904. https://doi.org/10.1063/1.1329672.

(42) Olsen, R. A.; Kroes, G. J.; Henkelman, G.; Arnaldsson, A.; Jonsson, H. Comparison of Methods for Finding Saddle Points without Knowledge of the Final States. *J. Chem. Phys.* **2004**, *121* (20), 9776–9792. https://doi.org/10.1063/1.1809574.

(43) Heyden, A.; Bell, A. T.; Keil, F. J. Efficient Methods for Finding Transition States in Chemical Reactions: Comparison of Improved Dimer Method and Partitioned Rational Function Optimization Method. *J. Chem. Phys.* **2005**, *123* (22). https://doi.org/Artn 22410110.1063/1.2104507.

(44) You, K. E.; Ammal, S. C.; Lin, Z. X.; Wan, W. M.; Chen, J. G. G.; Heyden, A. Understanding the Effect of Mo2C Support on the Activity of Cu for the Hydrodeoxygenation of Glycerol. *J. Catal.* **2020**, *388*, 141–153. https://doi.org/10.1016/j.jcat.2020.05.007.

(45) Jaf, Z. N.; Altarawneh, M.; Miran, H. A.; Jiang, Z. T.; Dlugogorski, B. Z. Mechanisms Governing Selective Hydrogenation of Acetylene over Gamma-Mo2N Surfaces. *Catal. Sci. Technol.* **2017**, *7* (4), 943–960. https://doi.org/10.1039/c6cy02110g.

(46) He, H.; Dai, H. X.; Ngan, K. Y.; Au, C. T. Molybdenum Nitride for the Direct Decomposition of NO. *Catal. Letters* **2001**, *71* (3–4), 147–153. https://doi.org/Doi 10.1023/A:1009067507802.

(47) Ren, H.; Yu, W.; Salciccioli, M.; Chen, Y.; Huang, Y.; Xiong, K.; Vlachos, D. G.; Chen, J. G. Selective Hydrodeoxygenation of Biomass-Derived Oxygenates to Unsaturated Hydrocarbons Using Molybdenum Carbide Catalysts. *ChemSusChem* **2013**, *6* (5), 798–801. https://doi.org/10.1002/cssc.201200991.

Chapter 6: Experimental and Theoretical Insights into the Active Sites on WO_x/Pt(111) Surfaces for Dehydrogenation and Dehydration Reactions

6.1 Introduction

The catalytic upgrading of biomass is an effective approach for mitigating environmental issues and enhancing energy security.[1–5] Many processes have been developed to convert biomass into value-added fuels and chemicals, including gasification to produce synthesis gas, liquefaction to produce bio-oils, esterification of triglyceride to produce bio-diesel, and low-temperature catalytic conversion of biomass-derived sugars,[6] with the latter being especially promising because a variety of value-added chemical and fuels can be selectively produced.[7,8] Nonetheless, excess oxygen is often present in biomass molecules, and needs to be removed to increase the energy content and to avoid the reactivity toward byproducts.[9] The oxygenates derived from lignocellulosic biomass can be upgraded via reactions involving selective C-O bond scissions, including the hydrodeoxygenation (HDO), hydrogenolysis, and dehydration reactions. The removal of excess oxygen in these molecules produces value-added chemicals, fuels and fuel additives. The selective C-O bond scission of biomass derivatives has been studied using various types of catalysts, including bimetallics[3,10–14], and transition metal carbides- and oxide-based catalysts[15–22]. Among these catalysts, both Pt/WOx and its inverse oxide, WO_x/Pt, are particularly interesting because they have multiple distinct active sites and are active and selective for the C-O bond scission of glycerol, tetrahydrofurfuryl alcohol, and m-cresol.[23–29] For the glycerol hydrogenolysis reaction that produces 1,3-propanediol, it has been proposed that the Pt site is responsible for dissociating hydrogen, which then spills over to the WO_x site to form *in situ*

Brønsted acid sites that catalyze the selective C-O bond scission.[26,27] On the other hand, it has also been proposed that WO_x covers the Pt particles due to the strong metal-support interaction (SMSI) during the ring opening reaction of tetrahydrofurfuryl alcohol to produce 1,5-pentanediol.[28] The oxygen vacancy sites on WO_x serve as the active sites for the HDO reaction of m-cresol.[29] Even though there are many proposed mechanisms for this catalyst, the detailed reaction mechanisms on the Pt and WO_x sites are still unclear. It is therefore important to understand the nature of the Pt and WOx sites of this catalytic system, as well as the synergy between these sites to guide optimal catalyst design for specific reactions of interest.

In order to understand the reactivities and mechanisms on the Pt and WO_x sites present on the WOx/Pt catalyst, this work utilized an inverse oxide design of depositing WO_x on a Pt(111) model surface. The WO_x/Pt(111) surfaces with different WO_x coverages were prepared by chemical vapor deposition of $W(CO)_6$ and subsequent oxidation over a Pt(111) surface. Carbon monoxide (CO) was used as a probe molecule to differentiate between the Pt and WO_x sites as well as to quantify the WO_x coverage. Isopropyl alcohol (IPA) was used as a model compound to compare the adsorption and reaction over Pt(111) and WOx/Pt(111) surfaces. The reaction pathways on the Pt and WO_x sites were identified using TPD experiments by varying the WO_x coverage on Pt(111). HREELS measurements identified the reaction intermediates that were present at different temperatures. Surface functional groups associated with the active sites were confirmed by both HREELS and *in situ* IRRAS measurements. DFT calculations further revealed the binding configurations and energetics of IPA over the Pt(111) and WOx/Pt(111) surfaces to help interpret the experimental observations.

6.2 Methods

6.2.1 Experimental Methods

All TPD experiments were conducted in an ultrahigh vacuum (UHV) chamber with a base pressure of $7*10^{-10}$ Torr that has been described previously.[30] Briefly, the chamber was equipped with a UTI-100C mass spectrometer, an Auger electron spectrometer (AES), and a sputter gun. A Pt(111) single crystal was spot-welded through two tantalum posts to the manipulator for resistive heating and cooling by liquid nitrogen. A K-type thermocouple was spot-welded to the back of the crystal for temperature measurements. In a typical experiment, the Pt(111) surface was cleaned by cycles of Ne^+ sputtering and annealing at 1050 K. The surface was then titrated with oxygen at 800 K until no carbon was detected by AES. To synthesize WO_x/Pt(111), the Pt(111) surface was cooled to 130 K, and subsequently exposed to tungsten hexacarbonyl ($W(CO)_6$, 99%, Strem Chemicals) at a pressure of $1*10^{-8}$ Torr. The tungsten hexacarbonyl sample cylinder and the entire gas line were kept at 403 K to facilitate evaporation. The purity of $W(CO)_6$ was monitored using mass spectrometry. After deposition, the presence of tungsten on Pt(111) was confirmed by AES and the surface was subsequently heated to 573 K at 0.5 K/s in $5*10^{-7}$ Torr O_2 and held at 573 K for 30 minutes for oxidation. After oxidation, the surface was flashed to 950 K in the same O_2 environment to remove excess carbon, followed by reduction at 473 K in $5*10^{-8}$ Torr H_2 for 10 minutes. The surface coverages of WO_x were determined by CO TPD experiments and confirmed by the W/Pt atomic ratio from AES measurements. In a typical TPD experiment, the as-synthesized WO_x/Pt(111) surface was cooled to 150 K and exposed to a desired amount of reactant gas while facing the sample dosing tube. The surface was then heated at 3 K/s in front of the mass spectrometer while the spectra were recorded.

HREELS experiments were performed in a separate UHV chamber equipped with the same instruments as in the TPD chamber, with the addition of a HREEL spectrometer.[31] In a typical HREELS experiment, the as-synthesized WOx/Pt(111) surface was exposed to a desired amount of reactant, ramped to specific temperatures, and cooled to below 200 K before spectra were recorded.

IRRAS experiments were conducted in an instrument located at the Center for Functional Nanomaterials of Brookhaven National Laboratory, capable of operating at pressures ranging from UHV to 7.5 Torr. The system was equipped with a VERTEX 80v FT-IR spectrometer with an external MCT detector, and the entire IR beam path was in vacuum. Details of this instrument have been described previously.[32] The instrument was equipped with a polarizer that allowed taking a background with s-polarized light (parallel to the surface plane), while p-polarized light (normal to the surface plane) was used to record the sample spectra. A Pt(111) single crystal (hat-shaped, 2mm thick, with a top diameter of 8 mm, from Princeton Scientific Corporation) was initially cleaned through cycles of Ar^+ sputtering and annealing. The deposition of WO_x was carried out from a heated $W(CO)_6$ source using a directional dosing tube on a leak valve, similar to that described in the TPD experiments.

6.2.2 Computational Methods

The reverse WO_x/Pt catalyst was modeled with a W_3O_9 trimer on a 5 × 4 Pt(111) slab. The density functional theory (DFT) calculations were performed using the Perdew-Burke-Ernzerhof (PBE) exchange-correlation functional as implemented in VASP.[33–35] The core electrons were modeled using the projector augmented wave function method. The plane-wave cutoff energy was set at 520 eV, and the energy and forces were converged to within 1×10^{-5} eV and 0.01 eV/Å, respectively. Transition states were located using the climbing-image nudged elastic band (NEB)

method as implemented in the VTST[36] package, with energy and force tolerances set at 1×10^{-5} eV and 0.025 eV/Å, respectively. The k-space integrations were performed on a (3 × 2 × 1) Monkhorst-Pack[37] mesh. During geometry optimization, the bottom two layers of the Pt(111) slab were fixed at their bulk positions while the rest of the system was fully relaxed.

6.3 Results and Discussion

6.3.1 CO TPD - Probing the Pt Sites

In order to probe the relative number of Pt sites on the WO_x/Pt(111) surfaces, CO TPD experiments were conducted. Figure 6.1 shows the CO desorption from Pt(111), 0.25-, 0.5-, and above-monolayer (ML) of WO_x deposited on Pt(111). On Pt(111), a well-defined CO desorption peak centered at 427 K was observed, consistent with reported literature.[38] When Pt was modified with 0.25 ML of WO_x, the CO desorption peak shifted to a lower temperature of 344 K and the peak area decreased. When the WO_x coverage was increased to 0.5 ML, the CO desorption peak temperature shifted further to 290 K and the peak area continued to decrease. When Pt(111) was fully covered by more than one ML of WO_x, there was no CO adsorption, indicating that there were no Pt sites available. The CO TPD results indicated that CO bound to the surface less strongly as WO_x coverage increased, suggesting that the presence of WO_x weakened the CO binding on the surface, with the extent of peak temperature shift and the decrease of peak area being dependent on the coverage of WO_x. Therefore, the amount of Pt sites, and consequently the WO_x coverage on the surface could also be quantified from the peak areas of CO TPD.

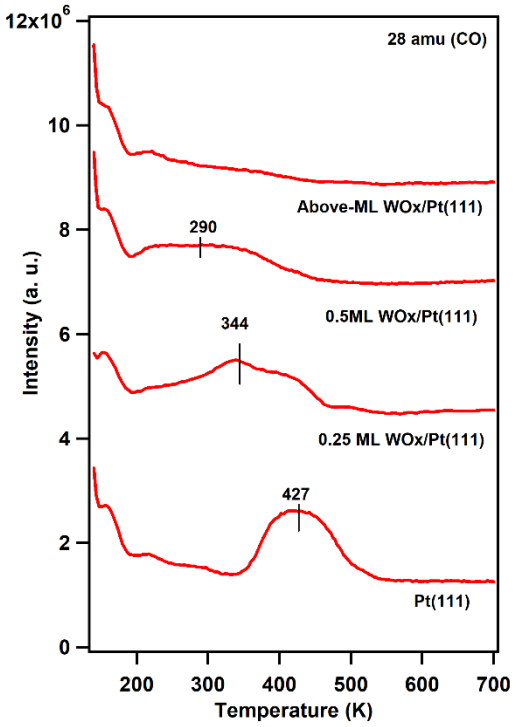

Figure 6.1. Desorption of CO after exposing the WO_x/Pt(111) surfaces with different WO_x coverages to 2 L (Langmuir, 1 L = 10^{-6} Torr*s) of CO.

6.3.2 IPA TPD - Reaction Pathways on the Pt and WO_x Sites

TPD experiments following the adsorption of IPA were performed to identify the reaction pathways over the Pt and WO_x sites present on WO_x/Pt(111). The results indicated that the Pt site was responsible for the dehydrogenation reaction, while the WO_x site catalyzed the dehydration pathway. Figure 6.2 compares the desorption of various products from the Pt(111) surfaces with different coverages of WO_x, after the surfaces were exposed to IPA at 150 K. From Figure 6.2 (a) and (b), acetone and H_2 desorbed from Pt(111) with peak temperatures at 227 K and 298 K, respectively. This showed that IPA underwent dehydrogenation on Pt(111), which was consistent

with previous studies.[39,40] The higher peak temperature of H_2 desorption, when compared to that of acetone desorption, indicated that H_2 formation was most likely desorption-limited; this was corroborated by DFT calculations as discussed later. On a WO_x/Pt(111) surface with a WO_x coverage of 0.3 ML, the acetone peak shifted to a higher temperature of 262 K, and the H_2 peak shifted to around the same temperature as that of acetone. This suggested that the addition of WO_x decreased the hydrogen binding energy on the surface. As the WO_x coverage was increased to 0.6 ML and beyond, there were no noticeable acetone and H_2 peaks, indicating that the dehydrogenation pathway was not preferred on the WO_x site. On the other hand, Figure 6.2 (c) and (d) demonstrate the desorption of propylene and water with a peak temperature of 339 K on all the surfaces modified by WO_x, suggesting that IPA underwent dehydration reaction on these surfaces. On Pt(111), there was no propylene formation, but as the WO_x coverage was increased, the propylene peak area increased, indicating that the dehydration pathway was favored on the WO_x site but not on the Pt site. The quantification results of products, based on the TPD peak areas, are summarized in Table 6.1, which shows that the amounts of dehydrogenation product (acetone) on the Pt site and the dehydration product (propylene) are comparable.

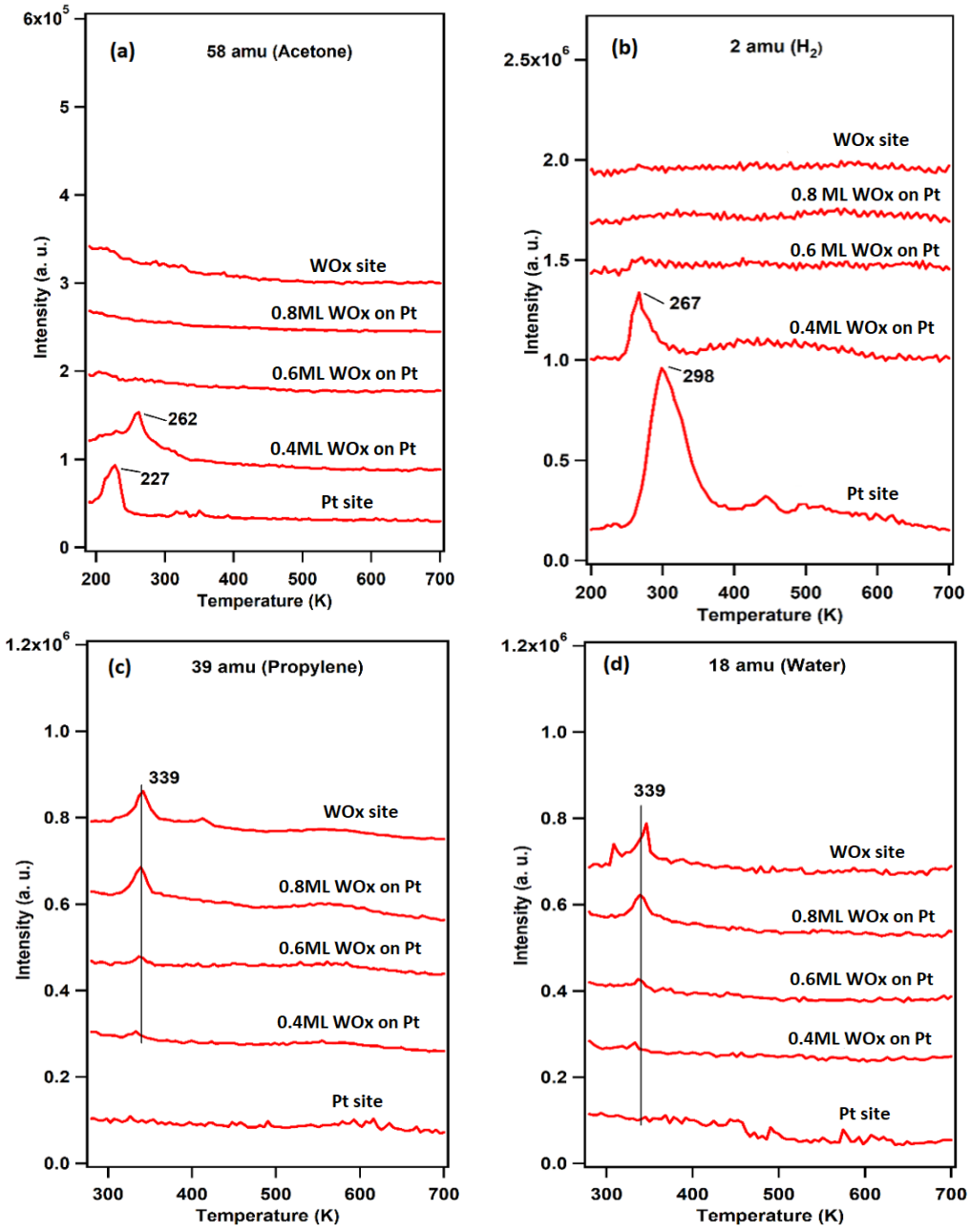

Figure 6.2. Desorption of (a) acetone (58 amu), (b) H_2 (2 amu), (c) propylene (39 amu), (d) water (18 amu) from Pt(111) surfaces modified by different coverages of WO_x after exposure of 5 L IPA.

Table 6.1. Activity (molecules per metal atom) of products from IPA TPD experiments on Pt(111) modified by different coverages of WO_x

WO_x coverage	Dehydrogenation	Dehydration
0 ML	0.011	0.000
0.3 ML	0.006	0.002
0.6 ML	0.000	0.002
0.9 ML	0.000	0.009
Above 1 ML	0.000	0.011

6.3.3 HREELS and IRRAS – IPA Reaction Intermediates and Active Site for Dehydration

Figures 6.3 (a)-(c) show the HREEL spectra after exposing IPA to Pt(111), 0.6 ML WO_x/Pt(111), and above-ML WO_x/Pt(111) surfaces at 150K. A spectrum was first recorded at (a) 150K upon IPA adsorption, and the following spectra were taken after heating the surface to (b) 200 K and (c) 400 K. The vibrational mode assignments are summarized in Table 6.2. As shown in Figure 6.3(a), at 150 K, the spectra on all three surfaces were very similar and contained the characteristic vibrational modes of IPA, indicating molecular adsorption on all surfaces at this temperature. Upon heating to 200 K (Figure 6.3(b)), a ν(C=O) mode at 1665 cm^{-1} was observed on Pt(111), suggesting the formation of acetone. The same feature was not present on the 0.6 ML WO_x/Pt(111) or above-ML WO_x/Pt(111) surfaces. In addition, adsorbed CO (1966 cm^{-1}) was only observed on Pt(111). After further heating to 400K (Figure 6.3(c)), CO was present on Pt(111). There was a smaller amount of CO on 0.6 ML WO_x/Pt(111), but none on above-ML WO_x/Pt(111).

This trend was consistent with the CO TPD experiments, in which the amount of adsorbed CO decreased with increasing WOx coverage, and that CO could not adsorb on a surface fully covered with WO_x. In addition, the Pt-C or Pt-O stretching mode at 477 cm^{-1} was observed on Pt(111) at 400K, while the W-O vibrational mode was visible at 537 cm^{-1} on 0.6 ML WO_x/Pt(111) and above-ML WO_x/Pt(111). The absence of detectable vibrational features related to the C=C bond on the WO_x/Pt(111) surfaces suggested that the desorption of the dehydration product, propylene, was reaction-limited, *i.e.*, propylene desorbed as soon as it was formed and therefore could not be detected by HREELS.

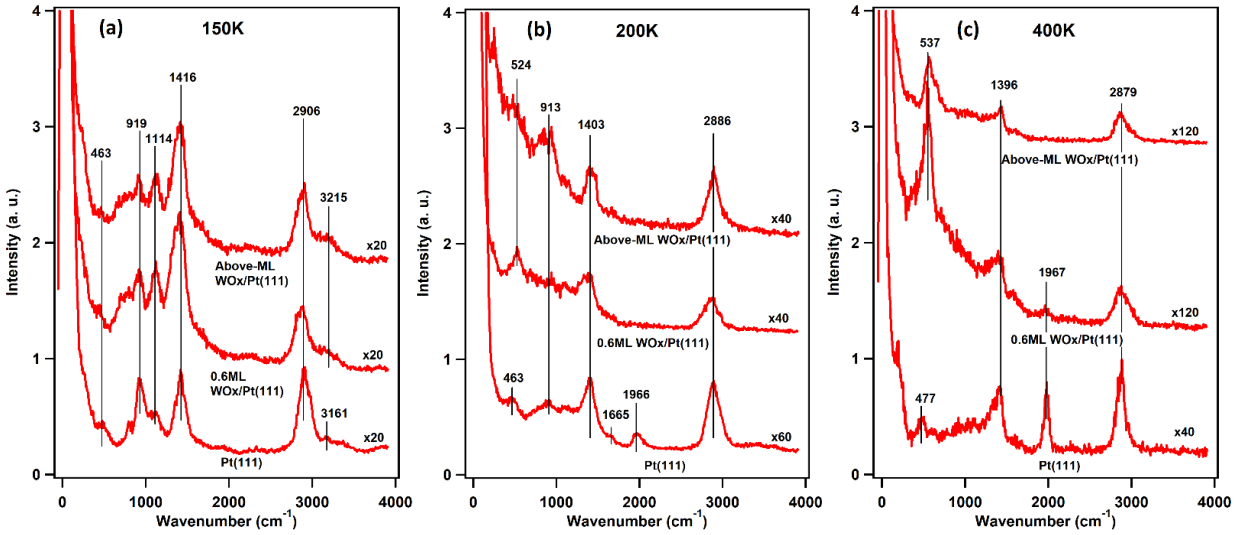

Figure 6.3. Comparison of IPA reaction pathways and intermediates on Pt(111), 0.6 ML WO_x/Pt(111), and above-ML WO_x/Pt(111) after exposing the corresponding surfaces to 5 L IPA and heating to (a) 150 K, (b) 200 K, and (c) 400 K.

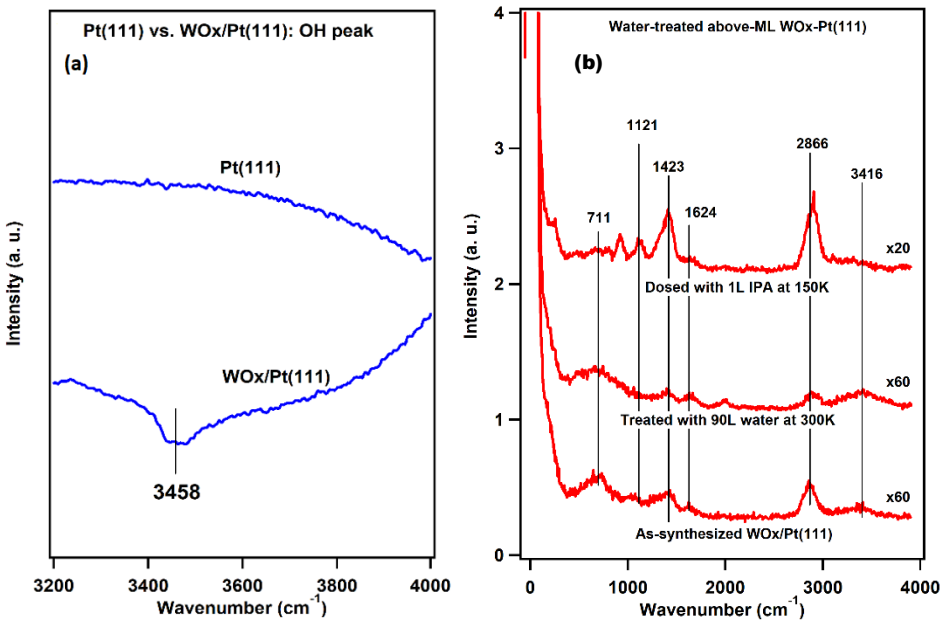

Figure 6.4. (a) IRRA spectra of the Pt(111) and as-synthesized WO_x/Pt(111) surfaces; (b) HREEL spectra of the as-synthesized WO_x/Pt(111) surface (bottom), followed by 90L water treatment at 300K (middle), and exposure to 1L IPA at 150K (top).

In order to understand the nature of the active sites, IRRAS measurements were conducted on the Pt(111) and the as-synthesized WO_x/Pt(111) surfaces. Figure 6.4 (a) compares the spectra of both surfaces in the range between 3200 cm^{-1} and 4000 cm^{-1}. The OH stretching mode was observed on WO_x/Pt(111) at 3458 cm^{-1} but not on Pt(111). The detection of the OH stretching mode suggested that the hydroxyl groups on the as-synthesized WO_x/Pt(111) surface could be involved in the dehydration reaction. In addition, HREEL spectrum of the above-ML WO_x/Pt(111) surface (bottom spectrum of Figure 6.4(b)) was also collected to compare with the IRRAS observation. Hydroxyl groups were found at 3416 cm^{-1}, which was consistent with the IRRAS measurement. To further understand the role of the surface hydroxyl groups in the IPA dehydration reaction, the as-synthesized surface was treated with 90 L of water at 300 K, followed by exposure to a lower coverage (1 L) of IPA at 150 K (middle and top spectra of Figure 6.4(b)). After the

water treatment, more hydroxyl groups were present on the surface as evidenced by the increase of the ν(OH) mode at 3416 cm^{-1}. Upon the adsorption of IPA, the intensity of the ν(OH) mode decreased significantly, suggesting that IPA had reacted with the hydroxyl groups. Therefore, it was likely that the surface hydroxyl groups participated in the IPA dehydration reaction to produce propylene. Attempts were also made to generate *in situ* hydroxyl groups by treating a sub-ML WO_x/Pt(111) surface with hydrogen, but hydroxyl groups could not be formed effectively under UHV conditions. Nonetheless, DFT calculations were performed to predict the activation barriers of *in situ* hydroxyl group formation by hydrogen spillover to further understand its role in the reaction of IPA over WO_x/Pt(111) surfaces.

Table 6.2. Vibrational mode assignments of IPA

	Pt(111)	**WO_x/Pt(111)**	**Liquid IR[a]**
ν(Pt-C), ν(Pt-O)	**463**		
ν(W-O)		**537**	
ρ(CH_3)	**919**	**919**	**921**
ρ(CH_3)	**1114**	**1114**	**1130**
δ(CH_3)	**1416**	**1416**	**1470**
ν(C=O)	**1665**		
ν(CH)	**2906**	**2906**	**2894**
ν(OH)	**3161**	**3215**	**3350**

Abbreviation: ρ – Wagging, δ – Deformation, ν – Stretching

a. From Ref.[39]

6.3.4 DFT Calculations of IPA Dehydrogenation and Dehydration

DFT calculations were performed to further understand the catalytic activity of Pt(111) toward IPA dehydrogenation and of 1ML WO_x/Pt(111) toward IPA dehydration. On Pt(111), dehydrogenation of IPA to acetone happened facilely (Figure 6.5). IPA underwent physisorption on the Pt(111) surface, coordinating to an atop site through its hydroxyl group. The first step of the dehydrogenation reaction was the breaking of the O-H bond and required 0.9 eV of intrinsic activation energy. The isopropoxy intermediate was quite unstable and thus underwent almost instantaneous elimination of its α-hydrogen to form acetone (intrinsic barrier of 0.02 eV). Product release seemed to be rate-controlling: although acetone desorbed readily, requiring *ca*. 0.5 eV of energy, H_2 recombination and desorption required an additional 0.8 eV of activation. This was consistent with the TPD observations described earlier.

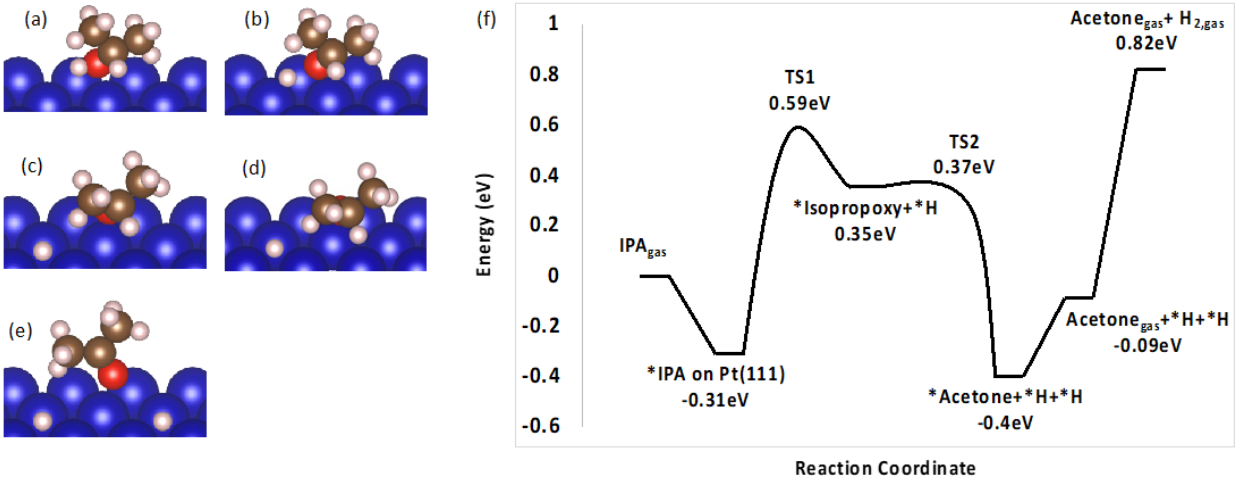

Figure 6.5. IPA dehydrogenation on Pt(111). (a) IPA bound to Pt(111); (b) O-H bond breaking transition state (TS1); (c) Isopropoxy and atomic hydrogen species resulting from O-H bond breaking.; (d) Isopropoxy C_α-H bond breaking transition state (TS2); (e): Surface acetone and *H atoms. (f) Energy profile along the reaction pathway; note that acetone desorption was facile

whereas H_2 recombination and desorption was energetically demanding. (Color code: blue, Pt; grey, W; red, O; white, H; brown, C.)

As previously discussed, the detection of the OH stretching mode in IRRAS and HREELS measurements suggested the presence of hydroxyl groups on the as-synthesized WO_x/Pt(111). The activity of these OH groups for alcohol dehydration was investigated by performing DFT calculations on the ML WO_3/Pt(111) surface. The DFT results showed that they were acidic enough to catalyze the dehydration of IPA to propylene via a concerted, single-transition state mechanism that required 1.47 eV of intrinsic activation energy (Figure 6.6). As the system passed through the single transition state, the IPA hydroxyl accepted a proton from the surface OH group to which it was coordinated. This activated the breaking of the IPA C-O bond while the incipient water molecule mediated the β-elimination by accepting a proton from the C_β-carbon and donating a different proton back to the active site of the catalyst. In light of this, the increase in the propylene yield with the coverage of WO_x in the TPD results should be attributed to Brønsted acid sites present on the surface of the oxide.

In the absence of H_2 and of the hydrogen-spillover mechanism to generate hydroxyl sites on the WO_x/Pt(111) surface, the possibility of Brønsted site formation by dissociative adsorption of water was investigated. The DFT calculations showed that this was a very efficient mechanism as it required only 0.25 eV of activation energy. This result was consistent with the HREELS observation that hydroxyl groups that were active for IPA dehydration could be generated with water treatment under UHV conditions.

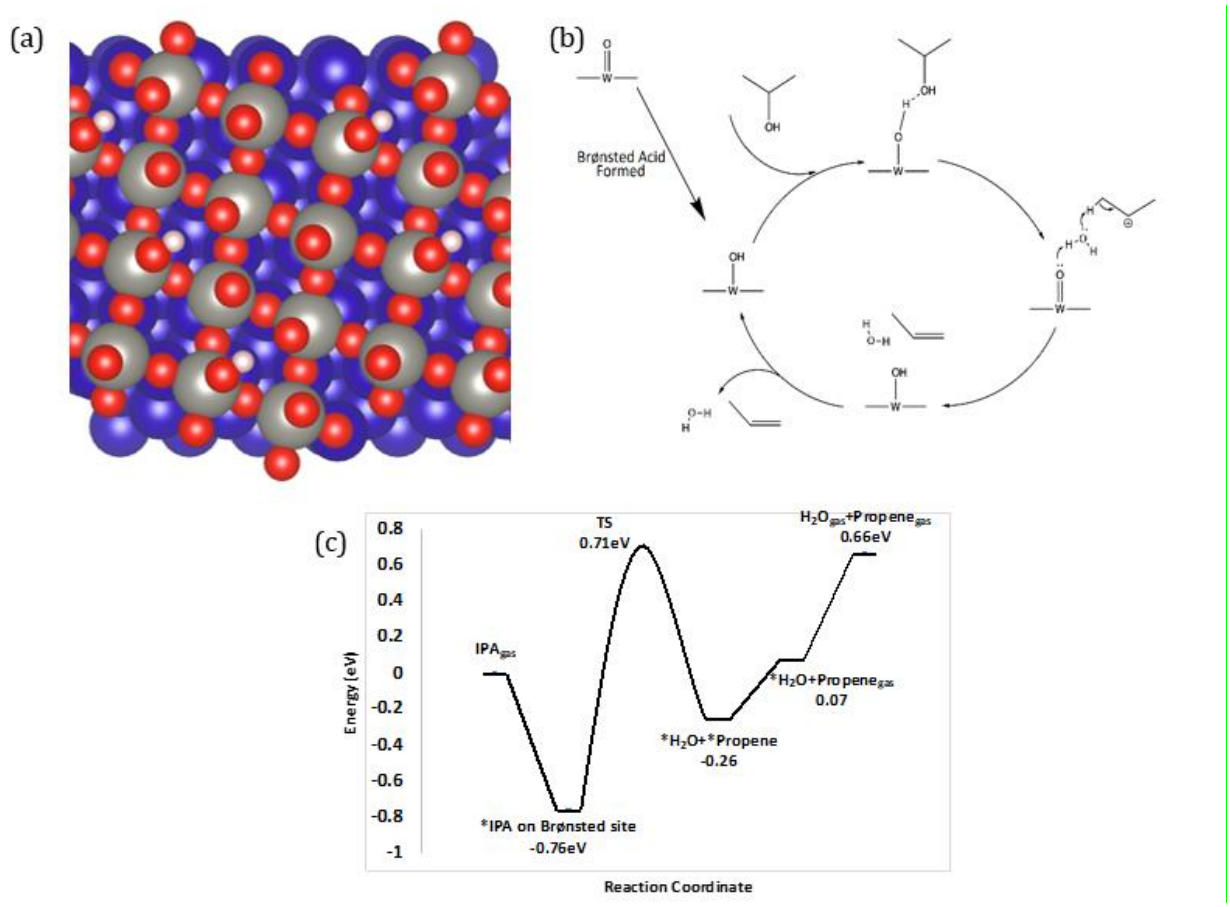

Figure 6.6. IPA dehydration on 1 ML WO_x/Pt (111). (a) Model surface; (b) Reaction mechanism; (c) Energy profile. (Color code: blue, Pt; grey, W; red, O; white, H.)

To understand the catalytic activity of sub-monolayer WO_x/Pt(111) for dehydration and to investigate the mechanism of hydroxyl group formation, a W_3O_9 cluster was deposited and relaxed on the Pt(111) surface. The DFT calculations showed that hydrogen spillover from the Pt(111) surface onto the WO_x cluster was facile and led to the formation of Brønsted acid sites. The Brønsted site formation energy was in the range between -0.5 and -0.3 eV, depending on the O-site in the cluster (see Table 6.3).

As shown in Figure 6.7, these Brønsted sites were active enough to catalyze IPA dehydration to propylene via the same single-transition state, concerted mechanism described earlier for the ML WO_x/Pt(111) surface. The reaction required activation energies in the range

between 1.23 and 1.55 eV, depending on the location of the Brønsted site (see Table 6.3). The most active site for dehydration (intrinsic barrier of 1.23 eV) corresponded to the proton that was the least strongly bound (site formation energy of -0.3 eV).

Table 6.3. List of investigated Brønsted acid sites on W_3O_9/Pt(111) formed by hydrogen spillover and corresponding energies of formation and of activation of IPA dehydration. (Atom labelling according to Figure 6.7(a).)

Acid site	Brønsted site formation energy (eV)	IPA dehydration barrier (eV)
W_3O_9H1_W1_up	-0.45	1.40
$W_3O_9H_1$_W1_down	-0.47	1.50
$W_3O_9H_1$_W2_down	-0.34	1.43
$W_3O_9H_1$_W2_up	-0.30	1.23
$W_3O_9H_1$_W3	-0.54	1.55

In addition to the hydrogen spillover mechanism, DFT calculations revealed facile Brønsted site formation by H_2O dissociative adsorption on the W_3O_9 cluster, with a reaction energy of -0.11 eV and an activation energy of 0.25 eV, similar to the ML WO_x/Pt(111) model. This mechanism created two neighboring OH sites, one on the undercoordinated W3 site and one on the "O up" of the W2 site (Figure 6.7 (a)). Interestingly, these water-dissociation Brønsted sites seemed to be less active than the hydrogen-spillover sites as the IPA dehydration required 1.72 eV of activation energy, namely *ca*. 0.5 eV higher than on the most active hydrogen-spillover site. One should note that they were also 0.3 eV less active than the respective water-dissociation sites

on the ML WO_x/Pt(111) model, presumably because they were more dispersed in the latter and thus not strongly interacting with one another.

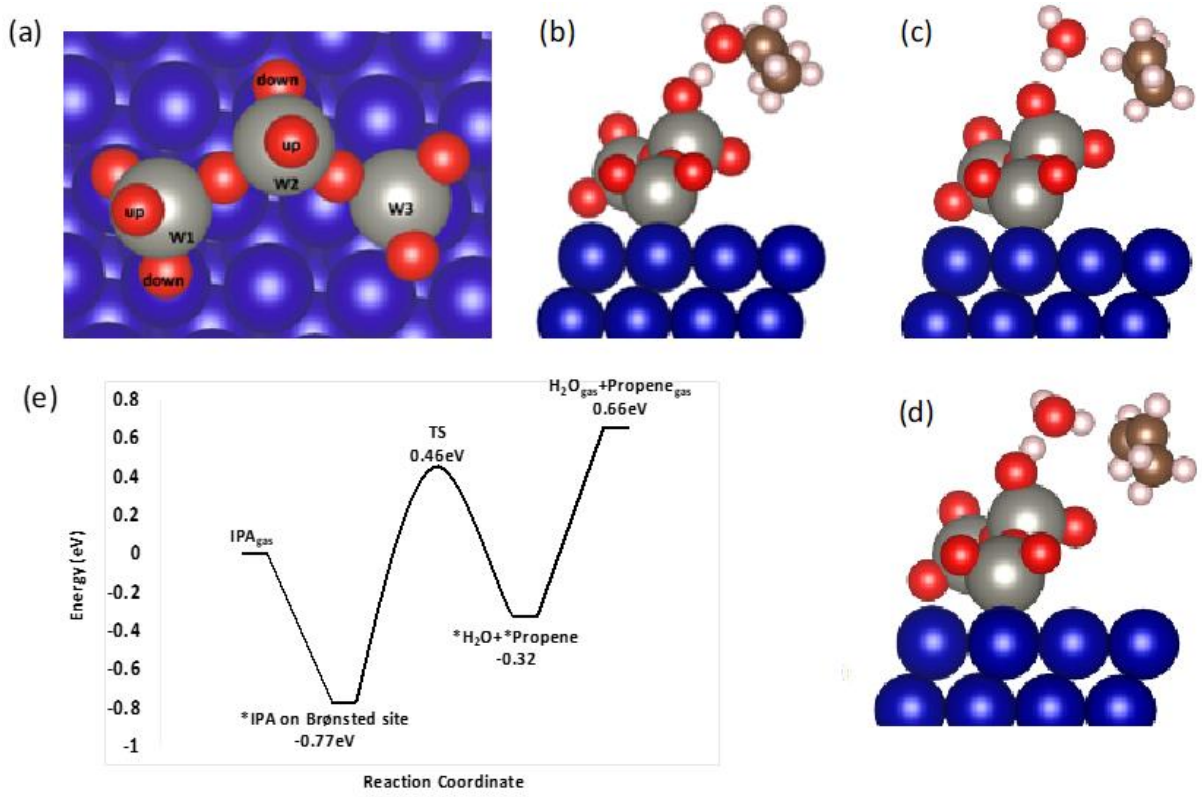

Figure 6.7. IPA dehydration on a W_3O_9 cluster modelling low oxide coverage on Pt(111). (a) W_3O_9 cluster model on Pt(111) prior to OH formation; (b) IPA coordinated to oxide hydroxyl group formed on O atom marked "up" and which was bonded to atom marked W2; (c) Dehydration transition state; (d) Propylene and water formation; (e) Energy profile along the reaction pathway. (Color code: blue, Pt; grey, W; red, O; white, H: brown, C.)

6.4 Conclusions

In conclusion, TPD, HREELS, and IRRAS experiments have been performed to investigate the active sites on the Pt(111) and WO_x/Pt(111) surfaces using CO and IPA as probe molecules. The WO_x coverages were determined by CO TPD experiments. The IPA TPD experiments showed

that the dehydrogenation reaction was preferred on the Pt site, producing acetone and hydrogen. On the WO_x site, the dehydration reaction of IPA was favored, with propylene and water being produced. HREELS experiments identified the reaction intermediates on both the Pt and WO_x sites. HREELS and IRRAS measurements also confirmed the presence of hydroxyl groups on the WO_x site, which should likely be the active sites for IPA dehydration. DFT calculations revealed detailed reaction mechanisms and energetics of both IPA dehydrogenation over Pt(111) and dehydration over WO_x/Pt(111) surfaces. Based on the understanding of both active sites, the activation barriers of *in situ* hydroxyl group formation, from both hydrogen-spillover and water dissociation, on the WO_x/Pt(111) interface were also calculated using DFT. The hydroxyl group with the least strongly bound proton (site formation energy of -0.3 eV) was predicted to be the most active site for dehydration. This work reveals the nature of the different active sites on the WO_x/Pt(111) model surface, and in turn provides insights into the design of relevant metal/metal oxide catalytic systems to control the dehydrogenation and dehydration of biomass-derived oxygenates.

6.5 Acknowledgements

Reused with permission from *Lin, Z., Liu, S., Denny, S. R., Porter, W. N., Caratzoulas, S., Boscoboinik, J. A., Vlachos, D. G., Chen, J. G., Experimental and Theoretical Insights into The Active Sites on WO_x/Pt(111) Surfaces for Dehydrogenation and Dehydration Reactions. (Manuscript under Review)*. I acknowledge Steven R. Denny and William N. Porter for the assistance with surface science experiments, Dr. Shizhong Liu, Dr. Stavros Caratzoulas, and Prof. Dionisios G. Vlachos for performing the DFT calculations and writing the computation section, and Dr. J. Anibal Boscoboinik for the help with IRRAS experiments.

6.6 References

(1) Chheda, J. N.; Huber, G. W.; Dumesic, J. A. Liquid-Phase Catalytic Processing of Biomass-Derived Oxygenated Hydrocarbons to Fuels and Chemicals. *Angew. Chemie - Int. Ed.* **2007**, *46* (38), 7164–7183. https://doi.org/10.1002/anie.200604274.

(2) Huber, G. W.; Iborra, S.; Corma, A. Synthesis of Transportation Fuels from Biomass: Chemistry, Catalysts, and Engineering. *Chem. Rev.* **2006**, *106* (9), 4044–4098. https://doi.org/10.1021/cr068360d.

(3) Jiang, Z.; Wan, W.; Lin, Z.; Xie, J.; Chen, J. G. Understanding the Role of M/Pt(111) (M=Fe, Co, Ni, Cu) Bimetallic Surfaces for Selective Hydrodeoxygenation of Furfural. *ACS Catal.* **2017**, *7* (9), 5758–5765. https://doi.org/10.1021/acscatal.7b01682.

(4) Robinson, A. M.; Hensley, J. E.; Will Medlin, J. Bifunctional Catalysts for Upgrading of Biomass-Derived Oxygenates: A Review. *ACS Catal.* **2016**, *6* (8), 5026–5043. https://doi.org/10.1021/acscatal.6b00923.

(5) Lin, Z.; Chen, R.; Qu, Z.; Chen, J. G. Hydrodeoxygenation of Biomass-Derived Oxygenates over Metal Carbides: From Model Surfaces to Powder Catalysts. *Green Chem.* **2018**, *20* (12), 2679–2696. https://doi.org/10.1039/C8GC00239H.

(6) Chheda, J. N.; Dumesic, J. A. An Overview of Dehydration, Aldol-Condensation and Hydrogenation Processes for Production of Liquid Alkanes from Biomass-Derived Carbohydrates. *Catal. Today* **2007**, *123* (1–4), 59–70. https://doi.org/10.1016/j.cattod.2006.12.006.

(7) Lin, Y. C.; Huber, G. W. The Critical Role of Heterogeneous Catalysis in Lignocellulosic Biomass Conversion. *Energy Environ. Sci.* **2009**, *2* (1), 68–80. https://doi.org/10.1039/b814955k.

(8) Lin, L.; Cunshan, Z.; Vittayapadung, S.; Xiangqian, S.; Mingdong, D. Opportunities and Challenges for Biodiesel Fuel. *Appl. Energy* **2011**, *88* (4), 1020–1031. https://doi.org/10.1016/j.apenergy.2010.09.029.

(9) Xiong, K.; Yu, W.; Vlachos, D. G.; Chen, J. G. Reaction Pathways of Biomass-Derived Oxygenates over Metals and Carbides: From Model Surfaces to Supported Catalysts. *ChemCatChem* **2015**, *7* (9), 1402–1421. https://doi.org/10.1002/cctc.201403067.

(10) Wang, H.; Li, X.; Lan, X.; Wang, T. Supported Ultrafine NiCo Bimetallic Alloy Nanoparticles Derived from Bimetal-Organic Frameworks: A Highly Active Catalyst for Furfuryl Alcohol Hydrogenation. *ACS Catal.* **2018**, *8* (3), 2121–2128. https://doi.org/10.1021/acscatal.7b03795.

(11) Wan, W.; Jenness, G. R.; Xiong, K.; Vlachos, D. G.; Chen, J. G. Ring-Opening Reaction of Furfural and Tetrahydrofurfuryl Alcohol on Hydrogen-Predosed Iridium(111) and Cobalt/Iridium(111) Surfaces. *ChemCatChem* **2017**, *9* (9), 1701–1707. https://doi.org/10.1002/cctc.201601646.

(12) Robinson, A.; Ferguson, G. A.; Gallagher, J. R.; Cheah, S.; Beckham, G. T.; Schaidle, J. A.; Hensley, J. E.; Medlin, J. W. Enhanced Hydrodeoxygenation of M-Cresol over Bimetallic Pt-Mo Catalysts through an Oxophilic Metal-Induced Tautomerization Pathway. *ACS Catal.* **2016**, *6* (7), 4356–4368. https://doi.org/10.1021/acscatal.6b01131.

(13) Yang, F.; Liu, D.; Wang, H.; Liu, X.; Han, J.; Ge, Q.; Zhu, X. Geometric and Electronic Effects of Bimetallic Ni–Re Catalysts for Selective Deoxygenation of m-Cresol to Toluene. *J. Catal.* **2017**, *349*, 84–97. https://doi.org/10.1016/j.jcat.2017.01.001.

(14) Liu, X.; An, W.; Turner, C. H.; Resasco, D. E. Hydrodeoxygenation of M-Cresol over Bimetallic NiFe Alloys: Kinetics and Thermodynamics Insight into Reaction Mechanism. *J. Catal.* **2018**, *359*, 272–286. https://doi.org/10.1016/j.jcat.2018.01.006.

(15) Chen, C. J.; Bhan, A. Mo_2C Modification by CO_2,H_2O, and O_2: Effects of Oxygen Content and Oxygen Source on Rates and Selectivity of M-Cresol Hydrodeoxygenation. *ACS Catal.* **2017**, *7* (2), 1113–1122. https://doi.org/10.1021/acscatal.6b02762.

(16) Chen, C. J.; Lee, W. S.; Bhan, A. Mo_2C Catalyzed Vapor Phase Hydrodeoxygenation of Lignin-Derived Phenolic Compound Mixtures to Aromatics under Ambient Pressure. *Appl. Catal. A Gen.* **2016**, *510*, 42–48. https://doi.org/10.1016/j.apcata.2015.10.043.

(17) Wan, W.; Ammal, S. C.; Lin, Z.; You, K.-E.; Heyden, A.; Chen, J. G. Controlling Reaction Pathways of Selective C–O Bond Cleavage of Glycerol. *Nat. Commun.* **2018**, *9* (1), 4612. https://doi.org/10.1038/s41467-018-07047-7.

(18) Lin, Z.; Wan, W.; Chen, J. G. 1,2-Propanediol as a Surrogate Molecule of Glycerol for Mechanistic Studies of Selective Hydrodeoxygenation Reactions over Mo_2C and Cu/Mo_2C Surfaces. *ACS Sustain. Chem. Eng.* **2019**, *7*, 8077–8082. https://doi.org/10.1021/acssuschemeng.9b01051.

(19) Shetty, M.; Murugappan, K.; Prasomsri, T.; Green, W. H.; Román-Leshkov, Y. Reactivity and Stability Investigation of Supported Molybdenum Oxide Catalysts for the Hydrodeoxygenation (HDO) of m-Cresol. *J. Catal.* **2015**, *331*, 86–97. https://doi.org/10.1016/j.jcat.2015.07.034.

(20) Sirous-Rezaei, P.; Jae, J.; Ha, J.-M.; Ko, C. H.; Kim, J. M.; Jeon, J.-K.; Park, Y.-K. Mild Hydrodeoxygenation of Phenolic Lignin Model Compounds over a $FeReO_x/ZrO_2$ Catalyst: Zirconia and Rhenium Oxide as Efficient Dehydration Promoters. *Green Chem.* **2018**, *20* (7), 1472–1483. https://doi.org/10.1039/c7gc03823b.

(21) Gonçalves, V. O. O.; Ciotonea, C.; Arrii-Clacens, S.; Guignard, N.; Roudaut, C.; Rousseau, J.; Clacens, J. M.; Royer, S.; Richard, F. Effect of the Support on the Hydrodeoxygenation of M-Cresol over Molybdenum Oxide Based Catalysts. *Appl. Catal. B Environ.* **2017**, *214*, 57–66. https://doi.org/10.1016/j.apcatb.2017.05.003.

(22) Wang, F.; Dubois, J. L.; Ueda, W. Catalytic Dehydration of Glycerol over Vanadium Phosphate Oxides in the Presence of Molecular Oxygen. *J. Catal.* **2009**, *268* (2), 260–267. https://doi.org/10.1016/j.jcat.2009.09.024.

(23) Qin, L.-Z.; Song, M.-J.; Chen, C.-L. Aqueous-Phase Deoxygenation of Glycerol to 1,3-Propanediol over $Pt/WO_3/ZrO_2$ Catalysts in a Fixed-Bed Reactor. *Green Chem.* **2010**, *12*, 1466–1472. https://doi.org/10.1039/c0gc00005a.

(24) Zhu, S.; Gao, X.; Zhu, Y.; Li, Y. Promoting Effect of WO_x on Selective Hydrogenolysis of Glycerol to 1,3-Propanediol over Bifunctional $Pt\text{-}WO_x/Al_2O_3$ Catalysts. *J. Mol. Catal. A Chem.* **2015**, *398*, 391–398. https://doi.org/10.1016/j.molcata.2014.12.021.

(25) Zhao, X.; Wang, J.; Yang, M.; Lei, N.; Li, L.; Hou, B.; Miao, S.; Pan, X.; Wang, A.; Zhang, T. Selective Hydrogenolysis of Glycerol to 1,3-Propanediol: Manipulating the Frustrated Lewis Pairs by Introducing Gold to Pt/WO_X. *ChemSusChem* **2017**, *10*, 819–824. https://doi.org/10.1002/cssc.201601503.

(26) Wang, J.; Zhao, X.; Lei, N.; Li, L.; Zhang, L.; Xu, S.; Miao, S.; Pan, X.; Wang, A.; Zhang, T. Hydrogenolysis of Glycerol to 1,3-Propanediol under Low Hydrogen Pressure over WO_x-Supported Single/Pseudo-Single Atom Pt Catalyst. *ChemSusChem* **2016**, *9*, 784–790. https://doi.org/10.1002/cssc.201501506.

(27) Lei, N.; Zhao, X.; Hou, B.; Yang, M.; Zhou, M.; Liu, F.; Wang, A.; Zhang, T. Effective Hydrogenolysis of Glycerol to 1,3-Propanediol over Metal-Acid Concerted $Pt/WO_x/Al_2O_3$ Catalysts. *ChemCatChem* **2019**, *11* (16), 3903–3912. https://doi.org/10.1002/cctc.201900689.

(28) Wang, C.; Lee, J. D.; Ji, Y.; Onn, T. M.; Luo, J.; Murray, C. B.; Gorte, R. J. A Study of Tetrahydrofurfuryl Alcohol to 1,5-Pentanediol Over $Pt–WO_x/C$. *Catal. Letters* **2018**, *148* (4), 1047–1054. https://doi.org/10.1007/s10562-018-2323-6.

(29) Wang, C.; Mironenko, A. V; Raizada, A.; Chen, T.; Mao, X.; Padmanabhan, A.; Vlachos, D. G.; Gorte, R. J.; Vohs, J. M. Mechanistic Study of the Direct Hydrodeoxygenation of M-Cresol over WO_x-Decorated Pt/C Catalysts. *ACS Catal.* **2018**, *8*, 7749–7759. https://doi.org/10.1021/acscatal.8b01746.

(30) Hwu, H. H.; Chen, J. G. Reactions of Methanol and Water over Carbide-Modified Mo(110). *Surf. Sci.* **2003**, *536* (1–3), 75–87. https://doi.org/10.1016/S0039-6028(03)00607-1.

(31) Frühberger, B.; Chen, J. G. Reaction of Ethylene with Clean and Carbide-Modified Mo(110): Converting Surface Reactivities of Molybdenum to Pt-Group Metals. *J. Am. Chem. Soc.* **1996**, *118* (46), 11599–11609. https://doi.org/10.1021/ja960656l.

(32) Eads, C. N.; Zhong, J. Q.; Kim, D.; Akter, N.; Chen, Z.; Norton, A. M.; Lee, V.; Kelber, J. A.; Tsapatsis, M.; Boscoboinik, J. A.; et al. Multi-Modal Surface Analysis of Porous Films under Operando Conditions. *AIP Adv.* **2020**, *10* (8), 085109. https://doi.org/10.1063/5.0006220.

(33) Kresse, G.; Hafner, J. Ab Initio Molecular Dynamics for Open-Shell Transition Metals. *Phys. Rev. B* **1993**, *48* (17), 13115–13118. https://doi.org/10.1103/PhysRevB.48.13115.

(34) Kresse, G.; Furthmüller, J. Efficiency of Ab-Initio Total Energy Calculations for Metals and Semiconductors Using a Plane-Wave Basis Set. *Comput. Mater. Sci.* **1996**, *6* (1), 15–50. https://doi.org/10.1016/0927-0256(96)00008-0.

(35) Kresse, G.; Furthmüller, J. Efficient Iterative Schemes for Ab Initio Total-Energy Calculations Using a Plane-Wave Basis Set. *Phys. Rev. B* **1996**, *54* (16), 11169–11186. https://doi.org/10.1103/PhysRevB.54.11169.

(36) Henkelman, G.; Uberuaga, B. P.; Jónsson, H. Climbing Image Nudged Elastic Band Method for Finding Saddle Points and Minimum Energy Paths. *J. Chem. Phys.* **2000**, *113* (22), 9901–9904. https://doi.org/10.1063/1.1329672.

(37) Monkhorst, H. J.; Pack, J. D. Special Points for Brillouin-Zone Integrations. *Phys. Rev. B* **1976**, *13*, 5188. https://doi.org/10.1103/PhysRevB.13.5188.

(38) Hopster, H.; Ibach, H. Adsorption of CO on Pt(111) and Pt 6(111) × (111) Studied by High Resolution Electron Energy Loss Spectroscopy and Thermal Desorption Spectroscopy. *Surf. Sci.* **1978**, *77* (1), 109–117. https://doi.org/10.1016/0039-6028(78)90164-4.

(39) Vannice, M. A.; Erley, W.; Ibach, H. A RAIRS and HREELS Study of Isopropyl Alcohol on Pt(111). *Surf. Sci.* **1991**, *254* (1–3), 12–20. https://doi.org/10.1016/0039-6028(91)90633-4.

(40) Vannice, M. A.; Erley, W.; Ibach, H. A RAIRS and HREELS Study of Acetone on Pt(111). *Surf. Sci.* **1991**, *254* (1–3), 1–11. https://doi.org/10.1016/0039-6028(91)90632-3.

Chapter 7: Conclusions and Future Directions

7.1 Conclusions

In this dissertation, the active sites and reaction mechanisms of linear-chain and ring-containing biomass-derived oxygenates over transition metal carbide, nitride, and oxide surfaces are compared in the context of selective C-O/C=O bond scission. The relevant surface preparation methods, surface science experimental techniques, as well as first-principles DFT calculations are reviewed. While carbides and nitrides process metal-like sites that catalyze the direct C-O/C=O bond scissions, it is the acid sites on oxides that facilitate the dehydration reaction to achieve oxygen removal. Different strategies for modifying the reaction pathways and stabilizing TMC and TMN surfaces have been demonstrated. Mo_2C has been known to be highly active and selective toward C-O/C=O bond dissociation, but it deactivates rapidly due to the strong interaction with oxygen. Chapter 3 demonstrates that Co-modifiers reduce the oxygen binding energy of Mo_2C to a proper extent and thereby enhance the stability of the surface during the HDO reaction of a ring-containing molecule, furfural. For the HDO reaction of a linear-chain molecule, glycerol, the selective scission of specific numbers of C-O bonds remains a challenge. Glycerol has been shown to undergo total C-O bond scission over Mo_2C, again due to the strong interaction between the oxygen atoms in glycerol with Mo_2C. In chapter 4, it is shown that Cu-modifications enable the selective C-O bond scission of specific numbers of C-O bonds of glycerol, and the product selectivity can be tuned by varying the Cu coverage. Despite the promising results, vapor-phase mechanistic studies of glycerol are difficult because of the low vapor pressure of glycerol. In order to overcome this challenge, a surrogate molecule that has a similar chemical structure to that of glycerol but with a higher vapor pressure, 1,2-propanediol, is identified as an alternative to glycerol for ambient pressure vapor-phase mechanistic studies with industrial-relevant powder

catalysts. While Chapters 3 and 4 demonstrate the feasibility of enhancing the stability and tunning the selectivity of Mo_2C using metal modifiers, the C-O bond scission reactions of relevant biomass molecules over TMCs, TMNs, and TMOs are compared in Chapters 4 and 5. The active sites and reaction mechanisms between carbides and nitrides are compared in Chapter 5. The same glycerol HDO reaction is performed on Mo_2N. It is found that glycerol also undergoes complete HDO to form propylene on Mo_2N. In addition, products with two C-O bond scissions, ally alcohol and propanal, are also formed on Mo_2N. DFT calculations reveal that surface N atoms block some of the Mo sites, which facilitates the selective C-O bond scissions. These results suggest that by changing the interstitial atoms from carbon to nitrogen, the surface structure and the extent of interaction with adsorbates change, which leads to a change in product selectivity. As shown in Chapter 6, the active sites and reaction mechanisms for the oxygen removal of biomass-derived oxygenates over oxides (WO_x/Pt(111)) are very different from those for carbide and nitrides. Acid sites are the main active sites on oxide surfaces, and the reaction follows the dehydration mechanism instead of direct C-O/C=O bond scission. DFT calculations also provide insights into the *in situ* generation of acid sites using water and hydrogen, and the synergistic effect between the oxide overlayer and the metal substrate. Overall, this dissertation summarizes the similarities and differences among TMC, TMN, and TMO surfaces for the catalytic upgrading of biomass-derived oxygenates, and provides useful information for rational catalyst design depending on the application.

7.2 Future Directions

Based on the knowledge on TMCs/TMNs/TMOs provided in this dissertation, it is possible to synthesize corresponding powder catalysts and conduct further reactor studies. As shown in Chapter 6, the strong interaction between the metal and support of an inverse oxide catalyst can

lead to desirable reactivity. Therefore, it is of interest to conduct further reactor studies to correlate results from the theoretical calculations and model surface experiments on inverse oxide surfaces with *in situ* characterization of corresponding powder catalysts. This will allow a full understand of the active sites and reaction mechanisms on the powder catalysts under industrially relevant reaction conditions. In addition, due to the recent advances of machine learning in catalysis, it is also possible to leverage machine learning methods to accelerate the discovery of promising catalysts for biomass upgrading. These aspects will be discussed in the following subsections.

7.2.1 In-Depth Mechanistic Studies Using Inverse Oxide Model Surfaces

Oxide-supported metal catalysts are widely used in the industry.[4] Nonetheless, the interaction between metals and oxides as well as the active sites for catalytic biomass transformation are less well understood. Inverse oxide catalysts are catalytic materials with oxides deposited on metal substrates, in contrast to the conventional metal-over-oxide architecture. The advantage of the inverse oxide design is that by depositing oxides over metals, the oxide-metal interface can be maximized, which will facilitate mechanistic studies of interfacial active sites that catalyze many reactions. The inverse oxide design can sometimes stabilize active sites that cannot be stabilized otherwise. In Chapter 6, the inverse oxide design is utilized to study the IPA dehydration reaction over WO_x/Pt(111). Model surface experiments demonstrate the different functionality of the WO_x and Pt sites, while DFT calculations are used to further investigate the synergistic effect of WO_x and Pt. Such an approach can be extended to other relevant inverse oxide systems. It is also important to conduct steady-state reactor evaluations using powder catalysts and *in situ* characterization with ambient-pressure X-ray photoelectron spectroscopy (AP-XPS) and X-ray adsorption spectroscopy (XAS) measurements to investigate the dynamics of active sites and important reaction intermediates under reaction conditions. The combined first-principles

calculations, model surface experimentation, and *in situ* characterization of powder catalysts can provide an in-depth understanding of active sites, reaction mechanism, and rate-determining steps to guide rational catalyst design for the catalytic upgrading of biomass.

7.2.2 Machine Learning Guided Catalyst Design for Biomass Upgrading

With recent rapid development machine learning in catalysis,[5] it is possible to combine machine learning with multiscale modeling (DFT, microkinetic modeling, kinetic Monte Carlo and molecular dynamics simulations, *etc.*) to accelerate the identification of promising catalyst candidates and the development of catalysts. For example, it can take months to calculate activation barriers of elementary reactions using the DFT methods with current computational power. With the assistance of machine learning, DFT-calculated energetics and bind configurations can be used for training machine-learnt models.[6] Upon the completion of training, such models can be used to predict catalyst activity and selectivity effectively. Using this method, it is possible to screen a wide range of catalyst candidates with different compositions to select the most promising candidates. Machine learning can also be used in combination with molecular dynamics (MD) simulations to enable the calculations of industrial-relevant catalyst nanoparticles, which are significantly larger in size compared to the slab models with periodical boundary conditions used in DFT calculations. In addition, machine-learning-guided MD simulations[7] can also predict catalytic properties at elevated temperatures and pressures instead of 0 K and pristine environment used in the case of DFT calculations. With the help of carefully selected machine learning methods, MD simulations can be performed in most realistic conditions to explain experimentally observed phenomena. Using machine learning-assisted computation techniques, it is possible to rapidly screen a large number of catalyst candidates and predict the most promising ones, which can be evaluated with model surface experiments as well as reactor studies. Such a

combined approach should help accelerate the identification and rational design of optimal catalysts for application-dependent biomass catalytic transformations.

7.3 References

(1) Kwon, Y.; Schouten, K. J. P.; Waal, J. C. Van Der; Jong, E. De; Koper, M. T. M. Electrocatalytic Conversion of Furanic Compounds. *ACS Catal.* **2016**, *6*, 6704–6717. https://doi.org/10.1021/acscatal.6b01861.

(2) Wan, W.; Tackett, B. M.; Chen, J. G. Reactions of Water and C1 Molecules on Carbide and Metal-Modified Carbide Surfaces. *Chem. Soc. Rev.* **2017**, *46* (7), 1807–1823. https://doi.org/10.1039/C6CS00862C.

(3) Tackett, B. M.; Sheng, W.; Chen, J. G. Opportunities and Challenges in Utilizing Metal-Modified Transition Metal Carbides as Low-Cost Electrocatalysts. *Joule* **2017**, *1* (2), 253–263. https://doi.org/10.1016/j.joule.2017.07.002.

(4) Rodríguez, J. A.; Hrbek, J. Inverse Oxide/Metal Catalysts: A Versatile Approach for Activity Tests and Mechanistic Studies. *Surface Science*. February 15, 2010, pp 241–244. https://doi.org/10.1016/j.susc.2009.11.038.

(5) Kitchin, J. R. Machine Learning in Catalysis. *Nat. Catal.* **2018**, *1*, 230–232. https://doi.org/10.1038/s41929-018-0056-y.

(6) Artrith, N.; Lin, Z.; Chen, J. G. Predicting the Activity and Selectivity of Bimetallic Metal Catalysts for Ethanol Reforming Using Machine Learning. *ACS Catal.* **2020**, *17*, 9438–9444. https://doi.org/10.1021/acscatal.0c02089.

(7) Artrith, N.; Hiller, B.; Behler, J. Neural Network Potentials for Metals and Oxides - First Applications to Copper Clusters at Zinc Oxide. *Phys. status solidi* **2013**, *250* (6), 1191–1203. https://doi.org/10.1002/pssb.201248370.

Appendix A: Reprint Permission Letters

A.1 Chapter 1

Hydrodeoxygenation of biomass-derived oxygenates over metal carbides: from model surfaces to powder catalysts

Z. Lin, R. Chen, Z. Qu and J. G. Chen, *Green Chem.*, 2018, **20**, 2679

DOI: 10.1039/C8GC00239H

If you are not the author of this article and you wish to reproduce material from it in a third party non-RSC publication you must formally request permission using Copyright Clearance Center. Go to our Instructions for using Copyright Clearance Center page for details.

Authors contributing to RSC publications (journal articles, books or book chapters) do not need to formally request permission to reproduce material contained in this article provided that the correct acknowledgement is given with the reproduced material.

Reproduced material should be attributed as follows:

- For reproduction of material from NJC:
  Reproduced from Ref. XX with permission from the Centre National de la Recherche Scientifique (CNRS) and The Royal Society of Chemistry.
- For reproduction of material from PCCP:
  Reproduced from Ref. XX with permission from the PCCP Owner Societies.
- For reproduction of material from PPS:
  Reproduced from Ref. XX with permission from the European Society for Photobiology, the European Photochemistry Association, and The Royal Society of Chemistry.
- For reproduction of material from all other RSC journals and books:
  Reproduced from Ref. XX with permission from The Royal Society of Chemistry.

If the material has been adapted instead of reproduced from the original RSC publication "Reproduced from" can be substituted with "Adapted from".

In all cases the Ref. XX is the XXth reference in the list of references.

If you are the author of this article you do not need to formally request permission to reproduce figures, diagrams etc. contained in this article in third party publications or in a

thesis or dissertation provided that the correct acknowledgement is given with the reproduced material.

Reproduced material should be attributed as follows:

- For reproduction of material from NJC:
  [Original citation] - Reproduced by permission of The Royal Society of Chemistry (RSC) on behalf of the Centre National de la Recherche Scientifique (CNRS) and the RSC
- For reproduction of material from PCCP:
  [Original citation] - Reproduced by permission of the PCCP Owner Societies
- For reproduction of material from PPS:
  [Original citation] - Reproduced by permission of The Royal Society of Chemistry (RSC) on behalf of the European Society for Photobiology, the European Photochemistry Association, and RSC
- For reproduction of material from all other RSC journals:
  [Original citation] - Reproduced by permission of The Royal Society of Chemistry

If you are the author of this article you still need to obtain permission to reproduce the whole article in a third party publication with the exception of reproduction of the whole article in a thesis or dissertation.

Link to webpage: Hydrodeoxygenation of biomass-derived oxygenates over metal carbides: from model surfaces to powder catalysts - Green Chemistry (RSC Publishing)

A.2 Chapter 2: Figure 2.1, 2.2, 2.3

ELSEVIER LICENSE
TERMS AND CONDITIONS
May 18, 2021

This Agreement between Zhexi Lin ("You") and Elsevier ("Elsevier") consists of your license details and the terms and conditions provided by Elsevier and Copyright Clearance Center.

License Number	5072090682238
License date	May 18, 2021
Licensed Content Publisher	Elsevier
Licensed Content Publication	Surface Science Reports
Licensed Content Title	Monolayer bimetallic surfaces: Experimental and theoretical studies of trends in electronic and chemical properties
Licensed Content Author	Jingguang G. Chen,Carl A. Menning,Michael B. Zellner
Licensed Content Date	May 15, 2008
Licensed Content Volume	63
Licensed Content Issue	5
Licensed Content Pages	54
Start Page	201
End Page	254
Type of Use	reuse in a thesis/dissertation
Portion	figures/tables/illustrations
Number of figures/tables/illustrations	3
Format	both print and electronic
Are you the author of this Elsevier article?	No
Will you be translating?	No
Title	Catalytic Transformation of Biomass-Derived Oxygenates Using Transition Metal Carbide, Nitride, and Oxide Surfaces
Institution name	Columbia University
Expected presentation date	Jun 2023
Portions	Fig. 1, Fig. 2, Fig. 3.
Requestor Location	Zhexi Lin 500 W. 120th St

	Mudd 801 NEW YORK, NY 10027 United States Attn: Zhexi Lin
Publisher Tax ID	98-0397604
Total	0.00 USD

A.3 Chapter 3

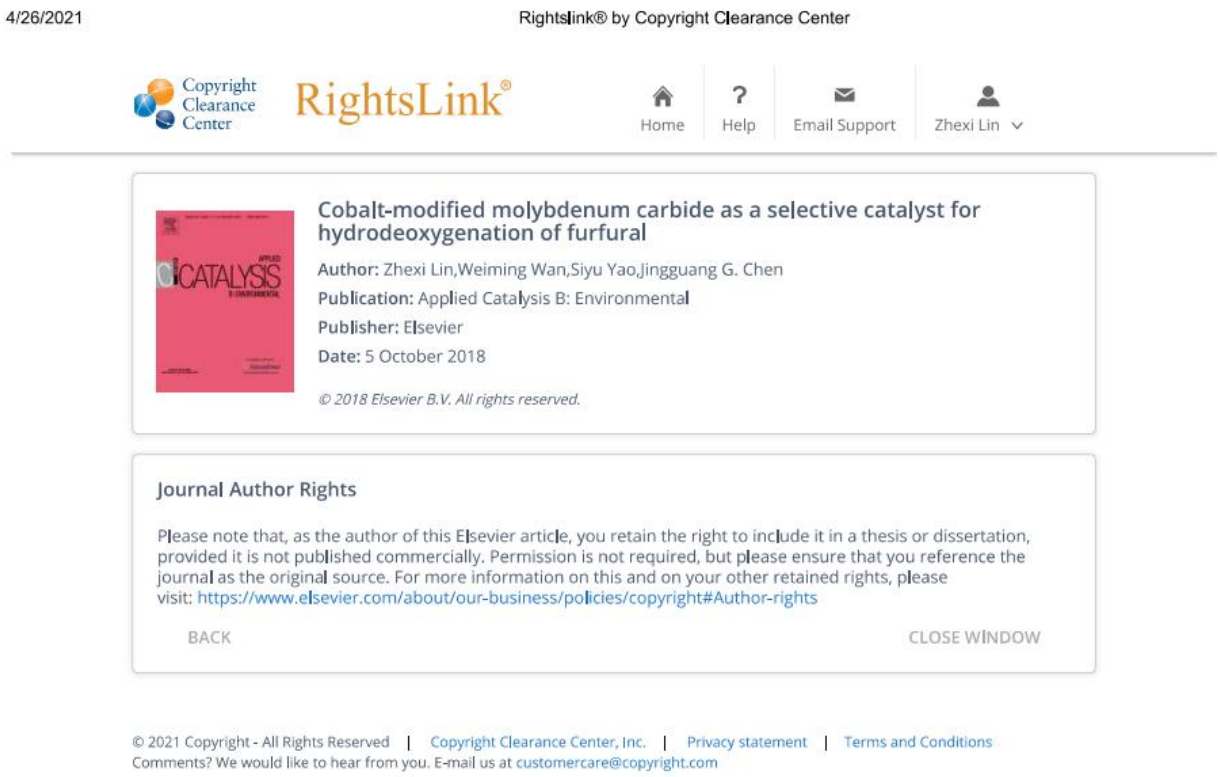
4/26/2021
Rightslink® by Copyright Clearance Center
Copyright Clearance Center
RightsLink®
Home
Help
Email Support
Zhexi Lin
Cobalt-modified molybdenum carbide as a selective catalyst for hydrodeoxygenation of furfural
Author: Zhexi Lin,Weiming Wan,Siyu Yao,Jingguang G. Chen
Publication: Applied Catalysis B: Environmental
Publisher: Elsevier
Date: 5 October 2018
© 2018 Elsevier B.V. All rights reserved.
Journal Author Rights
Please note that, as the author of this Elsevier article, you retain the right to include it in a thesis or dissertation, provided it is not published commercially. Permission is not required, but please ensure that you reference the journal as the original source. For more information on this and on your other retained rights, please visit: https://www.elsevier.com/about/our-business/policies/copyright#Author-rights
BACK
CLOSE WINDOW
© 2021 Copyright - All Rights Reserved | Copyright Clearance Center, Inc. | Privacy statement | Terms and Conditions
Comments? We would like to hear from you. E-mail us at customercare@copyright.com

A.4 Chapter 4

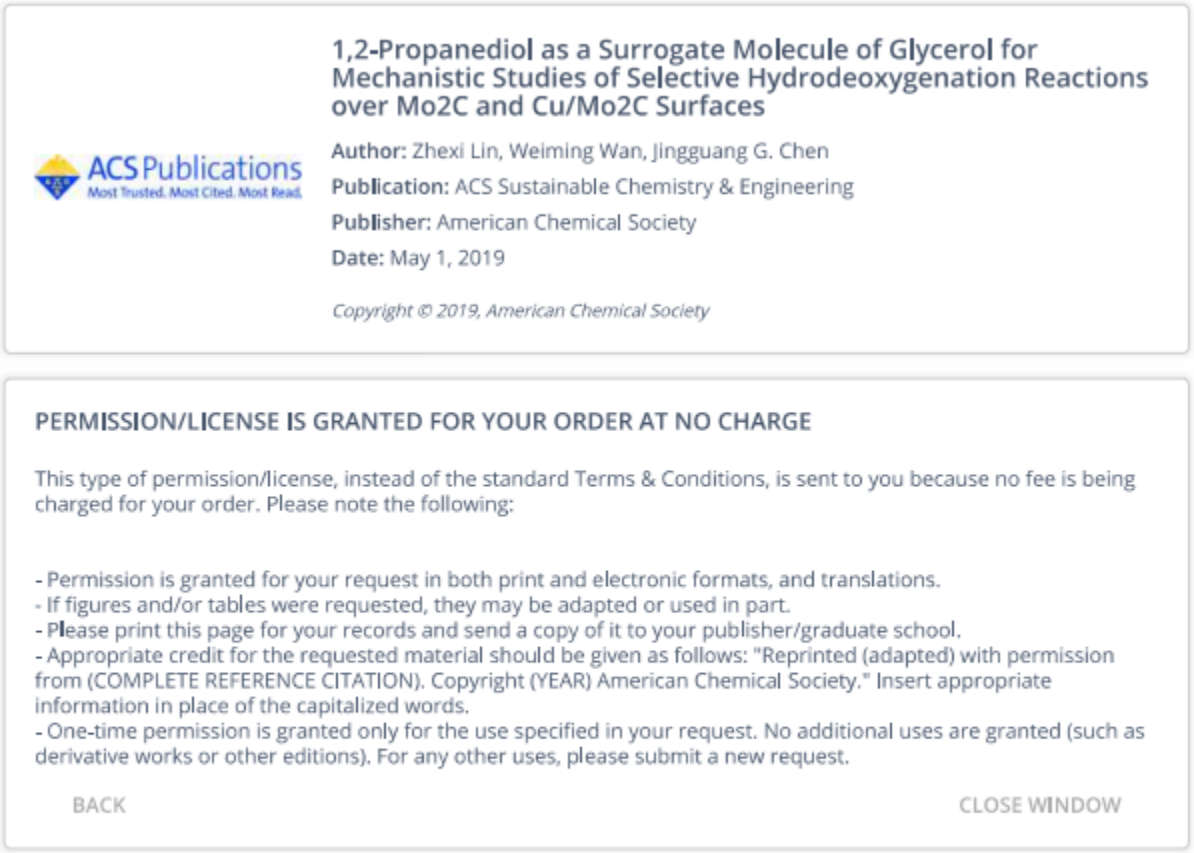

1,2-Propanediol as a Surrogate Molecule of Glycerol for Mechanistic Studies of Selective Hydrodeoxygenation Reactions over Mo2C and Cu/Mo2C Surfaces

Author: Zhexi Lin, Weiming Wan, Jingguang G. Chen

Publication: ACS Sustainable Chemistry & Engineering

Publisher: American Chemical Society

Date: May 1, 2019

Copyright © 2019, American Chemical Society

PERMISSION/LICENSE IS GRANTED FOR YOUR ORDER AT NO CHARGE

This type of permission/license, instead of the standard Terms & Conditions, is sent to you because no fee is being charged for your order. Please note the following:

- Permission is granted for your request in both print and electronic formats, and translations.
- If figures and/or tables were requested, they may be adapted or used in part.
- Please print this page for your records and send a copy of it to your publisher/graduate school.
- Appropriate credit for the requested material should be given as follows: "Reprinted (adapted) with permission from (COMPLETE REFERENCE CITATION). Copyright (YEAR) American Chemical Society." Insert appropriate information in place of the capitalized words.
- One-time permission is granted only for the use specified in your request. No additional uses are granted (such as derivative works or other editions). For any other uses, please submit a new request.

BACK CLOSE WINDOW